THE INFLUENCE OF ALLEY CROPPING SYSTEMS ON SOIL WATER DYNAMICS AND SOIL EROSION IN A CHANGING CLIMATE

Scientific report for Ouranos-ICAR Climate Change Action Plan 26 “Biodiversity”

By
Alain N. Rousseau
Dennis W. Hallema
Silvio J. Gumiere
Gabriel Hould-Gosselin
Claudie Ratté-Fortin

Centre Eau Terre et Environnement
Institut national de la recherche scientifique (INRS-ETE)
490, rue de la Couronne
Québec (QC) G1K 9A9

Rapport R-1441

May 30, 2013

ISBN : 978-2-89146-789-6

Table of Contents

List of Tables

List of Figures

List of Abbreviations and Acronyms

BMP	Beneficial management practice
CDF	Cumulative distribution function
CRCM	Canadian Regional Climate Model
DEM	Digital Elevation Model
ET_0	Reference evapotranspiration
FDR	Frequency domain reflectometry
GCM	Global climate model
INRS-ETE	Institut National de la Recherche Scientifique – Centre Eau, Terre, Environnement
LIDAR	Light detection and ranging
MHYDAS	Modélisation Hydrologique Distribuée des Agrosystèmes
PET	Potential evapotranspiration
PSD	Particle size distribution
RCM	Regional climate model
RS	Reach segment
SCS	Soil Conservation Service
SU	Surface unit

1 Introduction

1.1 Framework

This study was conducted within the framework of the Climate Change Action Plan 26 “Biodiversity” funded by Ouranos and ICAR, under the supervision of A. Olivier (Université Laval) and in collaboration with partners at the UQAM Centre for Forest Research (A. Paquette and S. Domenicano), and Institut de Recherche en Biologie Végétale (UdeM; A. Cogliastro, D. Rivest and L. Bouttier).

Contributors at INRS were A. N. Rousseau (local project lead, research and field study), D. W. Hallema (hydrological research, field study, final report), S. J. Gumiere (research and field study, now at Université Laval), G. Hould Gosselin (research on erosion), C. Ratté-Fortin (rating curves), and in the field: G. Levrel (soil moisture probes), M. Fossey (grain size analysis), G. Carrer (meteorological station) and E. Maroy (all INRS-ETE). S. Tremblay (INRS-ETE) and Y. Périard (Université Laval) provided technical assistance.

1.2 The effects of alley cropping as an agroforestry practice

Alley cropping is an agroforestry practice whereby hardwood trees are planted at wide spacings, creating alleyways within which agricultural, horticultural or companion crops are grown (Gold and Garrett, 2009). In the temperate climate zone, alley cropping systems represent an alternative to traditional row cropping and help deal with specific issues such as wind erosion and crop failure due to excessive surface evaporation. The practice is also used in areas to help the transition of row crops into forest and for its excellent stewardship qualities (Garrett *et al.*, 2011).

Hydrologists have long known that soil water dynamics and erosion by surface runoff depend in varying degrees on local weather (precipitation, solar irradiance, temperature and wind), vegetation (distribution of the root system, growth stage), soil characteristics (texture, soil type, porosity) and upstream drainage area. The implementation of alley cropping systems has an immediate effect on the first two in this list (local meteorological variables and vegetation), and studying these effects inescapably involves the study of the interaction between both.

1.3 Outline

The report continues with the scientific context and objectives. In the third chapter we will expand the theoretical framework within which we collected the required data and developed the corresponding methods (chapter 4). Chapter 5 and 6 present the outcomes of the study with most notably, the modeling results, followed by the conclusion in chapter 7.

2 Scientific context and objectives

2.1 Background

The components of a canopy of vegetation are known to influence the airflow near the land surface (Wilson and Shaw, 1977), and it is for this reason that alley cropping has a direct effect on transpiration and, as a consequence, on the soil water balance. Local meteorological variables are the result of an interaction between the thermal energy balance at the soil surface (net radiation, latent and sensible heat flux) and the atmospheric water balance (atmospheric density, vapor pressure deficit; Monteith, 1981).

Depending on characteristics of the environment in which alley cropping is practiced, such as elevation, relief and height of vegetation, we may expect that alley cropping systems influence local meteorological variables as well as the water distribution in the soil and at the soil surface. The distribution of soil water is a key factor in the growth and survival of trees and crops alike. If trees are able to redistribute water from layers with a low water availability (below the wilting point) to the upper layers of the soil where the trees and crops absorb water, both are more likely to survive and maintain high growth rates even during dry spells (*e.g.* Plamboeck *et al.*, 1999).

Alley cropping also has an effect on erosion, depending on the type of crop. The cultivation of annual crops decreases the amount of soil organic matter, and can lead to enhanced erosion, especially on hillslopes with a high gradient (Kremer and Kussman, 2010). Perennial crops on the other hand maintain a continuous cover throughout the year, resulting in a reduced detachment of soil particles during rainfall and a maximization of infiltration. On the field scale, the tree rows may behave in a similar way as the vegetated filters along water streams, trapping sediment and preventing the evacuation of suspended load (Gumiere and Rousseau, 2011).

Given the reported effects of alley cropping in the microclimate zone, it is highly probable that alley cropping systems in southern Quebec provide a certain level of resilience to drought and increased rainfall intensity expected for this region (*e.g.* Mailhot *et al.*, 2007), while simultaneously reducing the risk of water erosion and crop damage.

2.2 Objectives and hypotheses

In the light of changing environmental conditions caused by a shift in the local climate, the present study aims to characterize and evaluate local hydrology and erosion in an alley cropping system in southern Quebec for the present climate and climate conditions simulated for the period 2041-2070. Our hypotheses are the following:

1. The root systems of trees in an alley cropping systems improve the resilience of intercrops to drought and increased rainfall;

2. Alley cropping systems reduce the risk of water erosion at the field scale.

2.3 Approach

In order to quantify the effect of alley cropping systems on soil water dynamics and water erosion, we adopted a two-fold approach in which we study first the soil water dynamics, and second, the processes of water erosion, transportation and deposition, both for different climate change scenarios. The approach was divided into five steps, corresponding to five chapters of this report:

1. Field work: Collection of weather data, soil samples and soil moisture data during two field campaigns in 2011 and 2012 at an experimental alley cropping site near St. Paulin (province of Quebec, Canada) with two different tree species. Soil moisture patterns were measured with 45 frequency domain reflectometers (FDR sensors) installed up to a depth of one meter along a 25-m transect perpendicular to two tree rows and the alley between them.

2. Analysis of spatial patterns of water movement within the soil. The latter was done by performing a spatial interpolation of the point data obtained by the FDR sensors.

3. Analysis of weather data and simulation of climate change between the periods 1967-1996 and 2041-2070 at the experimental site. This step involves the simulation of daily values for precipitation, daily maximum temperature and daily minimum temperature.

Figure 1. Springtime photograph of the experimental alley cropping site near St. Paulin, Quebec (31/05/2012). Tree rows are planted at a 12.4 m distance with an open space in between, the alley, where crops or forage are grown. The tree rows are not continuous in the row direction.

The first three steps in the approach helped obtaining a first image of the hydrological processes that govern the alley cropping system, and the large number of FDR sensors installed on a small transect makes the field study unique in its own right. After data analysis we continued with:

4. Two-dimensional simulation of water movement within the soil below the alley cropping system. HYDRUS 2D/3D (Simunek *et al.*, 1992) was used to describe the spatial domain of the transect with finite elements and simulate the following processes:

    a. Variably saturated flow in the soil with the Richards equation (Richards, 1931);
    b. Transpiration after root uptake with Feddes linear water stress response function (Feddes *et al.*, 1978; Feddes *et al.*, 2001);
    c. Potential transpiration using the Penman-Monteith equation (Penman, 1948; Monteith, 1981; Allen *et al.*, 1998).

    Three different scenarios were evaluated:

    a. Scenario a: Observed field situation during the summer and autumn of 2011;
    b. Scenario b: Observed field situation during the summer and autumn of 2012;
    c. Scenario d: Climate change scenario for 2041-2070.

    Scenarios a and b provide the parameterization of the model and are used to determine the water availability under current climate conditions, whereas scenario d gives an indication how alley cropping systems influence water availability to vegetation in the long term.

5. Simulation of the influence of the following processes on water erosion at the field scale with MHYDAS-Erosion (Gumiere *et al.*, 2010): sheet erosion, rill erosion and sediment trapping by rows of trees in alley cropping systems. The modeling approach was divided in two steps:

    a. Calibration of MHYDAS-Erosion on the 2.5-km^2 Bras d'Henri microwatershed with intensive farming in the Beauce region of Quebec (study site of the Canadian project WEBs – Watershed Evaluation of Beneficial Management Practices); and

    b. Simulation of the impact of alley cropping on sediment trapping at the same watershed using the parameter values found after calibration for synthetic rainfall events with return periods of 10, 50 and 100 year. Six- and 24-hour Chicago and triangular rainfall distributions were used to simulate the response to different rainfall peaks and average intensities, as these are the most common rainfall distributions in this region (Mailhot *et al.*, 2007). Two scenarios were evaluated for sediment trapping:

        i. Bras d'Henri microwatershed without alley cropping (current field situation); and
        ii. Bras d'Henri microwatershed with alley cropping (hypothetical scenario). This scenario assumes that tree rows are planted along the downstream edge of all fields.

3 Theoretical framework and literature review

3.1 Simulation of soil moisture patterns with HYDRUS 2D/3D

HYDRUS 2D/3D was selected as the software environment in which we developed a model for soil water movement below the alley cropping system. HYDRUS traces its roots to the SWMS_2D model (Šimůnek *et al.*, 1992; based on Van Genuchten, 1987), which later evolved into a software package for simulating two- and three-dimensional movement of water, heat and solutes in variably saturated media (Šimůnek *et al.*, 2011; Šejna *et al.*, 2011). The choice for HYDRUS 2D/3D was motivated by the versatility of the software with respect to the spatial representation of the simulated domain and process interaction it can account for, and also by its widespread use for educational and professional applications.

The concepts and physically-based equations that represent hydrological processes within the model allow for simulating:

- Precipitation, infiltration, groundwater flow, throughflow and seepage using Richards equation (Richards, 1931);

- Transpiration after root uptake by vegetation using Feddes linear water stress response function (Feddes *et al.*, 1978; Feddes *et al.*, 2001);

- Evaporation from the soil surface and actual transpiration (together called evapotranspiration) using the Penman-Monteith equation (Penman, 1948; Monteith, 1981; Allen *et al.*, 1998).

These governing equations have also been used in other physically-based models developed over the last decades. HYDRUS 2D/3D can simulate flow for different time scales (event-based or continuous-time) and spatial scales (soil column, plot scale and field scale). In this project we are mainly interested in soil water distribution at the plot scale, because this is the scale at which we can observe changes in local variables that play a role on the scale at which intervention takes place, namely the field scale.

The hydrologic response of an alley cropping system is characterized by the following hydrological processes. First rainfall infiltrates into the soil surface and from there moves vertically and laterally through the soil (infiltration, throughflow). This phenomenon is simulated using the Richards equation for variably saturated flow. Subsequently, water can be either stored in pore spaces, leave the upper soil by percolation to the groundwater table, be taken up by roots (potential transpiration), or evaporate directly from the soil surface.

We have selected three models that are able to simulate these processes observed in the soil (up to 1.5 m depth), which are (i) the nonlinear Richards equation for variably saturated flow in the soil, (ii) Feddes linear water stress response function for simulating water uptake by roots, and (iii) the Penman-Monteith evaporation model for surface evaporation.

3.1.1 Model for variably saturated flow

We used the Richards equation (Richards, 1931) to simulate infiltration and variably saturated flow in the soil. This is a non-linear partial differential equation that combines the Darcy-Buckingham equation and the continuity equation (formulated here for one dimension):

$$\frac{\partial \theta(h)}{\partial t} = \frac{\partial}{\partial z}\left(K(h)\frac{\partial h}{\partial z}\right) + \frac{\partial K(h)}{\partial z} - S(h)$$

where θ is the volumetric water content [L^3 L^{-3}], t is time [T], z is a spatial coordinate [L], $K(h)$ is the hydraulic conductivity, which is a function of pressure head h [LT^{-1}], and $S(h)$ is a sink function representing water uptake by roots. The formulation above is the mixed form of the Richards equation, referring to the presence of two dependent variables θ and h, where the rate of change in water content is expressed by the sum of the capillary flow and gravity flow terms minus the sink term.

When $\frac{d\theta}{dt}$ is represented by a soil water capacity function $C_w(h)$ that characterizes the slope of the retention curve, the Richards equation can also be expressed in terms of pressure head only. This way, we obtain the pressure head formulation:

$$C_w(h)\frac{\partial h}{\partial t} = \frac{\partial}{\partial z}\left(K(h)\frac{\partial}{\partial z}\right) + \frac{\partial K(h)}{\partial z} - S(h)$$

HYDRUS uses the numerical finite element method to solve the Richards equation in space and the finite difference method to solve the Richards equation in time. Soil water capacity function $C_w(h)$ is defined by a hydraulic model, in this case the Brooks and Corey (1964) soil water retention function:

$$S_e = \begin{cases} |\alpha h|^{-n}, & h < -1/\alpha \\ 1, & h \geq -1/\alpha \end{cases}$$

and hydraulic conductivity function given by:

$$K = K_s S_e^{2/n+l+2}$$

where K_s is the saturated hydraulic conductivity, α is the inverse of an empirical air-entry value, n is pore size distribution index assumed for a given particle size distribution, l is a pore connectivity parameter (value assumed equal to 2.0 by Brooks and Corey, 1964), and S_e is the effective water content defined as:

$$S_e = \frac{\theta - \theta_r}{\theta_s - \theta_r}$$

with θ_r and θ_s representing the residual water content and the water content at saturation, respectively.

3.1.2 Root uptake model

Root uptake was simulated with the model developed by Feddes *et al.* (2001), which defines the maximum possible (*i.e.* potential) water extraction rate by plants $S_p(z)$ [T^{-1}] under optimal water availability integrated over rooting depth D_{root} as equal to the potential transpiration rate T_p [LT^{-1}]. S_p for depth z is given by the fraction of the root length density at depth z over the total root length density:

$$Sp(z) = \frac{\pi_{root}(z)}{\int_{-D_{root}}^{0} \pi_{root}(z)\partial z} T_p$$

$$potential\ root\ uptake\ rate = \frac{root\ length\ density}{total\ root\ length\ density} \times potential\ transpiration\ rate$$

where the potential transpiration rate was simulated with the Penman-Monteith equation (see following sections). The influence of water stress on water extraction is expressed by a dimensionless stress response function of the pressure head yielding:

$$S(z) = \alpha(h) S_p$$

where $S(z)$ is the actual flux density at depth z and α the dimensionless water stress response function for which $0 \leq \alpha \leq 1$.

The water stress response function can be defined in multiple ways, for example with a linear function (Feddes *et al.*,1978), with a nonlinear water and osmotic stress response function (Van Genuchten, 1987), and even in combination with a time-variable root depth function (Verhulst-Pearl, 1838; Pearl and Reed, 1920). For the sake of parsimony we use the linear water stress response function (Feddes *et al.*, 1978) in combination with a constant root distribution that does not evolve over time (Vrugt *et al.*, 2001).

Water stress response is approximated by a continuous linear function α defined by four pressure head values, numbered h_1 to h_4 (see figure below). Water uptake is assumed zero for pressure heads higher than the air-entry pressure h_1 ($pF \approx 2$ for sand, $pF \approx 2.4$ for silt and $pF \approx 2.5$ for clay), also called the anaeobiosis point, and for pressure heads lower than the permanent wilting point h_4 ($pF \approx 4.2$ for sand, silt and clay).

Between field capacity h_2 and wilting point h_3 the water uptake rate equals S_p when the water stress is minimal, in which case $\alpha(h) = 1$. When the pressure head in the pore spaces is higher than wilting point h_3, S_p equals the potential transpiration rate T_p. In the event that the pressure head falls below the wilting point, the potential water uptake is reduced to the actual uptake.

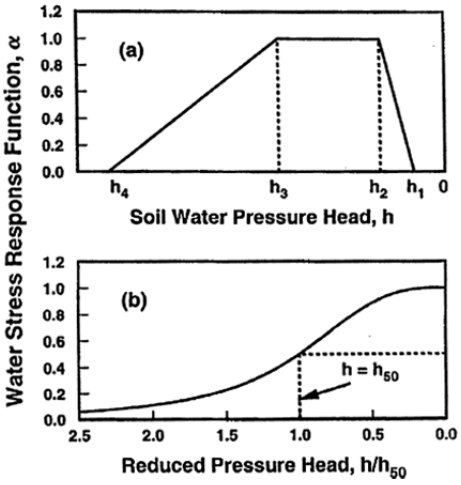

Figure 2. The water stress response function $\alpha(h)$ defined by (a) Feddes *et al.* (1978) and (b) Van Genuchten (1987), taken from Šimůnek *et al*. (2009).

3.1.3 Water uptake distribution model

Rather than simulating the uptake of individual roots, the potential water uptake is simulated by a potential water uptake distribution function. Following this approach, it is possible to represent a variety of different root systems of different vegetation with one potential water uptake distribution function. The time-invariant distribution of the root systems is described by a shape factor that defines the two-dimensional distribution of potential water uptake (Vrugt *et al.*, 2001a,b):

$$b(x,z) = (1 - \frac{z}{Z_m})(1 - \frac{x}{X_m})e^{-(\frac{p_z}{Z_m}|z^* - z| + \frac{p_r}{X_m}|x^* - x|)}$$

where $b(x,z)$ is the potential water uptake distribution function, where X_m and Z_m are the maximum rooting length and maximum rooting depth, respectively, x and z are the distances from the origin of the plant at the surface in horizontal and vertical direction, respectively, p_x, x^*, p_z and z^* are empirical parameters used to ensure zero water uptake at $z=Z_m$. x^* and z^* are called the radius and depth of maximum intensity, respectively. The potential water uptake can now be calculated for a root zone with arbitrary shape (Vogel, 1987):

$$S_p = b(x,z) S_t T_p$$

where T_p [L T^{-1}]is the potential transpiration rate and S_t is the diameter of the zone through which the plant transpires.

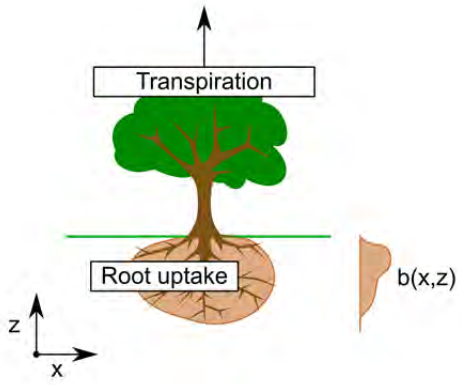

Figure 3. Two-dimensional distribution of potential water uptake by roots represented with a distribution function b(x,z) (Vrugt *et al.*, 2001a,b).

3.1.4 Potential evapotranspiration models

Assuming that the potential evapotranspiration rate was dominated by the upward flux from vegetation canopy, we used the Penman-Monteith equation to calculate a reference evapotranspiration rate ET_0 [LT^{-1}] for 2011 and 2012 with data recorded by the local weather station (Penman ,1948; Monteith, 1981; Allen *et al.*, 1998):

$$ET_0 = \frac{0.408\Delta(R_n - G) + \gamma \frac{900}{T+273} u_2 (e_s - e_a)}{\Delta + \gamma(1 + 0.34u_2)}$$

where R_n is the net incoming radiation at the crop surface [$MJ.m^{-2}day^{-1}$], calculated as twice the radiation measured with the PAR sensor, G is the heat transfer into the soil [$MJ.m^{-2}day^{-1}$], ρ is the atmospheric density [$kg.m^{-3}$], c_p is the specific heat of moist air [1.013 $kJ.kg^{-1}.°C^{-1}$], T is the mean daily air temperature at 2 m height [°C], u_2 is the wind speed at 2 m height, e_s is the vapor pressure at temperature T [kPa], e_a is the actual vapor pressure [kPa], Δ is the slope of the vapor pressure curve [$kPa.C^{-1}$] and γ is the psychrometric constant [$kPa.°C^{-1}$]. Heat transfer into the soil (G) is relatively small compared to the other terms for the summer and autumn periods in a humid continental climate, and was therefore neglected.

The weather data available for the periods 1967-1996 and 2041-2070 did not include all variables necessary to calculate the Penman-Monteith equation, so for this period we used the empirical Hargeaves equation defined as (Hargeaves, 1974):

$$PET = MF \times T \times CH$$

where *PET* is potential evapotranspiration, *MF* is a tabulated monthly factor depending on latitude, *T* is the daily mean temperature (degrees Fahrenheit) and *CH* is a correction factor for when the 24-hour mean relative humidity exceeds 64 per cent.

3.2 Simulation of water erosion with MHYDAS-Erosion

3.2.1 Model overview

Intensive agriculture is often the cause of accelerated erosion with ablation rates many times higher than the rate of soil forming processes (pedogenesis). Water erosion is observed in most parts of the world, and some regions are more prone to erosion than others depending on vegetation type and density, as well as rainfall intensity and frequency.

In agricultural watersheds, Beneficial Management Practices (BMPs) are known to improve soil conservation and reduce sediment transport toward streams in the Quebec province (Quilbé *et al.*, 2007; Rousseau *et al.*, 2013). Structural BMPs such as alley cropping and other agroforestry practices in particular have the potential to modify flow paths and sediment connectivity in agricultural watersheds, thereby improving the overall sediment abatement at the watershed scale (Gumiere *et al.*, 2010, 2012).

The evaluation of the potential impact of alley cropping would ideally require two fields that are exactly alike, except for the presence of rows of trees on one of them, or else the possibility to cut the trees from an existing alley cropping site and study the difference before and after. The complexity of the study would also require the distributed measurement of erosion, transport and deposition processes, which is a great challenge by itself. These means were not available for this project and thus, a physically-based modeling approach was used for estimating the potential impact of alley cropping on water erosion at the field scale. In addition, a modeling study of erosion on alley cropping applied in the context of this study can eventually be upscaled in order to assess the influence of structural BMPs on erosion at the watershed scale.

For this part of the study, we used MHYDAS-Erosion (Gumiere *et al.*, 2010), an event and physically-based distributed model for linear erosion in agricultural watersheds, to simulate the following processes:

- Sheet erosion, which includes detachment by rain splash (Yann *et al.*, 2008) and transportation by shallow overland flow (Zhang and Horn, 2001), corrected for the transport efficiency reduced by discontinuity of flow (Gumiere *et al.*, 2010);

- Rill erosion, transport and deposition by unconfined concentrated flow (Foster *et al.*, 1995);

- Deposition of suspended material (or sediment trapping) at the base of the tree row due to an increased drag force exerted by the trees on flow (Deletic, 2005).

Because MHYDAS-Erosion was developed according to the principle of parsimony, the number of parameters is limited. The main input variables are rainfall intensity, soil map, land use map and land register. If desired, the user can specify a time-variable (dynamic) land use which is characteristic of the agricultural landscape.

3.2.2 Spatial discretization and topology

MHYDAS-Erosion uses a spatial subdivision of the watershed into surface units (SU) and a segmentation of the drainage network into channel sections, or reach segments (RS) (Lagacherie *et al.*, 2010). The surface units were created by intersection of spatial data including the digital elevation model, drainage network and the location of the spatial boundaries associated with fields, roads, units of the soil map and BMPs. Each surface unit is connected to the downstream end either to one surface unit (if there is one) or to one channel section (RS). The boundaries of spatial units are stored as vector shapes and may take virtually any geometrical form. Therefore, the model framework allows for adding spatial discontinuities such as BMPs (Gumiere *et al.*, 2010).

We used PHYSITEL (Rousseau *et al.*, 2011) and a 1-m digital elevation model or DEM (LIDAR) to create a subdivision into hillslopes by identifying the drainage network and calculating the accumulation matrix. Field maps are also used as spatial information to define the SUs. Hydrological short circuits are identified in the field, and are incorporated in the model to better define the topological links SU-SU and SU-RS. Figure 4 shows how spatial information layers are superposed to define the SUs. The drainage network is then separated into as many RS units as there are SU-RS connexions. In this study, the soil map is not used specifically for the spatial definition of SUs as the number of homogeneous regions would be too large. The soil map is instead used to assign the dominant soil type to the corresponding SU.

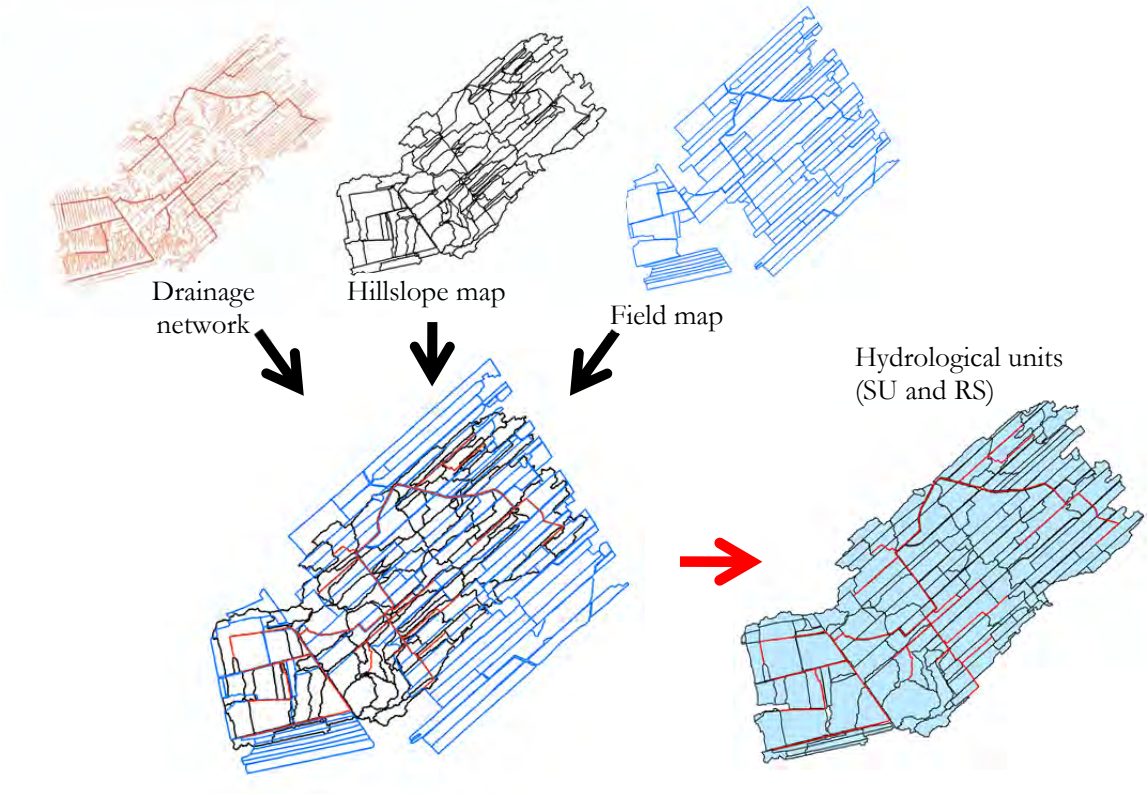

Figure 4: Spatial discretization into surface units (SU) and reach segments (RS) performed with PHYSITEL.

Topological links SU-SU and SU-RS are derived from specific hydrological path calculated using PHYSITEL. Adjustments are then made to include short circuits that cannot be identified by PHYSITEL alone with *in situ* observations. For example, a small culvert under a farm road allows one field to drain to another. Because the farm road is higher than the fields it divides, this connection is not identifiable with the pathways derived by the flow matrix alone. Figure 5 shows the downstream portion of the micro-catchment where branches 14 and 15 converge. SUs and RSs are identified by black and red numbers, respectively. The blue arrows indicate the topological pathways for each SU-SU and SU-RS connexion. For example, excess precipitation on SU 53 (located in the centre of the figure 5) flows to SU 36 under a farm road through a small culvert (diameter of approximately 10 cm). The combined flow of surface runoff and the contribution from the downstream SU 36 then flows to the drainage network, or the RS 8. This method allows the user to have greater control over the topological links in the model, allowing a more realistic scenario supported by field observations.

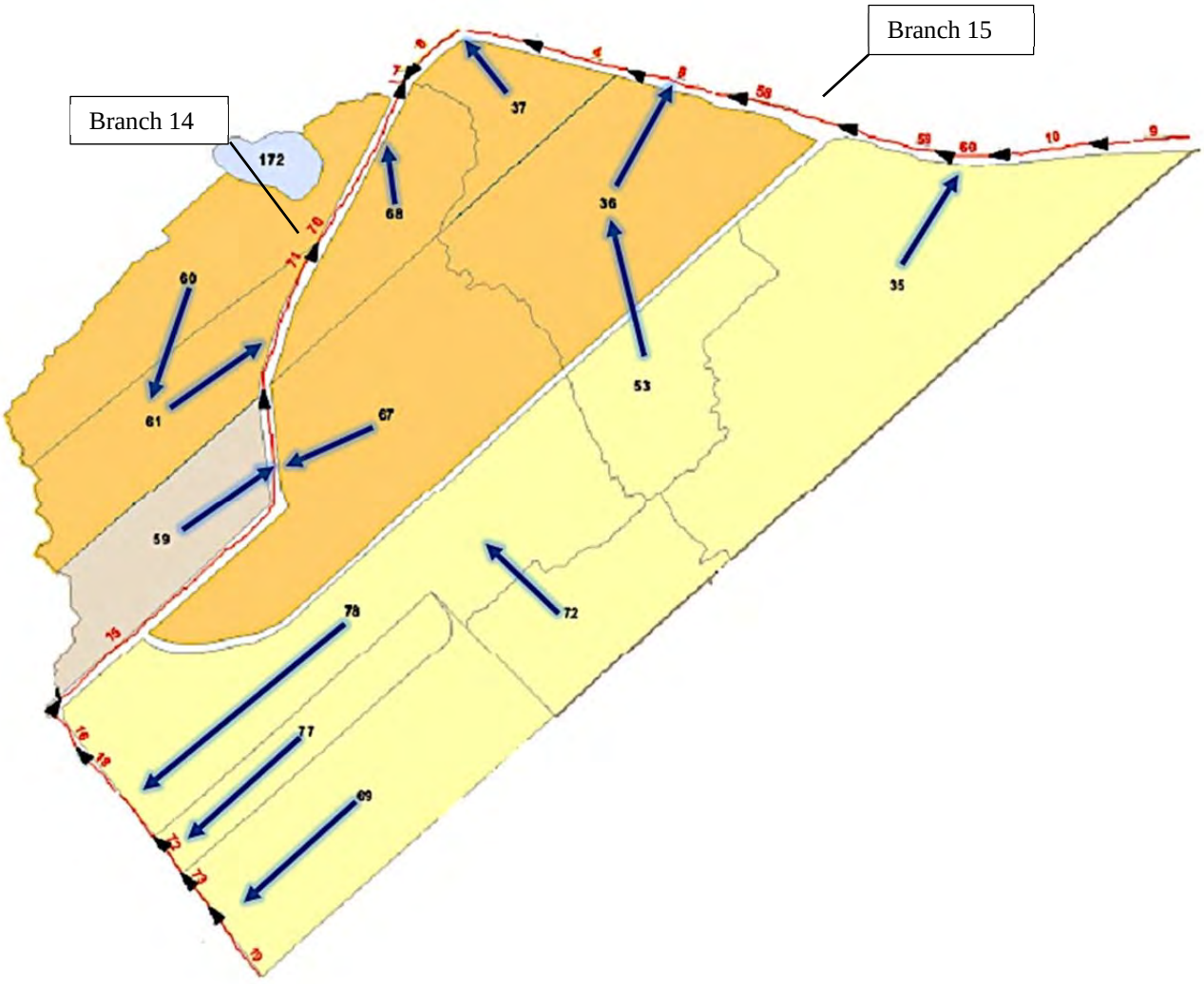

Figure 5: Topological links SU-SU & SU-RS near the micro-watershed outlet

3.2.3 Parameterization

3.2.3.1 Erosion parameters

As MHYDAS-Erosion takes into account spatially distributed information to create homogenous units, each model input parameter can also be spatially distributed. Geometric SU and RS parameters such as average slope, as well as soil stability parameters can be drawn from the same spatially distributed information used to generate SUs and RSs (crops, tillage practices, etc.). The model also requires as inputs initial moisture contents (θ_i); as initial conditions based on the normalized antecedent precipitation index (NAPI) for periods of 48 hours and 5 days. (Heggen, R. 2001). Table 1 shows the input parameters MHYDAS-erosion requires. Each parameter has a distinct value for each RS and SU.

Table 1 : MHYDAS-Erosion parameters

Parameter	Description	Unit
SU		
ks	Saturated hydraulic conductivity	m s^{-1}
hc	Air entry potential	m
$_r$	Soil residual moisture	m^3 m^{-3}
$_s$	Soil saturation moisture	m^3 m^{-3}
n_{SU}	Manning's roughness coef.	s m$^{-1/3}$
A_s	Aggregate stability index	—
N_{rill}	Number of rills	—
W	Rill width	m
$d50_{sed}$	Median sediment diameter	m
$_c$	Critical soil shear stress	*Pa*
Transfcode	Interface type indicator	—
K_r	Rill erodibility	s m^{-1}
Cetimax	Max transport coef from interrill erosion	—
Strip.width	Vegetated filter width	m
Strip.density	Density of vegetation on the filter	—
RS		
ks	Saturated hydraulic conductivity	m s^{-1}
n_{RS}	Manning's roughness coef.	s m$^{-1/3}$
K_r	Rill erodibility	s m^{-1}
$_c$	Critical soil shear stress	*Pa*

It should be noted that all hydrological and soil input parameters can vary during the year depending on land use (growth stage of crops, ploughing, etc.). The following sections explore in greater detail the range of values taken by each parameter according to land cover. A detailed look at the equations governing the transport and erosion mechanisms is beyond the scope of this report, and is presented in more detail by Gumiere *et al.* (2010).

3.2.3.2 Hydrological parameters

Hydrological input parameters include hydraulic conductivity (k_s), air entry potential (h_c), residual and saturated moisture content (θ_s and θ_r) and Manning's roughness coefficient for SUs and RS (n_{SU} and n_{RS}). These parameters are mainly responsible in separating precipitation into surface and sub-surface flow, as well as surface flow velocities and heights.

The values chosen for the Manning's coefficient are based on field observations throughout the summer and fall of 2012 and are based on the recommended values by Chow *et al.* (1964). Table 2 shows the different values assigned to the SU and RS as was growth or activity in the field.

Table 2: Manning's roughness coefficient according to land use (from Chow *et al.*, 1964)

Occupation	Manning start/end of season	Manning mature	Manning cut	Manning plowed
Unknown	0.03	0.035	0.03	0.030
Maize	0.032	0.040	0.032	0.027
Oats	0.032	0.450	0.032	0.030
Soy	0.030	0.040	0.035	0.027
Prairie	0.040	0.050	0.040	-
Prairie (late growth)	0.030	0.045	0.040	-
Forest	0.100	0.150	-	-
Urban	0.025	0.027	-	-

Residual moisture and saturation moisture (θ_s and θ_r) are based on soil texture described in the soil map provided by Agriculture and Agri-Food Canda (AAC) and corresponding values provided by the United States Department of Agriculture (USDA). Hydraulic conductivity values however, are not only strongly influenced by soil type, but also by farming practices such as ploughing. Coherent values for SUs and RSs are found by intersecting the soil and hydrological unit maps and assigning the dominant soil type for each unit. Those values are then altered if ploughing took place. Saturated hydraulic conductivity values (k_s) for the untilled soils were surveyed by AAC and their values are reported in Table 3. For the same ploughed soils, SU hydraulic conductivity values are multiplied by a factor of 10, as *in situ* measurements were not available.

Table 3: Saturated hydraulic conductivity according to soil type (see Table 9 for the nomenclature of soil names)

Soil	*ks* (mm/h)	Soil	*ks* (mm/h)
ALL	0.1	LBS	0.3
BVG1	19.6	MWO	21.1
BVG2	10.0	NUB	2.0
DGX	8.8	RRR	1.0
DQT	47.0	SJU	3.3
DSP	0.1	SPH	19.6
DSU	0.1	VAR	3.0

Finally, air entry potential values (h_c) are linked to residual and saturation moisture as well as topsoil porosity. Air entry potential values varying from 0.20 to 0.32 m are allocated by weighing a fixed maximum value (0.35 m) with topsoil porosity values surveyed by AAFC in 2007. .

3.2.3.3 Erosion and transport parameters

Parameters specific to the erosion and sediment transport alter soil cohesion, transport and deposition properties. MHYDAS-erosion simulates these processes in two parts: process caused by the impact of raindrops between the rills, and process caused by concentrated surface flow within the rills. Rills are defined as preferential paths, naturally formed by the topography, or artificially by ploughing.

Processes affecting the detachment and transport by rainfall only take place on SUs and are mainly contained in the areas between the rills. The interrill detachment equation used to simulate these processes was developed empirically by Yan *et al.* (2008) initially for the ultisoils type in China. Parameters influencing these processes can be summarized as: soil aggregate stability index between the rills (A_s) and transport efficiency coefficient between rills (CETI). The concept of CETI was introduced to describe the effect of the perpendicular roughness on the interrill-to-rill erosion contribution. $CETI_{max}$ is the maximum value that CETI can take.

Sediment detachment and transport processes in surface flow take place within SU rills and within the drainage network (RS). Parameters used in these processes can be summarised as: rill erodibility (K_r) and critical soil shear stress (τ_c). These two coefficients are used in the equation given by and Foster (1995).

Value ranges suggested by Gumiere *et al*. (2010) for each parameter are attributed to each SUs or RS according to land use and soil type. Erosion parameter value ranges are set according to land use or soil type (see table below).

Table 4: Erosion parameter value ranges according to land use or soil type

Parameter	Value	Land Use or Soil Type
A_s	0.001	Farm Roads
	0.7	Annual Crops
	0.5	Prairies & Forests
$CETI_{max}$	0.25	Farm Roads
	0.06	Annual Crops (Tilled)
	0.12	Annual Crops (Tilled)
	0.01	Prairies & Forests
τ_c	100	Farm Roads
	2	Sand, Soamy sands, Sandy loams
	3	Loams, Silty loams
	10	Clay, Loamy clay
K_r	1.00E-09	Farm Roads
	0.1	Sand, Loamy sands, Sandy loams
	0.01	Loams, Silty loams
	0.005	Clay, Loamy clay

The number of rills per SU (N_{rill}) is limited to 30 to ensure model stability. As all SUs cover an area large enough for more than 30 rills to occur, the maximum number of rills is attributed to all surface units in the watershed. Rill width is derived according to *in situ* observation and the crop type. For example, naturally occurring rills are distributed irregularly and have a width ranging between 10 and 50 cm. Artificial rills in corn fields are regularly spaced and have a width ranging from 60 to 75 cm. Finally, according to the sensitivity analysis performed by Gumiere *et al.* (2010), the median diameter of particles does not have a significant impact on simulation results, and is set to 0.3 mm.

4 Materials and methods

4.1 Materials

4.1.1 Description of the experimental alley cropping site

We selected an alley cropping site in the Rivière du Loup-Lac Saint-Pierre watershed near St. Paulin, Quebec, 20 km from the St. Lawrence River on the north shore at 46°27'9" N 72°59'29" W (see figure below). The site with an elevation between 130-144 m is located on Juneau Island, locked between two branches of the Rivière du Loup that split 1 km downstream of Hunterstown and merge again 600 m before the “Chute aux Chaudières” waterfall. The east bank (altitude 200 m) is an alluvial terrace with sand and gravel, whereas the west bank (altitude 160 m) and Juneau Island are characterised by loamy and clayey marine deposits, which were deposited when the region was covered by what is known as the Champlain Sea. The river bed is cut into the marine deposits to an altitude of around 125 m at Juneau Island, which is around 17-18 m lower with respect to the experimental site.

This site was selected for two reasons: (1) the site has an alley cropping system typical of the temperate climate zone, with hardwood trees planted at wide spacings and alleyways where agricultural, horticultural or companion crops are grown (Gold and Garrett, 2009); and (2) the alley cropping system was already an active research site for research on the contribution of multifunctional agroforestry systems to the climate change adaptation capacity of agro-ecosystems (professor Alain Olivier, Laval University).

The experimental alley cropping site is composed of a tree row with *Populus spp.* (hybrid poplar), another tree row with *Quercus rubra* (red oak), both planted in 2009, and within the alleyway *Phleum pratense L.* (common timothy) and *Trifolium pratense L.* (red clover), sown simultaneously in 2009. The alleyways are oriented NW-SE and are clearly visible in high resolution remote sensing imagery (figure below).

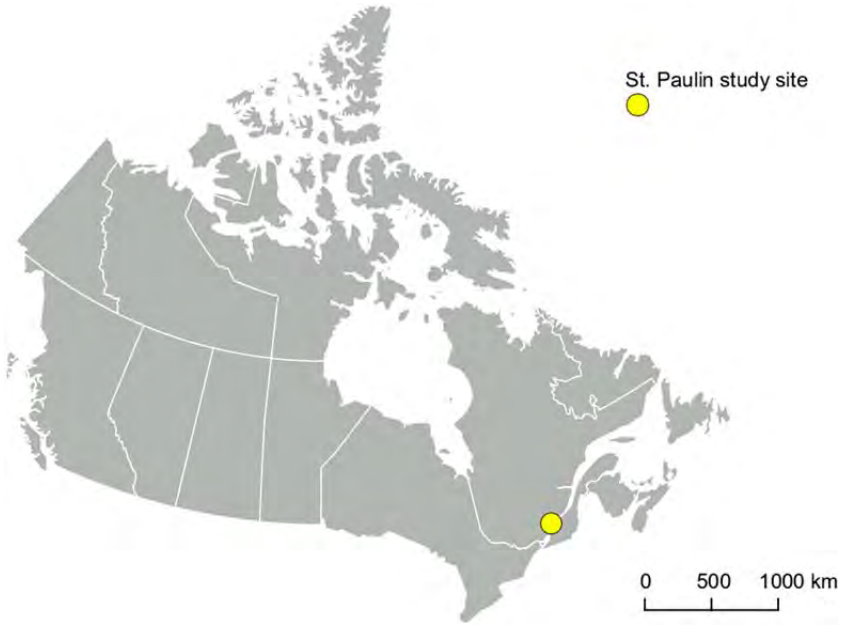

Figure 6. The location of the St. Paulin experimental alley cropping site within Canada.

Figure 7. Satellite image of the experimental alley cropping site near St. Paulin, Quebec (marked with the red frame; Cnes/Spot/Google). The NW-SE oriented lines within and below the indicated area are the alleyways with individual tree rows.

4.1.2 Particle size distribution (PSD)

An initial study was carried out by Bambrick *et al.* (2010) to determine the soil characteristics at the experimental site. They analyzed soil samples from one sample block in the western section of the field close to the Rivière du Loup, and found fractions of 79% sand by weight, 16% silt, 5% clay and pockets of sandy loam (56% sand, 30% silt and 14% clay). The soil was classified *in situ* as a dytric brunisol with pH 6.2 and moderate agricultural potential according to the Canadian Soils Classification System (Soil Classification Working Group, 1998).

In order to obtain the particle size distribution necessary for simulating the hydrology of the unsaturated zone at the experimental site, we extracted soil samples from within the alleyway, and assumed these were representative of the alley cropping system. The grain size analysis was based on the ASTM D-322 method (American National Standard Institute, 1972), as described by the Canadian Soil Survey Committee (McKeague, 1978). This method commends the dry sieving of the sand fraction precipitated after suspension. The organic matter content was determined by loss on ignition (LOI) at 375°C, as described by the Centre d'Expertise en Analyse Environnementale du Quebec. The particle size distribution, texture classes and organic matter content are given in the two tables below. Above a depth of 75 cm the soil is mostly sandy (up to 87-96% by weight) with smaller amounts of silt (2-8%) and clay (2-5%), which corresponds with the sandy soils found in this area by Bambrick *et al.* (2010). A clay loam layer below 110 cm contains up to 34% clay, which has a reducing effect on hydraulic conductivity. Organic matter content was highest within the first 35 cm below the surface (2.9-3.6 %).

Table 5. Particle size distribution (PSD) and organic matter for different depths below the alleyway of the experimental alley cropping site (analysis performed by M. Fossey).

	Soil separates (% weight)			Texture class	Organic matter (% weight)
Depth below surface (cm)	Sand (0.05 - 1 mm)	Silt (0.002 - 0.05 mm)	Clay (< 0.002 mm)		
0-15	87	8	5	Loamy sand	2.9
15-25	89	8	3	Sand	3.6
25-35	88	6	5	Sand	2.9
35-45	95	2	3	Sand	1.4
45-60	95	2	3	Sand	0.9
60-75	96	2	2	Sand	0.6
75-110	41	37	22	Loam	0.3
110-140	37	28	34	Clay loam	0.9

Table 6. Particle size distribution (PSD) of the sand fraction for different depths below the alleyway of the experimental alley cropping site (analysis performed by M. Fossey).

	Soil separates (% weight)				
Depth below surface (cm)	Very coarse sand (1 – 2 mm)	Coarse sand (0.5 – 1 mm)	Medium sand (0.25 – 0.5 mm)	Fine sand (0.1 – 0.25 mm)	Very fine sand (0.05 – 0.1 mm)
0-15	1	16	43	36	4
15-25	2	17	42	35	4
25-35	2	21	40	34	3
35-45	4	36	38	22	1
45-60	1	18	56	24	1
60-75	1	8	61	29	1
75-100	0	12	28	19	41
100-140	3	16	21	17	44

4.1.3 Root distribution (Bouttier, 2013)

A parallel study was carried out within the framework of this project by Bouttier (2013) in order to determine the spatial distribution of the fine roots of *Quercus rubra* and *Populus deltoides*, the species planted in the tree rows, and of forage vegetation in the alley. The analysis was limited to the first 100 cm below the surface, because this is the zone where fine roots traditionally extract most water. The root systems of *Quercus rubra L* and forage are spatially separated, and the root density of *Quercus rubra L* at 0-10 cm depth is 17% lower than for forage, but 22% higher at a depth of 10-20 cm. The high root density of *Populus deltoides* near the stem results in a 45% lower root density for forage in those locations, which suggests strong competition for water resources between these two types of vegetation. The study of agricultural output has furthermore revealed a reduction of forage biomass especially near *Populus deltoides*. Nevertheless, the results of a principal components analysis suggested that the effect of root competition on agricultural output is only secondary, with competition for light being the principal factor of influence. The influence of the fast-growing *Populus deltatoides* root system on forage is greater than that of *Quercus rubra L*.

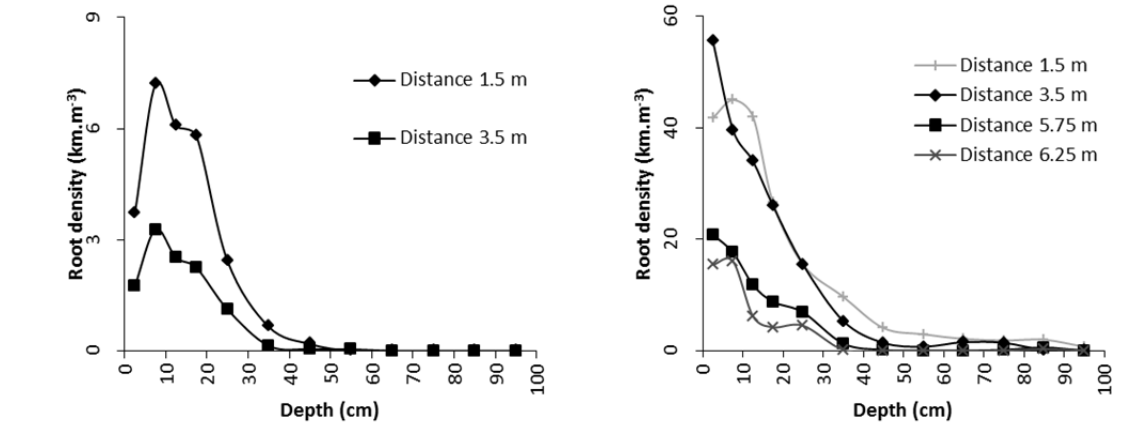

Figure 8. Fine root density of *Quercus rubra* (a) and *Populus deltoides* (b) as a function of depth below the surface and distance to the tree (Bouttier).

4.1.4 Weather data

A weather station (see figure below) was mounted in a suitable clearing at approximately 120 m from the alley cropping site (46°27'10.32"N 72°59'34.31"W) to measure air pressure, photosynthetically active radiation (400-700 nm), wind speed, wind direction, air temperature, relative humidity, and rainfall. Measurements were recorded every 15 minutes during the summer and autumn of 2011-2012. The following components were used to build the weather station:

- Monitoring: Independent monitoring system Onset Hobo U30 with space for a battery. This system operates under temperatures from -20 to 40 degrees C, has 10 Smart Sensor ports and 15 channels. Data are downloaded over a USB connection (mini-USB) using the Hoboware Pro software (Windows and MacOS). LEDs indicate system activity. Includes one 4 V 10.0 Ah battery (Power Sonic PS-4100).

- Power unit charged using one solar panel providing 1.2 W (Onset Solar).

- Relative humidity measurements: Onset S-THB-M002 Smart Sensor hygrometer for measuring relative humidity (1-100%) and temperature (-40 to 75 degrees C). Includes 2m cable.

- Wind speed and direction: Onset S-WCA-M003 combined anemometer and wind vane for wind speed between 0-44 $m.s^{-1}$ and wind direction between 0-358 degrees (wind speed threshold of 0.5 $m.s^{-1}$) mounted on an Onset M-CAB half cross arm attached to the tripod.

- Rain gauge: Onset S-RGB-M002 tipping bucket rain gauge (0.2 mm container), with 2 m cable.

- Atmospheric pressure sensor: Onset S-BPB-CM50 Smart Sensor for measuring barometric pressure from 660-1070 mbar with an accuracy of 0.1 mbar. Includes 50 cm connector cable.

- Sensor for photosynthetically active radiation (PAR): Onset S-LIA-M003 sensor for visible light between 400-700 nm, includes 3 m cable.

- Solar radiation shield: Onset RS3, protects relative humidity and air temperature sensors.

- The weather station was mounted on an Onset M-TPB-KIT, which includes a 2 m metal tripod (M-TPB), a mast level (M-MLA), guy wire kit (M-GWA), 1/2" stake kit (M-SKA) for guy wires, 1/4" stake kit (M-SKB) for tripod and a grounding kit (M-GKA).

Figure 9. The weather station used at the experimental alley cropping site at St. Paulin, Quebec in 2011 and 2012 (picture taken on 23/05/2012).

The table below shows the monthly statistics of precipitation and temperature. The summer of 2012 was particularly dry in the province of Quebec, with precipitation as low as 32.4 mm in July against 95.4 mm in the same month a year before. August 2012 was still dry for the time of the year with 82.2 mm, but September and October were regular months. The contrast with 2011 is remarkable, here August was a very wet month with 188.2 mm, and the wettest day measured during the 2011field campaign was August 10, with 69.2 mm. The distribution of precipitation events in the figure below shows that October 2012 had the most days with precipitation. The wettest day of the 2012 field campaign also occurred in October (56.2 mm on October 31).

Daily mean temperature from July to October was very similar in 2011 and in 2012, while the daily range between minimum and maximum temperature was greater in 2012. The warmest temperatures were measured on July 22, 2011 (32.3°C) and on July 13, 2012 (34.5°C).

Table 7. Monthly statistics calculated for 2011 and 2012 precipitation, average daily maximum (Tmax) and minimum (Tmin) temperature, and daily mean temperature at the experimental site.

Date	Precipitation (mm)		Daily Tmax (°C)		Daily Tmin (°C)		Daily mean T (°C)	
	2011	2012	2011	2012	2011	2012	2011	2012
May	-	63.2	-	20.0	-	6.5	-	13.5
June	-	136.4	-	24.6	-	10.7	-	17.5
July	95.4	32.4	27.8	28.0	12.9	12.1	20.4	20.0
August	188.2	82.2	24.6	26.4	12.1	12.5	18.1	19.0
September	110.4	153.8	21.3	20.4	8.6	5.8	14.6	12.9
October	96.8	158.6	13.0	13.6	2.5	2.7	7.6	8.0

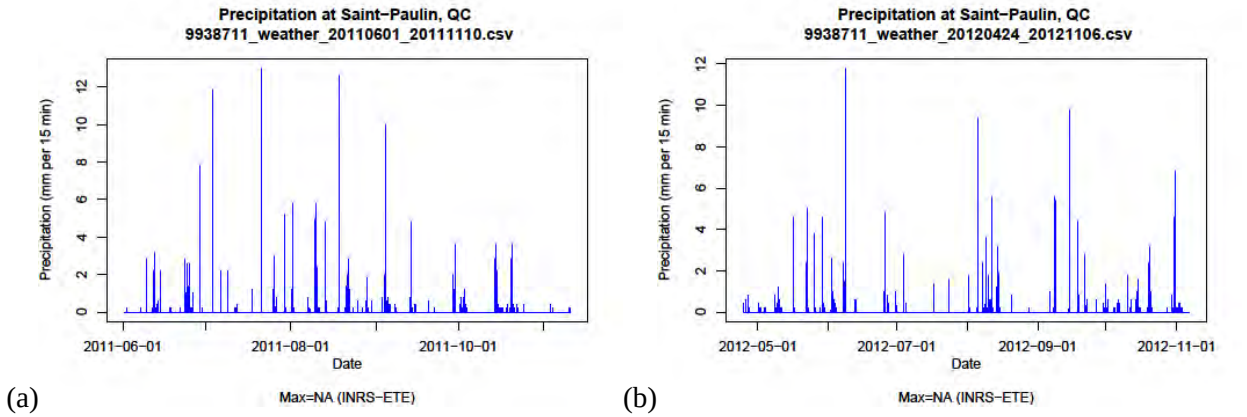

Figure 10. Seasonal distribution of precipitation events observed in 2011 (a) and 2012 (b) at the experimental site.

The figure below shows the wind roses calculated for the summer and autumn of 2011 and 2012 at one-minute intervals (a and b), and the direction of wind gusts for the same periods (c and d). The wind came mostly from N to NNW (cold air) and from SSW (Saint-Lawrence Valley). Recorded wind speeds are quite slow compared to wind speeds observed in regions closer to the sea, and can be classified as gentle breeze at most (maximum wind speed 6 $m.s^{-1}$, corresponding to Beaufort scale 3). Cold winds coming from NNW-NW were mostly light breezes with wind speeds up to 4 $m.s^{-1}$ (Beaufort scale 2-3). Wind gusts coming from SSE-ESE were strongest, with speeds up to 15-16 $m.s^{-1}$ (Beaufort scale 7).

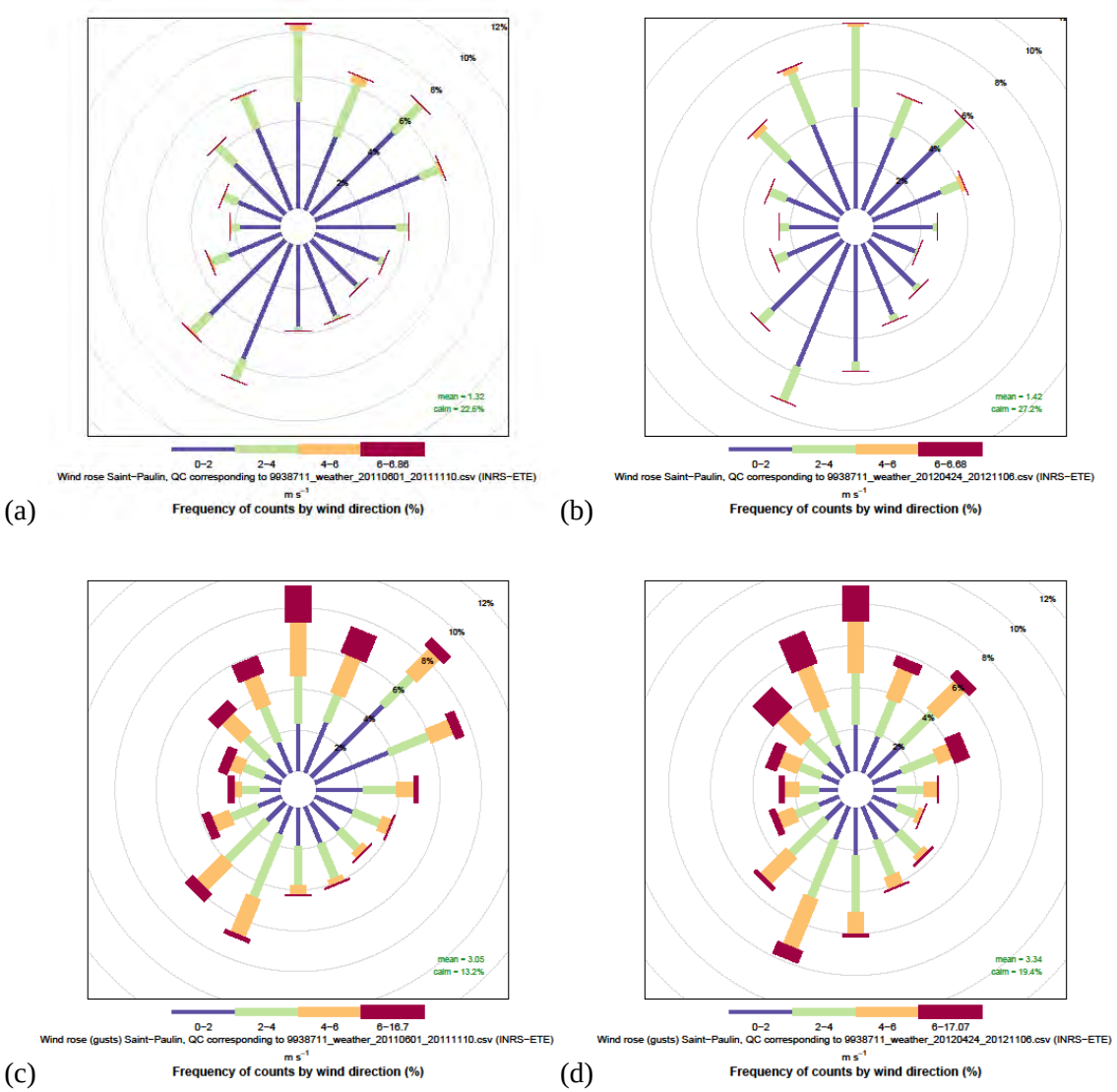

Figure 11. Wind roses calculated for the summer and autumn of 2011 (a) and 2012 (b) at one-minute intervals, and the direction of wind gusts for 2011 (c) and 2012 (d).

4.1.5 Soil moisture patterns measured with frequency domain reflectometry (FDR)

Forty-five frequency domain reflectometers of the type Onset S-SMD-M005 (see figure below) were used simultaneously to monitor volumetric water content within the first 100 cm of the soil along a transect perpendicular to the tree rows. The sensors were divided into 11 sets corresponding with a vertical profile, and inserted in the ground at depths of 7, 25 ,45, 75 and 100 cm (values correspond with the middle of the probe). FDR sensors in each set were installed in close proximity of one another (distance 18-22 cm) so that all sets combined provide a nearly two-dimensional soil moisture profile in the plane perpendicular to the tree rows (figures below). Soil moisture measurements were performed from 09/06/2011 to 10/11/2011 and from 25/04/2012 to 06/11/2012.

Figure 12. Frequency domain reflectometer (FDR sensor) Onset S-SMB-M005 with UTP connector cable.

Each sensor has a unique frequency around 70 MHz, and the distance between two sensors within one set was chosen such as to avoid signal interference (>20 cm). The high frequency circuit also reduces sensitivity to salinity. This, together with the probe length of 10 cm being a few centimeters longer compared to other more sensitive sensors, helps averaging out any variability in soil moisture patterns within 1 dm^3 of soil. The normal operation temperature of the sensors is between 0-50 degrees C. We used three independent Onset Hobo U30 monitoring systems. This system operates under temperatures from -20 to 40 degrees C, has 10 Smart Sensor ports and 15 channels. In combination with a Smart Sensor consolidator box and a power unit with a 85W solar panel and a deep cycle battery, it was possible to record the data of 45 FDRs with three monitoring systems. Data were sampled once per 15 minutes, based on the average value measured during the last minute of each 15 minute cycle. Data were downloaded over a USB connection (mini USB) using the Hoboware Pro software (Windows and MacOS). A LED indicates system status.

The sensors were installed as follows. First we drilled 45 holes in the ground using a hand auger with a 5 cm diameter. The shaft of each hole was cleaned during and after drilling using a soft brush. Subsequently, a metal rod with at one end an aluminum fork was used to pinch the soil at the bottom of the borehole in order to create room for the two pins of the probe. The FDR sensors were inserted vertically into the soil with the aid of a PVC tube in which we inserted the folded signal cable. Finally, the boreholes were filled with the same material that was removed before insertion.

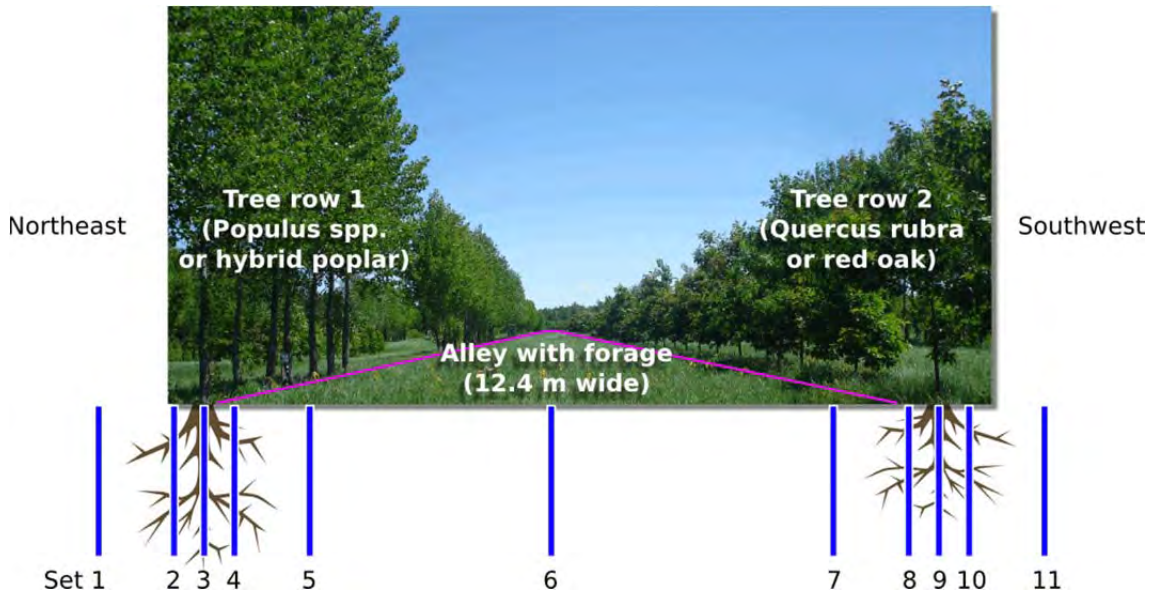

Figure 13. Transect of the FDR setup at the experimental alley cropping site (diagram not drawn to scale).

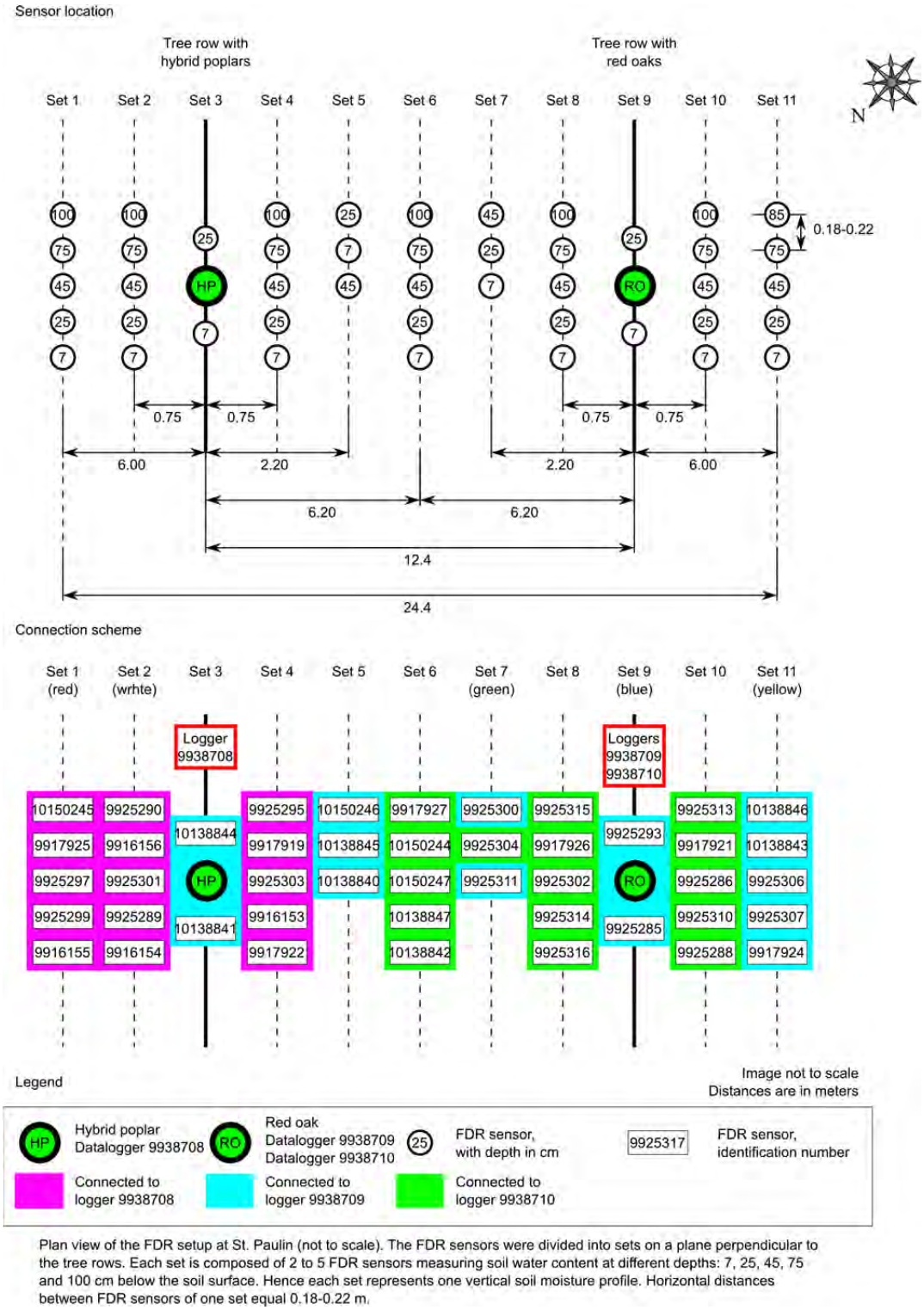

Plan view of the FDR setup at St. Paulin (not to scale). The FDR sensors were divided into sets on a plane perpendicular to the tree rows. Each set is composed of 2 to 5 FDR sensors measuring soil water content at different depths: 7, 25, 45, 75 and 100 cm below the soil surface. Hence each set represents one vertical soil moisture profile. Horizontal distances between FDR sensors of one set equal 0.18-0.22 m.

Figure 14. Plan view of the FDR setup at the experimental alley cropping site (not drawn to scale). The FDR sensors were divided into sets that are on a line perpendicular to the tree rows. Each set contains 2 to 5 sensors that monitor the volumetric water content at different depths: 7, 25, 45, 75 and 100 cm below the surface.

4.1.6 Description of experimental micro-watershed used for calibrating the erosion model

The experimental micro-watershed (2.4 km^2) used to calibrate the erosion model is a sub-watershed of the Bras d'Henri (150 km^2), which is itself part of the Chaudière watershed in the south of the province of Quebec. The Bras d'Henri is intensively farmed with an animal density of 4.7 animal units per hectare of farmland, illustrating the importance of livestock farming in the area. Pig farming is practiced on 59% of agricultural units in the watershed, beef and poultry production, 23% and 6% respectively.

Figure 15 shows the micro-watershed, situated directly south-east of St-Narcisse-de-Beaurivage. The micro-watershed follows the Bras d'Henri's trend in that it is intensively farmed, with very few wooded areas (mainly located south-west) covering 86% and 13 % of the total area, respectively. The remaining 3% consists of residential areas and farms located at the outskirt of the micro-watershed. Two main waterways separate the watershed drainage network, (branches 14 and 15) and converge at the outlet

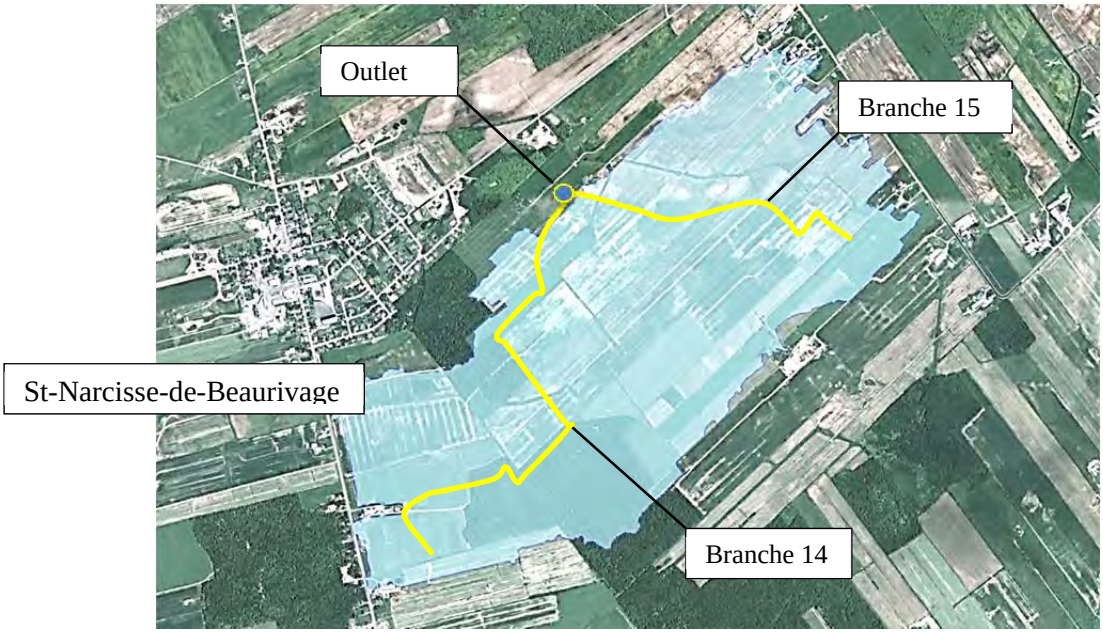

Figure 15. Satellite view of the micro-watershed at St-Narcisse-de-Beaurivage and the two main creek branches

The micro-watershed is mainly used for large-scale farming practices including corn (20%), oats (6%), soy (31%) and prairies (24%) (year 2012). A large proportion of soy was farmed with residues left from previous growing seasons (18% with residues, 13% without), and 3% of prairies were planted late, exposing bare soil longer than other cultures.

Table 8 shows the micro-watershed land cover in terms of area and percentage of use. Figure 21 shows the spatial distribution of land uses.

Table 8. Land use and corresponding area cover.

Occupation (type)	Area (km^2)	Occupation (%)
Unclassified	0.09	4%
Maize	0.50	20%
Oats	0.14	6%
Soy	0.33	13%
Soy (with residues)	0.45	18%
Prairies	0.52	21%
Prairie (late growth)	0.07	3%
Forest	0.32	13%
Urban	0.05	2%

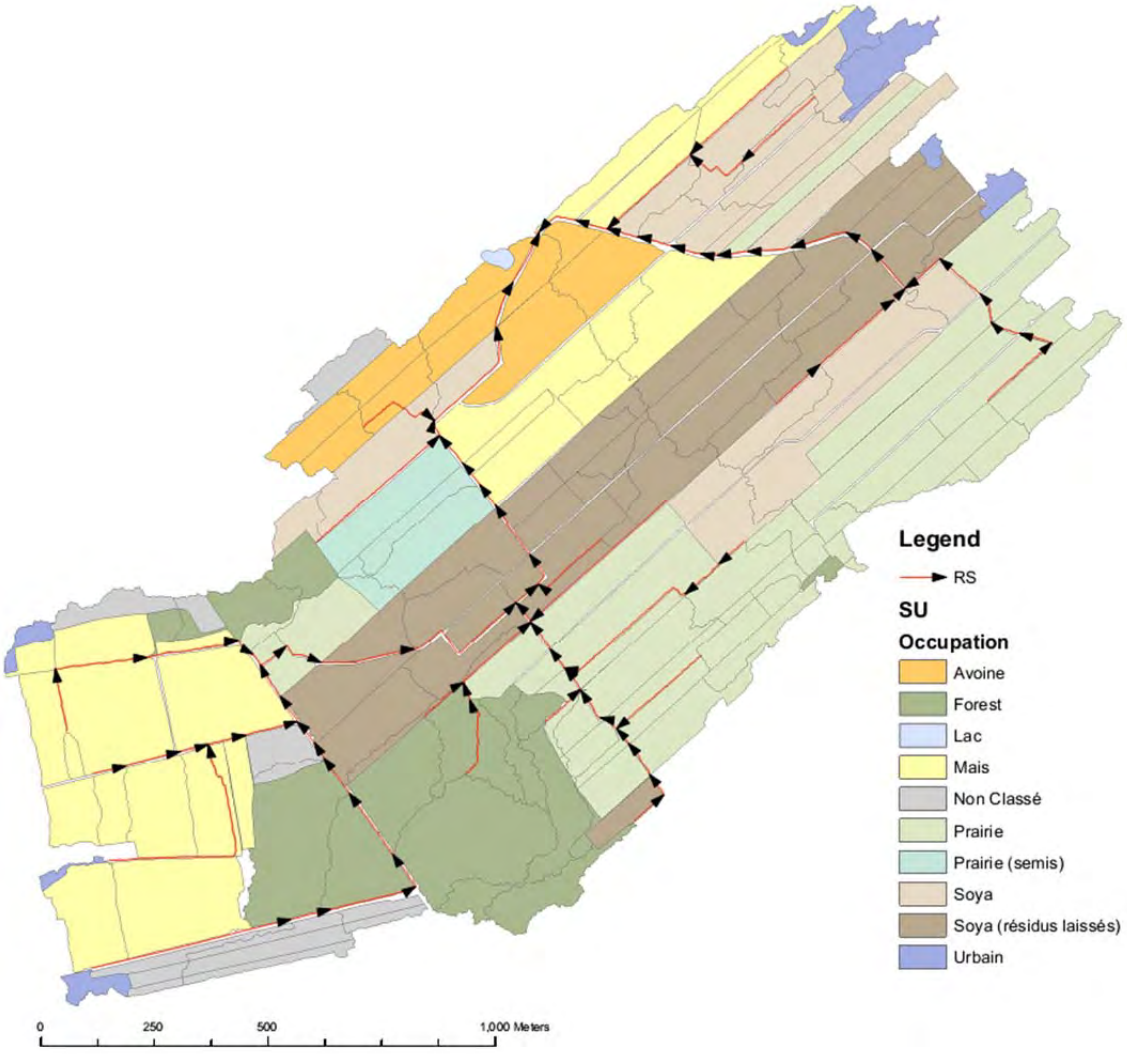

Figure 16. Map of hydrological units (SU and RS) and land use

Soil types found at the surface are mainly limited to loamy sands and sandy loams. The table below shows the different types of soils and their properties, identified by a soil survey conducted in 2007 by AAFC. Finally, Appendix C provides a detailed soil map and specific to each type of soil found in the micro-watershed properties.

Table 9. Soil types found in the micro-watershed.

Sols		Classification taxonomique (Sous-groupe)	Granulométrique de la famille	Drainage	Superficie (ha)
Code	Nom				
ALL	Alluvions	Gleysol humique orthique	Loameux	Mal drainé	4.53
BE	Breault	Podzol humo-ferrique gleyifié	Loameux-grossier	Imparfaitement drainé	4.95
BS	Le Bras	Gleysol humique orthique	Loameux	Mal drainé	45.84
BSa	Le Bras, variante calcaire	Gleysol humique orthique	Loameux	Mal drainé	30.43
BSl	Le Bras, substratum loameux	Gleysol humique orthique	Loameux	Mal drainé	3.22
BV	Beaurivage	Podzol humo-ferrique gleyifié	Sableux	Imparfaitement drainé	42.01
BVb	Beaurivage, variante brunisolique	Brunisol sombrique gleyifié	Sableux	Imparfaitement drainé	21.82
BVs	Beaurivage, squelettique sableux	Podzol humo-ferrique gleyifié	Squelletique-sableux	Imparfaitement drainé	42.38
DS	Des Saults	Gleysol orthique	Loameux-grossier	Mal drainé	1.73
DSa	Des Saults, variante calcaire	Gleysol orthique	Loameux-grossier	Mal drainé	8.70
DT	Dosquet	Podzol humo-ferrique gleyifié	Loameux-grossier	Imparfaitement drainé	0.00
FC	Fourchette	Gleysol humique orthique	Sableux	Mal drainé	2.23
JU	Saint-Jude	Podzol humo-ferrique gleyifié	Sableux	Imparfaitement drainé	11.99
MA	Mawcook	Gleysol humique orthique	Loameux-grossier	Mal drainé	5.41
NE	Neubois	Podzol humo-ferrique gleyifié	Loameux	Mal drainé	6.30
NEl	Neubois, substratum loameux	Podzol humo-ferrique gleyifié	Loameux	Imparfaitement drainé	3.05
OR	Des Orignaux	Brunisol dystrique gleyifié	Loameux-grossier	Imparfaitement drainé	1.59
PI	Des Pins	Podzol humo-ferrique gleyifié	Loameux-grossier	Mal drainé	25.58
SE	Séraphine	Gleysol humique orthique	Sableux	Mal drainé	5.10
SM	Saint-Samuel	Gleysol humique régosolique	Sableux	Mal drainé	4.47
SMa	Saint-Samuel, variante calcaire	Gleysol humique régosolique	Sableux	Mal drainé	1.84
VA	Valère	Podzol humo-ferrique gleyifié	Sableux	Imparfaitement drainé	25.89
TN/S	Humisol sur matériau sableux	Humisol terrique	Humisol sur sableux	Très mal drainé	4.10
NC	Non classifié	-----	-----	-----	53.96

4.1.7 Data used for calibrating the erosion model

Calibration and validation require simulated and measured values of flow rates as well as sediment flux during several rainfall events. To this end, a measurement campaign during the major rainfall events of summer and fall 2012 was undertaken (from 4 July to 19 October 2012). For each rainfall event, precipitation, flow rate and total suspended solids (TSS) were recorded.

4.1.7.1 Rainfall

Precipitation was measured with a tipping bucket rain gauge installed on a weather station at the outskirts of the micro-catchment. Data was recorded continuously during the entire period of the measurement campaign. Monique Bernier's team (INRS) operated the rain gauge used for this study. Data available at this station has an hourly resolution and were stored in a database via modem. According to previous uses of MHYDAS-Erosion, a one hour resolution is adequate to validate simulation results Gumiere *et al.* (2010).

4.1.7.2 Flow rate

As mentioned in **section 4.1.6**, two major branches run through the micro-catchment (branches 14 and 15) and meet near the outlet. Flow rates were measured at three sites, one downstream, and two upstream from the junction, respectively on branches 14 and 15. Mass balances between both branches and the outlet could be compared to check for consistency between measured results. In this report, only values reported for the outlet are discussed. Figure 17 shows the sampling location at the micro-catchment outlet.

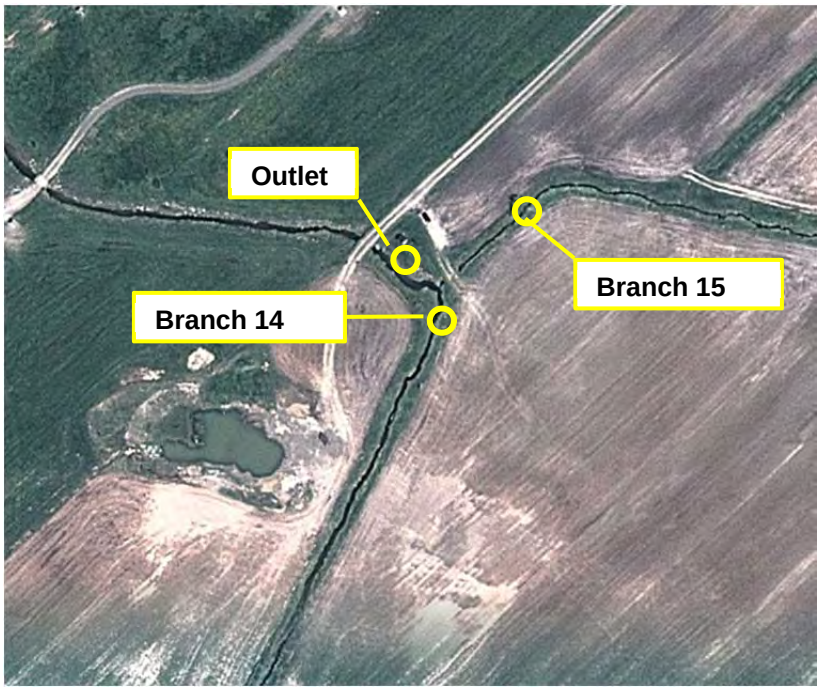

Figure 17. Sampling locations at the outlet of the micro-watershed.

Flow rates were not measured directly, but were derived using a rating curve. This method involves the use of a regression curve between measured water heights in a channel with known dimensions, and measured flow rate. Unlike a hydraulic structures designed for this purpose such as a triangular weir, the measurement site is located in a natural section of the drainage network near the outlet, with a non-uniform section. Furthermore, the channel dimensions vary throughout the season depending on the stage of plant growth within the channel and sediment transport.

Manual measurements of flow rate and water level were taken every two weeks during the summer and fall periods by AAFC technicians. Following a preliminary analysis, we developed a regression function to establish the relationship between water level and flow rate (logarithm of a power function):

$$\ln(Q) = \beta_0 + \beta_1 \ln(h)$$

Where h is the daily average height (m), Q is the average daily flow rate (L/s) and β_1, β_2 are constants. A simple linear regression was established between the water level and flow and regression parameters were estimated by the least-squares method. Figure 18 shows the rating curve at the outlet for the growth

season 2012. A detailed description of the method used to generate the rating curve can be found in Appendix D.

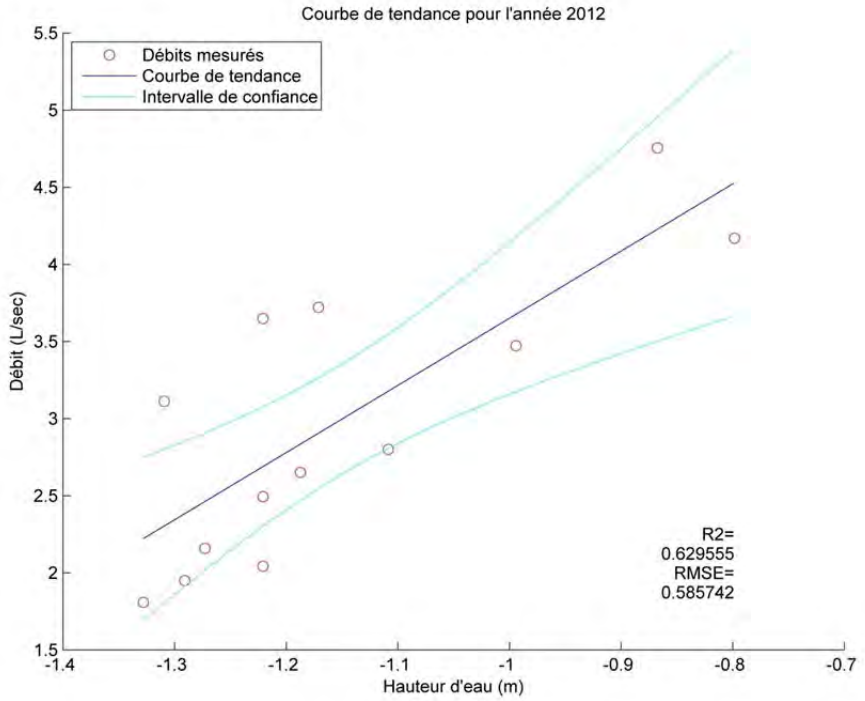

Figure 18. Rating curve defining the relationship between water height and discharge at the catchment outlet for the growth season of 2012

Water height was measured with an ultrasonic probe (Ultrasonic 710, see Figure 19). An average of the measured heights was recorded every 15 minutes during the measurement campaign. The ultrasonic module is attached to a metal frame directly above the riverbed.

Figure 19. Ultrasonic module (module 710) used at the catchment outlet for measuring water height.

4.1.7.3 Total suspended solids (TSS)

Total suspended solids measurements are essentially a snapshot of the amount of suspended matter in a known volume of water. Using the flow rate, it is thus possible to estimate at the sample collection time the sediment flux at a given site. This section briefly describes the procedure to measure sediment flux.

Water samples were taken at the same sampling site as water height measurements. As for flow rates, only measurements at the outlet are discussed in this report. The USGS (United States Geological Survey) suggests many different sample collection methods to take into account the spatial variability of TSS caused by irregularities in the channel section. Because the channel section at the sampling site is small, a one-liter composite of four (250 ml sub-samples) was taken for each measurement. Figure 20 shows a cross sectional schematic of sub-sample positions for TSS measurements suggested by the USGS guide.

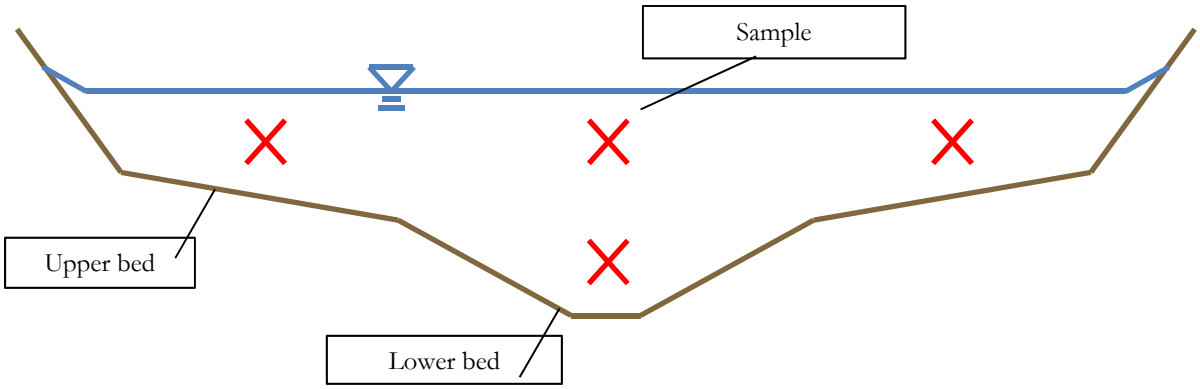

Figure 20: Cross section of the channel with the sample locations used for TSS measurements (marked with *X*).

Each sub-sample was taken manually with a perch equipped with a 250-ml bottle, at intervals of 30 minutes or one hours depending on rainfall and the number of bottles available. Manual sampling was the preferred method, as opposed to an automatic sampling, for the following reasons:

- Samples can be taken at several locations in the river and form composites, better representing sediment flux in the entire section.

- Elimination of risk of failure or obstruction of the automatic sampling device during an event. As measurements are made during the events causing more sediment transport, the risk of a pump failure or obstruction is increased.

Samples were taken throughout the event to properly cover the rise and fall of sediment transport, thus facilitating model calibration. Appendix E presents two photographs showing the sample collection apparatus.

The total mass per sample volume was measured using fiberglass 45 microns filters, according to the USGS guide. Volumes ranging from 300 ml to 1 l for each sample were filtered (depending on the speed at which the filter clogged) to minimize the error caused by smaller total mass values.

4.1.7.4 Sediment flux

Sediment flux is simply calculated by multiplying the TSS values by flow rate rates found with the rating curve, using the following equation:

$$q = TSS * Q$$

Where q is sediment flux (mg/s), TSS total suspended solids (mg/l), and Q flow rate (l/s).

4.1.7.5 Digital elevation map

As discussed in **section 3.2.2**, topological SU-SU and SU-RS links are derived using PHYSITEL from a high precision DEM (LIDAR). The DEM was provided by IRDA (Institut de recherche et de développement en agroenvironnement) with a 1-m spatial resolution. The micro-watershed has a relatively flat topography with a maximum slope of 3.2% near branch 14 closed to the outlet, and at the watershed head, south. Figure 21 shows a slope map for the studied watershed. Note that the small lines of high slope values seen in the south are trails in a wooded area and not actually large slopes.

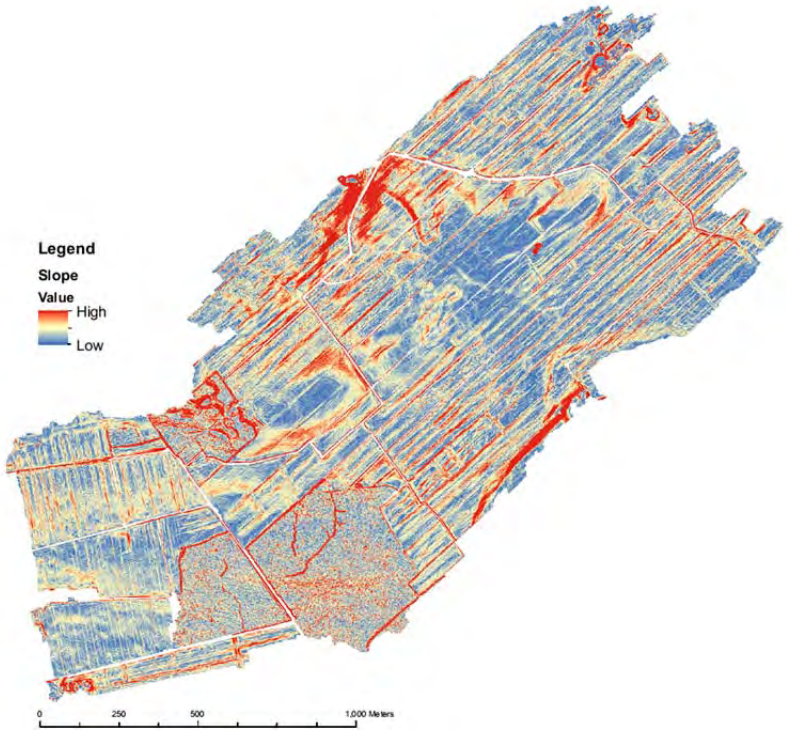

Figure 21: Slope map of the micro-watershed near St-Narcisse-de-Beaurivage.

4.2 Methods

4.2.1 Simulating future climate for the experimental alley cropping site

The input for the model of water movement in the soil includes precipitation and potential transpiration. These variables can be either measured directly (precipitation), calculated from weather observations (potential transpiration) or estimated from climate simulations for future time periods. The approach for estimating future climate conditions was based on:

1. Selection of the most relevant regional climate simulations for 2041-2070 (cluster analysis);

2. Downscaling of global climate simulations to the regional scale (dynamical downscaling);

3. Calculating the 30-year monthly differences (or deltas) between precipitation, maximum temperature (Tmax) and minimum temperature (Tmin) between 1971-2000 and 2041-2070.

These steps involve the regional scale of the southern part of the Quebec province, and were carried out by the Ouranos Consortium on Regional Climatology and Adaptation to Climate Change. The monthly deltas found for the regional scale were subsequently projected on the experimental alley cropping site at St. Paulin, Quebec. The approach for this part of the study was as follows:

4. Analysis of the distributions of daily precipitation, Tmax and Tmin at the experimental site and at three nearby locations for which weather data were available;

5. Perform linear regression of cumulative precipitation, Tmax and Tmin at Shawinigan and at St. Paulin; likewise for values measured at St. Charles de Mandeville and at St. Paulin; and likewise for values measured at Quebec City airport and at St. Paulin;

6. Reconstruction of a 1967-1996 reference dataset with daily P, Tmax and Tmin using the linear models resulting from the preceding step;

7. Simulation of the 2041-2070 climate using reference dataset and deltas (constant scaling).

8. Calculation of potential transpiration with the Penman-Monteith equation (Penman, 1948; Monteith, 1981; Allen *et al.*, 1998).

4.2.1.1 Selection of the most relevant regional climate simulations (Ouranos)

A total of 102 global and regional climate simulations were available for the southern part of Quebec in a database managed by Ouranos Consortium on Regional Climatology and Adaptation to Climate Change. Ouranos performed a cluster analysis resulting in a selection of five simulations of expected climate change for the period 2041-2070:

- CGCM_3.1 A1b with a 3.75 x 3.75 degree coverage (regional simulation)

- CNRM-CM_3 A1b with a 2.8 x 2.8 degree coverage (regional simulation)

- MIROC_3.2-medres A1b with a 1.4 x 1.4 degree coverage (regional simulation)
- MRI-CGCM_2.3.2a A1b with a 2.8 x 2.8 degree coverage (regional simulation)
- CGCM_3.1.3 A2, downscaled from CRCM_4.2.3 and with a 45 x 45 km coverage (downscaled from a global simulation)

These five simulations explain 74.5% of the variance of the following variables: minimum temperature (Tmin), maximum temperature (Tmax), net incoming shortwave solar radiation at the earth surface (Sn), precipitation (P) and relative humidity (RH).

4.2.1.2 Dynamical downscaling of global climate simulations to the regional scale (Ouranos)

After the selection of five climate scenarios, the global simulations in the selection were downscaled to the regional scale and averaged. The boundary conditions of regional-scale computational domains were based on the predictors of global climate models (GCMs with ~200x200 km tiles), and obtained for the watershed scale by means of (Mpelasoka and Chiew, 2009) (i) empirical downscaling of historical data informed by GCM simulations, (ii) statistical downscaling of GCM predictors, or (iii) by dynamic downscaling of GCM predictors using regional climate models (RCMs). Statistical and dynamic downscaling methods are often preferred for two reasons: firstly, they can account for changes in the weather characteristics and synoptic patterns that may apply for future climate, and secondly, GCMs are not optimized for the purpose of simulating convective rainfall but rather for simulating large-scale atmospheric patterns.

The approach defined for our dynamical downscaling of GCMs to the regional scale was based on the approach followed for simulations of the Canadian Regional Climate Model (CRCM; Caya and Laprise, 1999; Music and Caya, 2007).

4.2.1.3 Monthly deltas for the southern part of Quebec (2041-2070 vs. 1971-2000) (Ouranos)

Using the five regional climate simulations and downscaled GCMs, Ouranos calculated the simulated differences (or deltas) for the monthly average of each of the aforementioned variables with respect to a given reference period, which in this case is the 30-year period between 1971-2000. Also known as constant scaling, this method involves offsetting or multiplying the amplitude of the simulated signal with a value that minimizes the root mean square error between observed and simulated signal. Since this only works when the time interval of observed and simulated signals correspond, this method limits the minimum possible sample interval of a bias-corrected simulation to the sample interval used by the weather station that provides the observations.

The resulting 12 deltas per variable are in essence factors with no units, with value 1 meaning “no change simulated.” The advantage of expressing simulated change in factors rather than in absolutes is that negative values for solar radiation, precipitation, relative humidity are avoided. For temperature however, which in centigrade can be either positive or negative, the deltas were calculated as absolute values, with value 0 meaning “no change simulated.”

As the table below shows, deltas were not significant for rainfall, solar irradiance, wind speed and relative humidity because the range between the highest value of these variables simulated for one scenario and

the corresponding lowest value for another scenario was greater than the average of both. In other words, there is a large discrepancy between the outcomes of the climate simulations selected after the cluster analysis. Simulated changes in wind speed were not significant for our study for an entirely different reason also. Monthly average wind is much more variable in space and time than the aforementioned meteorological variables due to the local relief. Deltas for Tmax and Tmin on the other hand were significant for at least 8 months during the year and therefore we simulated a 2041-2070 weather dataset for St. Paulin based on these deltas. We also simulated changes in rainfall, although these changes were not significant at any time.

Table 10. Monthly deltas and uncertainties of climate variables simulated for 2041-2070 for the southern part of Quebec with respect to 1971-2000 observations (Ouranos, 2012). The deltas were calculated with the constant scaling method and based on five different climate simulations, and are presented here as a change factor (-) or for temperature, as a change in centigrades. The statistically significant changes are underlined.

Month of year	Change between 2041-2070 and 1971-2000					
	Rainfall (-)	Daily Tmax (°C)	Daily Tmin (°C)	Solar irradiance (-)	Wind speed (-)	Relative humidity (-)
1	1.18 ± 0.43	3.26 ± 3.40	**4.20 ± 4.13**	0.95 ± 0.22	0.97 ± 0.17	0.98 ± 0.04
2	1.21 ± 0.51	**2.58 ± 1.61**	**3.42 ± 3.30**	0.95 ± 0.12	1.09 ± 0.15	0.98 ± 0.04
3	1.06 ± 0.31	2.33 ± 4.70	2.90 ± 5.24	0.97 ± 0.13	1.04 ± 0.12	1.00 ± 0.06
4	1.14 ± 0.17	2.84 ± 3.97	2.89 ± 3.45	0.96 ± 0.07	0.97 ± 0.34	1.04 ± 0.11
5	1.14 ± 0.39	2.16 ± 3.56	2.44 ± 3.01	0.98 ± 0.09	0.93 ± 0.30	1.01 ± 0.04
6	0.99 ± 0.11	**2.43 ± 1.66**	**2.54 ± 1.38**	1.02 ± 0.03	1.01 ± 0.24	1.00 ± 0.01
7	0.95 ± 0.15	**2.48 ± 2.13**	**2.41 ± 1.70**	1.04 ± 0.07	0.96 ± 0.13	0.99 ± 0.06
8	0.94 ± 0.21	**2.90 ± 2.68**	**2.84 ± 1.81**	**1.07 ± 0.04**	0.87 ± 0.33	0.99 ± 0.02
9	1.01 ± 0.23	**2.80 ± 2.06**	**2.70 ± 1.70**	1.05 ± 0.09	0.93 ± 0.16	0.99 ± 0.03
10	1.11 ± 0.22	**2.88 ± 1.76**	**2.63 ± 1.37**	1.01 ± 0.15	0.99 ± 0.22	1.00 ± 0.04
11	1.17 ± 0.20	**2.83 ± 2.42**	**2.92 ± 1.94**	0.95 ± 0.10	0.99 ± 0.18	1.02 ± 0.06
12	1.19 ± 0.20	**2.89 ± 2.43**	**3.74 ± 3.73**	0.94 ± 0.23	1.00 ± 0.15	0.98 ± 0.04

4.2.1.4 Weather data used for the local climate simulation for the experimental site

The following locations were selected: the St. Paulin experimental site itself, Shawinigan (24 km from the experimental site), St. Charles de Mandeville (at 32 km) and Quebec City airport (136 km). St. Paulin data were available at 15-min time intervals, and were aggregated to 24 hours to allow for a comparison with the data from the other three locations (provided by Environment Canada). Because data for these locations are not always continuous we also used the high quality weather data from Quebec City airport.

Table 11. Properties of the weather stations used for creating a reference dataset for St. Paulin. The last column indicates which data was used in the regression analysis and which data was used for creating the reference dataset.

Name	Coordinates	Elevation (m)	Distance to experimental site (km)	Environment Canada climate identifier	Period
St. Paulin experimental site	46°27' N 72°59' W	140.00	-	-	2011-2012 (regression)
Shawinigan	46°56' N 72°73' W	110.00	23.68	7018001	2011-2012 (regression)
Shawinigan	46°57' N 72°75' W	121.90	22.75	7018000	1967-1996 (reference)
St. Charles de Mandeville	46°35' N 73°35' W	167.60	31.73	7016960	1967-1996 (regression) 2011-2012 (reference)
Quebec/Jean Lesage Intl Airport	46°80' N 71°38' W	60.00	135.57	701S001	2011-2012 (regression)
Quebec/Jean Lesage Intl Airport	46°80' N 71°38' W	74.40	135.32	7016294	1967-1996 (reference)

4.2.1.5 Simulation of local climate in 2041-2070 (constant scaling)

The weather record of the St. Paulin experimental site covers July-October 2011 and May-October 2012. In order to obtain an estimation of daily precipitation, Tmax and Tmin for the future period 2041-2070, we first had to obtain a 30-year reference dataset for St. Paulin to which we could apply the monthly deltas calculated by Ouranos. We characterized the distributions of daily precipitation, Tmax and Tmin at St. Paulin and, because most stations in the area do not have a continuous dataset, we analyzed data for three locations with a 30-year record covering more or less the period 1971-2000, which is the period for which the Quebec deltas were calculated. We subsequently performed a linear regression in order to establish the relationship between cumulative precipitation, Tmax and Tmin measured at St. Paulin in 2011-2012 and at these three locations, assuming that the estimated linear models could be used to obtain estimations of daily precipitation, Tmax and Tmin at St. Paulin for past dates and, eventually, for the 2041-2070 climate simulation.

4.2.2 Parameterization of HYDRUS and simulation of 2011-2012

In order to determine water availability for *Populus spp*. (hybrid poplar), *Quercus rubra* (red oak) and the intercrop (forage), we simulated the soil water dynamics around the root system in response to precipitation and potential evapotranspiration based on vegetation-specific water stress response characteristics (Wesseling, 1991) and potential uptake rates (Hinckley *et al*., 1994; Hadley *et al*., 2008). Two scenarios were defined:

- Scenario a: Observed field situation and local weather data for the summer and autumn of 2011;
- Scenario b: Observed field situation and local weather data for the summer and autumn of 2012.

The spatial domain and the hydraulic characteristics were considered the same for both scenarios, and therefore the only difference between the scenarios was the initial distribution of water content, input from precipitation and output by evapotranspiration. The simulation period was 153 days, corresponding with the period between 2011-06-03 and 2011-11-03 (scenario a), and the period between 2012-06-03 and 2012-11-03 (scenario b), respectively. These start to end dates were selected because they define the period for which weather observations were available for both years. We used a four-layer representation of the first 300 cm of the soil. *Populus spp*. had a maximum rooting depth of 95 cm with a maximum root density at 7.5 cm, which for *Quercus rubra* was 55 cm and 7.5 cm depth, respectively (Bouttier, observed in summer 2011). Forage was assumed to have a maximum rooting depth of 30 cm. Vegetation growth and root growth were not accounted for. In the sections that follow we will explain the model properties in more detail.

4.2.2.1 Computational domain defined for the alley cropping system

The two-dimensional computational domain of the transect of the alley was subdivided into three subdomains corresponding with the root system of the three vegetation types (see figure below), *i.e. Populus spp.* (extending 3 m to each side), *Quercus rubra* (also extending 3 m to each side), and forage (width of subdomain 6.4 m), where the first two are the trees that constitute the tree rows and forage is the vegetation grown within the alley. The vertical height of the domain equals 3 m. A finite element mesh was generated for the three subdomains, with a target element size of 20 cm on average and 10 cm at the upper boundary (see figure on next page).

The lower boundary and side boundaries of each subdomain were assumed impermeable, while time-dependent precipitation and potential evapotranspiration fluxes were applied to the upper boundaries. In this way we approximate the field situation with a semi-open system.

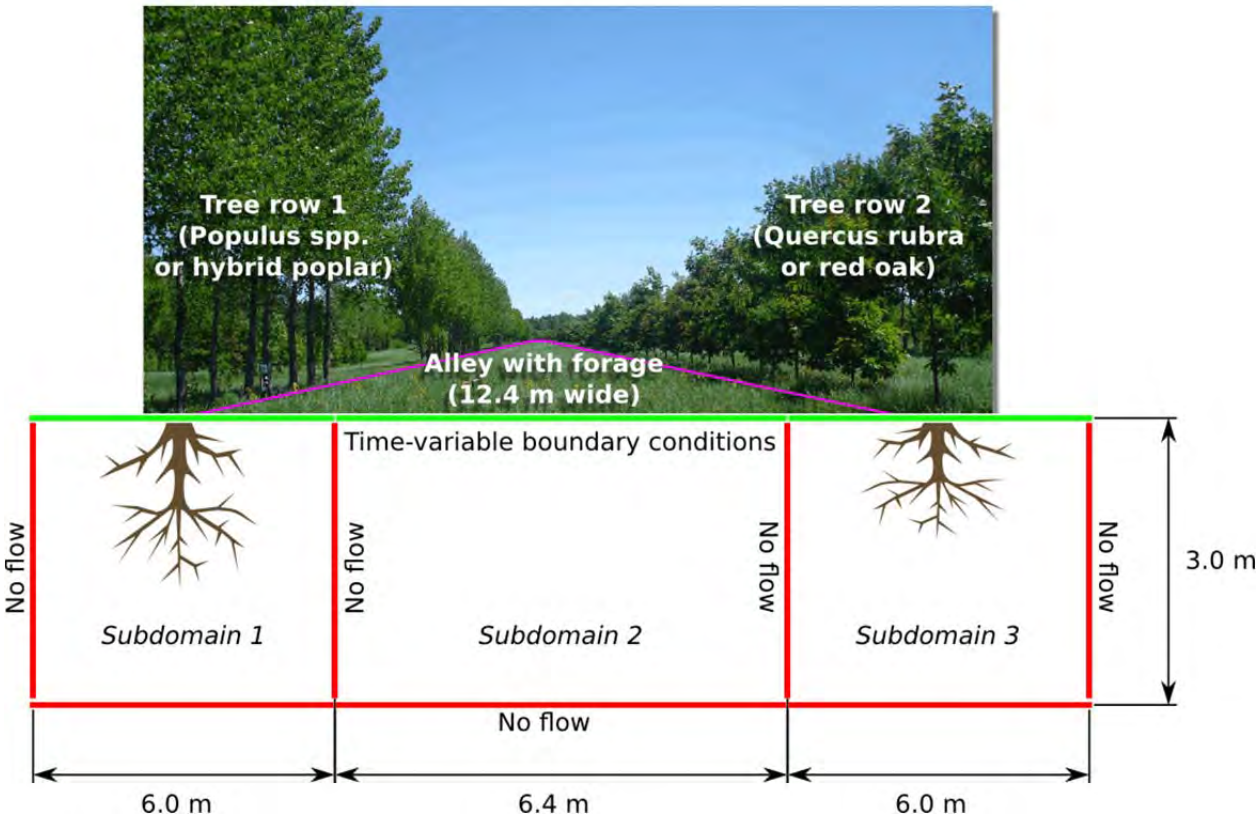

Figure 22. Subdivision of the alley transect into three subdomains corresponding with the three vegetation types, which are from left to right *Populus spp.* (tree row 1), forage (alley) and *Quercus rubra* (tree row 2) (diagram not drawn to scale).

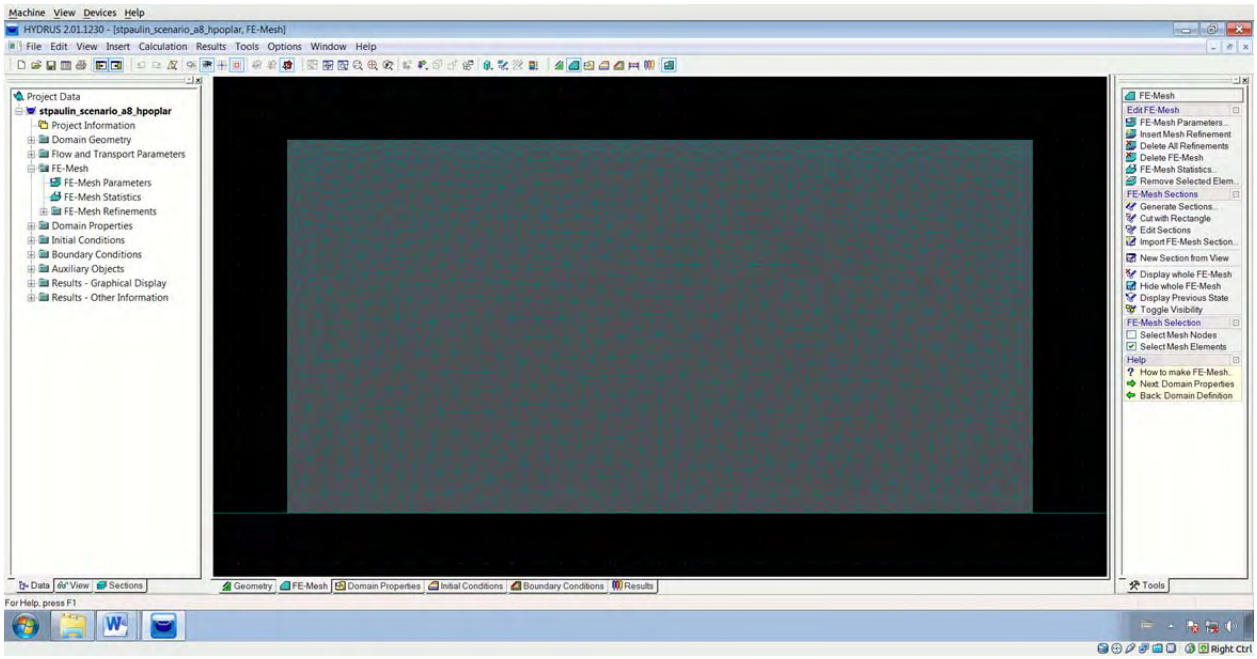

Figure 23. Finite element mesh for the *Populus spp.* subdomain.

4.2.2.2 Hydraulic parameters of the soil

We divided each subdomain in four horizontal layers (see figure below) that correspond with the soil layers that were identified using the particle size distribution: loamy sand between a depth of 0-15 cm, sand between 15-75 cm depth, loam between 75-110 cm depth, and clay loam between 110-140 cm depth. These layers were assigned different hydraulic parameters based on Rawls *et al.* (1982), who used multiple linear regression to estimate the Brooks-Corey parameters from a database of 2,540 soil layers; for the unsampled part of the domain between 140-300 cm we assumed water flow parameter values for clay. The table below gives the used parameter values.

Table 12. Values of soil hydraulic parameters (values based on Rawl *et al.*, 1982).

Depth below surface (cm)	Texture class	Residual water content θ_r (-)	Water content at saturation θ_s (-)	Parameter α in the soil water retention function (-)	Parameter n in the soil water retention function (-)	Hydraulic conductivity at saturation K_s (mm/hr)
0-15	Loamy sand	0.057	0.41	0.1	0.2	14.5917
15-75	Sand	0.045	0.43	0.1	0.2	29.7
75-110	Loam	0.078	0.43	0.1	0.2	1.04
110-140	Clay loam	0.095	0.41	0.1	0.2	0.26
140-300	Clay loam (assumed)	0.095	0.41	0.1	0.2	0.26

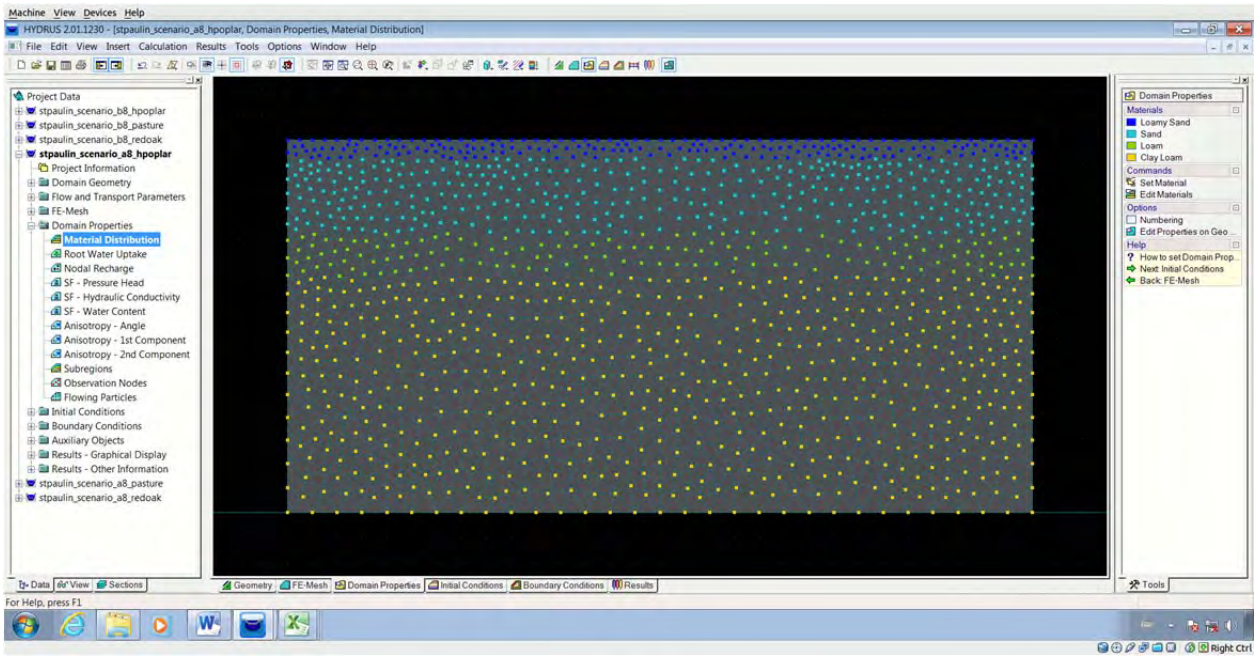

Figure 24. Material distribution for the *Populus spp.*, forage and *Quercus rubra* subdomains with from top to bottom loamy sand, sand, loam and clay loam (here shown for *Populus spp.*).

4.2.2.3 Hydraulic and distribution parameters of the root system

The Feddes linear water stress response function was parameterized according to values found in literature for air-entry pressure, field capacity, wilting point, permanent wilting point, potential uptake rate, maximum rooting depth and depth of maximum root density (see table below). The spatial distribution of the root system was represented by assigning a value of relative root density between 0-1 to each computational node. The root density of *Populus spp.* and *Quercus rubra* is assumed 0 at the surface, and increasing linearly to value 1 at the depth of maximum root density, which is 7.5 cm for *Populus spp.* and *Quercus rubra*. Beyond the depth of maximum root density, the root density decreases again to 0 at the maximum rooting depth of 95 cm and 55 cm for *Populus spp.* and *Quercus rubra*, respectively. For forage growing within the alley we assumed that the maximum rooting depth is at the surface, and decreasing linearly to a maximum rooting depth of 30 cm.

Table 13. Hydraulic and distribution parameters of the root system with values based on Wesseling *et al.* (1991) (denoted [*]), Hinkley *et al.* (1994) (denoted [**]), Hadley *et al.* (2008) (denoted [***]) and Bouttier (personal communication, denoted [****]).

Vegetation	Air-entry pressure h_1 (cm)	Field capacity h_2 (cm)	Wilting point h_3 (cm)	Permanent wilting point h_4 (cm)	Potential uptake rate S_p (cm/hr)	Maximum rooting depth (cm)	Depth maximum root density (cm)
Populus spp.	-10[*]	-25[*]	-500[*]	-8000[*]	0.02[**]	95[****]	7.5[****]
Quercus rubra	-10[*]	-25[*]	-500[*]	-8000[*]	0.0167[***]	55[****]	7.5[****]
Forage	-10[*]	-25[*]	-200[*]	-8000[*]	0.01	30	0

4.2.2.4 Initial distribution of water content

The distribution of volumetric water content at starting dates 03/06/2011 and 03/06/2012 were obtained by linear interpolation of FDR data sampled on 29 different locations within the transect (see the two figures below). Note how on 03/06/2011 the soil tends to be wetter close to the surface near the hybrid poplar and the red oak (x=6 m and x=18.4 m), and drier toward the alley between both trees. The alley section (between x=6 m and x=18.4 m) does not retain quite as much water as the tree root systems to the left and right of this section. On the same date one year later (03/06/2012) only the 14 FDR sensors below *Populus spp.* were live, so in order to obtain the initial conditions for the *Quercus rubra* and forage subdomains to the right of *Populus spp.* we used a characteristic vertical profile based on 2011 and 2012 data. We observe a dry zone (theta=0.05) at the bottom of the root zone (x=6 m and y=0.2 m, which equals 80 cm below the surface), while a zone with the same water content is found at a depth of 100 cm further away from the tree at x=0 m. This pattern is likely the result of root uptake by the tree.

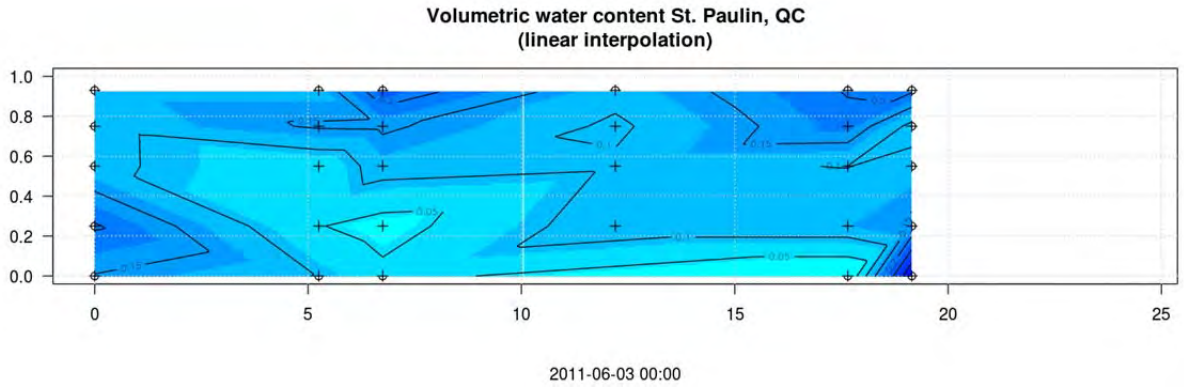

Figure 25. Linear interpolation of the soil moisture content on the starting date of scenario a (03/06/2011). This interpolation was used as initial condition for the three subdomains (from left to right: *Populus spp.* between x=0-6 m, forage between x=6-18.4 m and *Quercus rubra* between 18.4-24.4 m).

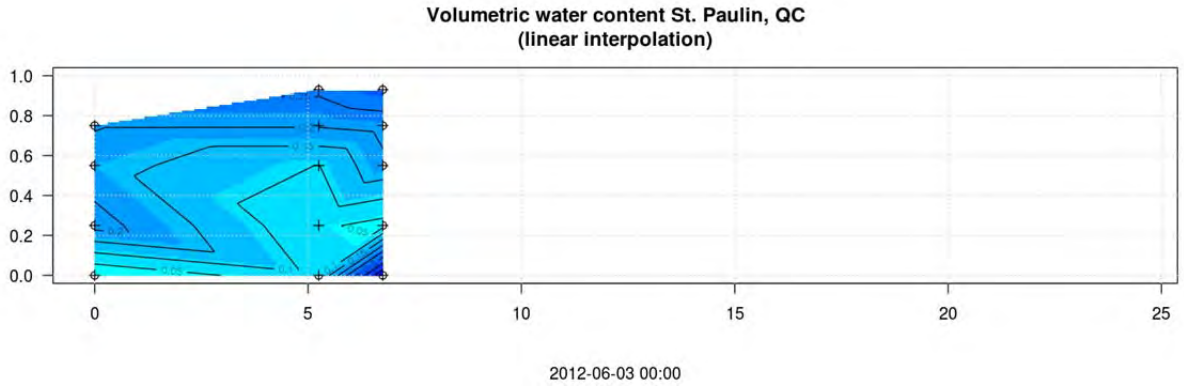

Figure 26. Linear interpolation of the soil moisture content on the starting date of scenario b (03/06/2012). This interpolation was used as initial condition for the subdomain of *Populus spp.*

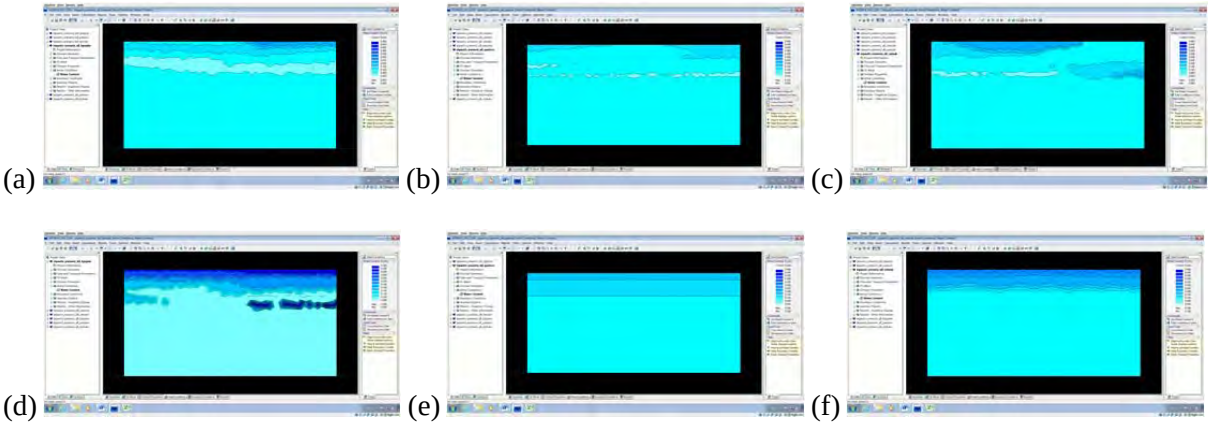

Figure 27. HYDRUS initial conditions for 2011 (a,b,c) and 2012 (d,e,f).

4.2.2.5 Time-dependent model input

Precipitation and other weather variables were provided for every 15 minutes, and in order to synchronize these data with FDR data we reinterpolated them for the whole hour, 15 minutes past the hour, 30 minutes past the hour and 45 past the hour. The total of interpolated precipitation intensities calculated for HYDRUS was compared to the total of the original data record to verify that the water balance was maintained. We further assumed that evapotranspiration was entirely for the account of transpiration by the plant canopy, and calculated a time-dependent potential transpiration rate with the Penman-Monteith equation (Allen *et al.*, 1998). A minimum pressure of -10,000 cm was allowed at the surface, and half the width of the subdomains for *Populus spp.* and *Quercus rubra* were associated with transpiration, *i.e.* 300 cm, while the entire width of the subdomain for forage was associated with transpiration (640 cm).

4.2.3 Hydrological simulations with HYDRUS for 2041-2070

After having obtained the climate variables for St. Paulin for 2041- 2070, and after parameterization of HYDRUS on 2011-2012 data, we simulated the soil water dynamics for the summer and autumn season of 2041 and 2070 at daily time steps. Again we used the transect of the experimental alley cropping system and the three subdomains corresponding with *Populus spp*. (hybrid poplar), *Quercus rubra* (red oak) and the intercrop (forage). The following scenario was defined:

- Scenario c: Climate change scenario for 2041-2070. Gives an indication of how alley cropping systems influence water availability to vegetation in the long term.

The parameter values used for each subdomain were found after parameterization of the model on 2011-2012 data and the initial moisture conditions on 03/06 of each year between 2041-2070 were based on the 2011 FDR data. The behavior of the system was analyzed based on differences in water availability and frequency of periods with a critical water content compared to 2011-2012 and the reference period 1967-1996.

Model performance was evaluated by comparing simulated water content below the vegetation with the water content measured with FDR. We subsequently analyzed the percentage of time that water was available for plants and the duration and frequency of periods with critical water conditions, defined as the state in which the daily average soil moisture content falls below the wilting point (pF>4 or pressure head < -10,000 cm) or exceeds the field capacity (pF<2 or pressure head >-10 cm).

4.2.4 Calibration of MHYDAS-Erosion

The model was calibrated using simulated values and initial parameters defined for each rainfall-runoff event observed during the field campaign (summer 2012). The model is thus theoretically capable of simulating the hydrological and erosion-transport processes for rainfall events with initial conditions similar to those covered during the field campaign. This section describes the calibration parameters and metrics used to calibrate the erosion model.

4.2.4.1 Calibration parameters

Because sediment transport is directly dependent on the micro-catchment hydrology, the calibration process is separated into a hydrological calibration and sedimentological calibration. The model is calibrated by adjusting the most sensitive input parameters, and constants in the equations that govern infiltration and surface flow. By comparing the simulated flow rates and sediment fluxes with recorded data, the user can change the calibration parameters, whilst realistic values. Section 3.2.3 describes some of the initial condition parameters and associated values found by Gumiere *et al.* (2010) during MHYDAS-erosion calibration for another watershed.

MHYDAS-Erosion solves equations related to the infiltration and transport analytically at each time step with methods developed by Morel-Seytoux (1984) and Hayami (1951), respectively. It is therefore possible to also adjust the model by changing the constants in the water infiltration and surface diffusivity equations (both for water and transported sediments).

4.2.4.2 Evaluation metrics

As recommended by Gumiere *et al*., 2011 evaluation statistics used include the Nash-Sutcliffe coefficient (ENS), the mean squared error (RMSE), the coefficient of determination (R^2), the relative volume error (RVE) and the percentage error at peak (PEP). These performance criteria were selected because they reflect different model properties (Dawson *et al.*, 2007) calculated as functions of time for each tested rainfall event**.** Table 14 shows the evaluation statistics and their respective ranges; where Y_i is the observed value $\hat{Y}_i$ simulated value, n is the number of elements in the sample and $\bar{Y}$ the average observed value.

Table 14. Metrics used to evaluate the performance of simulations with MHYDAS-Erosion.

Criteria	Equation	Range
E_{NS}	$E_{NS} = \frac{\sum_{i=1}^{n}(Y_i \times \hat{Y}_i)^2}{\sum_{i=1}^{n}(Y_i \times \overline{Y})^2}$	$[\times\infty, 1]$
RMSE	$\mathrm{RMSE} = \sqrt{\frac{1}{n}\sum_{i=1}^{n}(Y_i \times \hat{Y}_i)^2}$	$[0, +\infty]$
R^2	$R^2 = \left[\frac{\sum_{i=1}^{n}(Y_i \times \overline{Y})(\hat{Y}_i \times \tilde{Y}_i)}{\sqrt{\sum_{i=1}^{n}(Y_i \times \overline{Y})^2 \sum_{i=1}^{n}(\hat{Y}_i \times \tilde{Y}_i)^2}}\right]^2$	$[0, 1]$
RVE	$\mathrm{RVE} = \frac{\sum_{i=1}^{n}(Y_i \times \hat{Y}_i)}{\sum_{i=1}^{n} Y_i}$	$[\times\infty, +\infty]$
PEP	$\mathrm{PEP} = \frac{\max(Y_i) \times \max(\hat{Y}_i)}{\max(Y_i)} \cdot 100$	$[\times\infty, +\infty]$

4.2.4.3 Hydrograph separation

MHYDAS-Erosion only simulates Hortonian runoff caused by the portion of rainfall that is not directly infiltrated. Flow rates simulated by the model are only product of surface runoff. A hydrograph separation for each recorded event is thus needed to determine their surface flow components. The linear separation method is chosen for this study. Although this method tends to underestimate the base flow during stormflow, this method is chosen because of its simplicity and constant values.

4.2.5 Simulation of water erosion with MHYDAS-Erosion

4.2.5.1 Erosion scenarios

One of the objectives of this study is to evaluate the trapping efficiency of strategically placed tree strips. Two simulation scenarios are tested using the parameters found after model calibration, using initial parameters from the event that yielded the highest sediment export. The calibration event most likely to yield the most erosion is chosen according to the amount of ploughed or bare fields, the stage of plant growth, the normalised antecedent precipitation index (NAPI) and the importance of the rainfall event in terms of maximum intensity and total precipitation. Each scenario is then tested by running the simulations with synthetic storm events with different return periods and different distributions (triangular, SCS, Chicago, etc.). Different distributions of varying intensities allow the watershed to be tested under different types of stresses (volume vs. peak intensity). Section 4.2.5.2 discusses in more detail the return periods and distributions used. The simulation scenarios are defined as follows:

- Bras d'Henri micro-watershed under current field conditions.

- Bras d'Henri micro-watershed with strategically placed rows of trees (hypothetical scenario). This scenario assumes that tree rows are planted along the downstream edge of all SUs.

As discussed in section 3.2.2, SU-SU and SU-RS topological links are derived from specific hydrological path calculated using PHYSITEL (shown in Figure 5). The hypothetical scenario assumes that each topological connection contains a vegetative strip (in this case tree strips) capable of trapping sediments. Each strip is at the intersection between two SUs within the same field, between two different fields or between fields and their corresponding RS. Figure 28 shows the same topology diagram as shown in Figure 5, but showing tree strip locations for the hypothetical scenario (seen as green stripes).

Sediment abatement induced by tree strips is derived from equations provided by Deletic (2001) and Deletic and Fletcher (2006). MHYDAS-erosion vegetative filter module is used, taking as input strip width and density (respectively *Strip.width* and *Strip.density* found in Table 1, in section 3.2.3.1). The average tree strip width set to 5 m and average density to 0.65.

Figure 28: Tree strip locations according to topology for the hypothetical scenario.

4.2.5.2 Synthetic rainfall and erosion simulation

Both scenarios must be tested with synthetic rainfall because, as will be shown in the results, no calibration events contained rainfall intensities large enough to generate significant field erosion. To better represent the tree strip trapping efficiency in the hypothetical scenario, a variety of synthetic design rainfalls for return periods of 10, 50 and 100 years are chosen to form a total of 18 simulations. The total precipitation for each return period is found with the intensity-duration-frequency (IDF) curves provided by Environment Canada for the city of Lévis, which is the closest location for which these curves are available.

We selected a 24 hour triangular distribution because it is most representative of rainfall events observed in the province of Quebec (Pelletier *et al.* 2009). The 6 hour and 24 hours Chicago rainfall distributions were chosen because they have a very high peak flow resulting in potentially high erosion rates. Although these distributions are still conservative in terms of intensity, their common use in hydraulic design allows the micro-catchment to be studied under high hydrologic stress within well-known conditions. Table 15 shows the distributions and total precipitation based on their return period.

Table 15. Distribution and total precipitation for synthetic rainfall according to return period.

SIMULATION	Precipitation (mm)
Chicago 6h	
10 years	55.6
50 years	71.4
100 years	78.1
Chicago 24h	
10 years	75.0
50 years	92.5
100 years	99.9
Triangulaire 24h	
10 years	75.0
50 years	92.5
100 years	99.9

5 Results

5.1 Observed soil moisture patterns in 2011-2012

The combination of continuous weather observations and continuous soil moisture at different depths allowed us to better understand the relationship between the two. By plotting soil water-timegraphs and soil water profiles we were able to identify the principal hydrological processes that characterize the alley cropping system. The figure below shows a typical summer rainfall distribution of a 71-mm event recorded in August 2011, and the corresponding evolution of the volumetric water content of the soil at a distance of 75 cm from *Quercus rubra* (red oak) in the 24 hours that followed the onset of rainfall. The response can be divided into three stages: (1) infiltration upon first rainfall, and wetting from the bottom upwards during the first hour and a half; (2) saturation of the bottom soil layers after 3 hours, during the second rainfall peak; and (3) drainage taking over as the dominant hydrological process after 4 hours. A trend observed for many events shows a rapid response of the lower soil layers (below a depth of 50 cm) at a horizontal distance of 75 cm from *Quercus rubra*, whereas the topsoil (above a depth of 25 cm) responds more quickly directly below the tree.

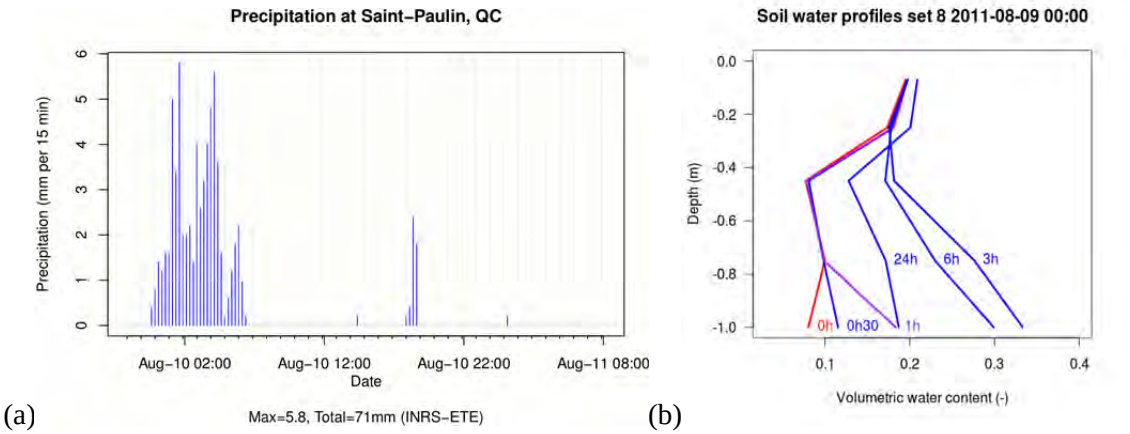

Figure 29. A typical summer rainfall recorded in St. Paulin on August 10, 2011 (a), and the corresponding soil water response over the course of 24 hours (b).

We subsequently performed a spatial interpolation of the 15-minute FDR point data in order to generate a spatial image of the soil moisture distribution and evolution during the 2011 and 2012 seasons. The interpolated soil moisture map fills in the gaps in the data and we can now observe more clearly that preferential flow is a plausible cause of the rapid infiltration. Water flowing along the stem saturated the soil around the tree (denoted 1 in the subfigure b), and quickly found its way down through nearby macropores (2 and 3) by means of preferential flow. Although not shown here, the observed data indicated different soil moisture patterns in the alley where the soil water dynamics mostly occurred in the first 45 cm of the soil. These results suggest that each vegetation system has a significant impact on soil water movement.

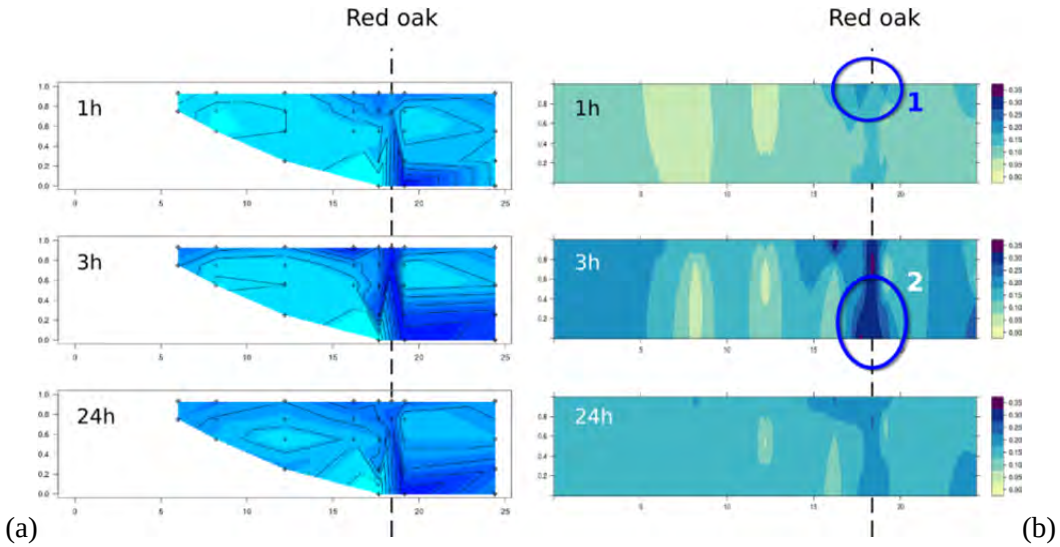

Figure 30. Linear (a) and Kriging interpolation (b) of volumetric water content to a depth of 100 cm below *Quercus rubra* (red oak). The interpolated period is August 10, 2011 and shows rapid infiltration from point (1) to point (2), directly below the tree.

5.2 Local climate simulation for 2041-2070

5.2.1 Distributions of daily P, Tmax and Tmin at St. Paulin

The 2011 and 2012 distributions of daily P, Tmax and Tmin at St. Paulin (elevation 140 m) are skewed, in part because these data do not cover the entire year. Atmospheric data are distinctly asymmetric and skewed toward extreme values, and in these cases it is generally not considered useful to fit a normal distribution (Wilks, 2006).

Daily precipitation, which has a physical constraint in that it cannot be negative, can be characterized by a combination of a discrete function at P=0 and a continuous gamma distribution for P>0 (e.g. Kedem, 1990; Cho *et al.*, 2004). The figure below shows the histogram of 2012 daily precipitation at St. Paulin, for which we fitted a gamma probability distribution with alpha=0.611 and beta=0.0864 to precipitation values of P>0. The quantile-quantile plot, cumulative distribution functions and probability-probability plots show that the gamma distribution fits quite well to the data.

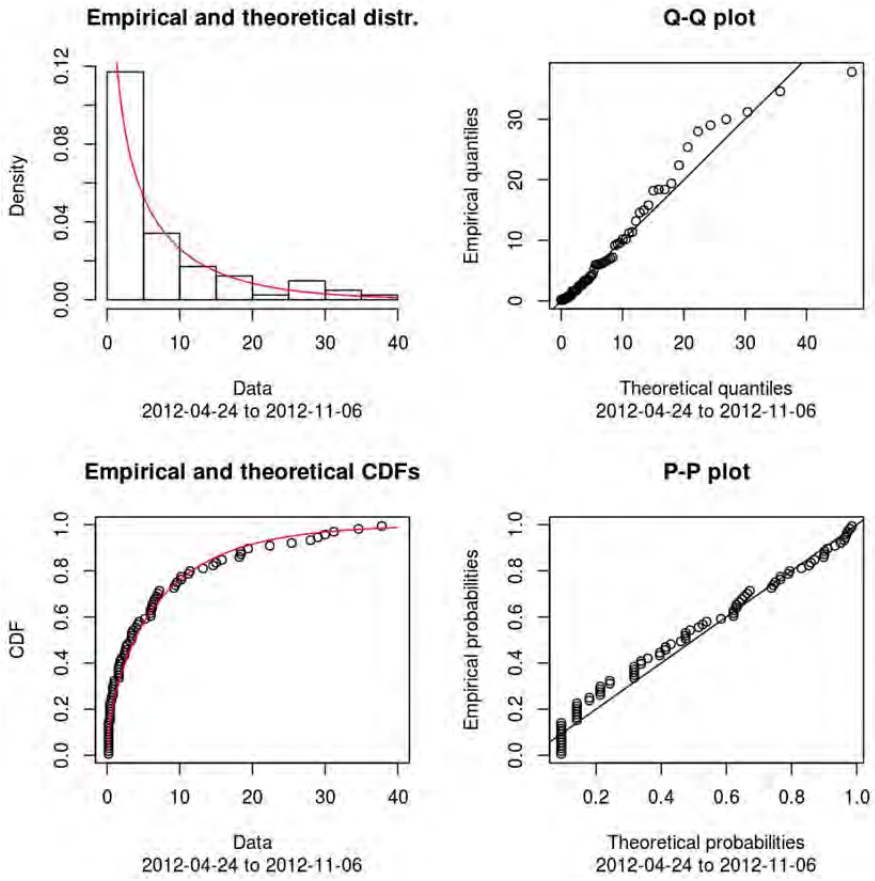

Figure 31. Distribution of 2012 daily precipitation at St. Paulin: (a) histogram and gamma probability density function with alpha=0.61 and beta=0.08 fitted for P>0; (b) the quantile-quantile plot; (c) cumulative distribution functions; and (d) probability-probability plots.

For the 2012 daily Tmax and Tmin we can also fit a gamma probabily distribution, with alpha=1593 and beta=5.41, and alpha=2320 and beta=8.26, respectively. The quantile-quantile plot, cumulative distribution functions and probability-probability plots show that the fits for the Tmax and Tmin probability density functions are even better than for daily precipitation. The probability distributions obtained for 2011 closely resemble 2012, but are not shown here for the sake of brevity. The table below gives the fitted parameters for Ptot, Tmax and Tmin of the St. Paulin dataset.

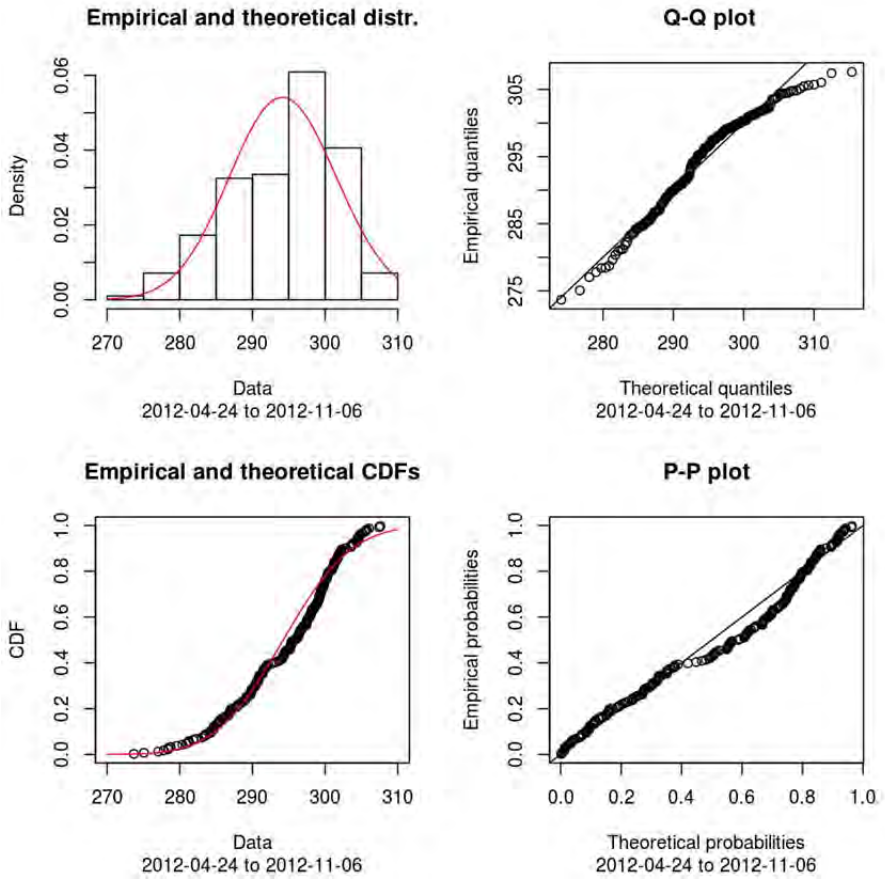

Figure 32. Distribution of 2012 daily Tmax at St. Paulin: (a) histogram and gamma probability density function with alpha=1593 and beta=5.41 fitted for P>0; (b) the quantile-quantile plot; (c) cumulative distribution functions; and (d) probability-probability plots. Note that temperature was converted to Kelvin in order to avoid negative values to which no gamma distribution can be fitted.

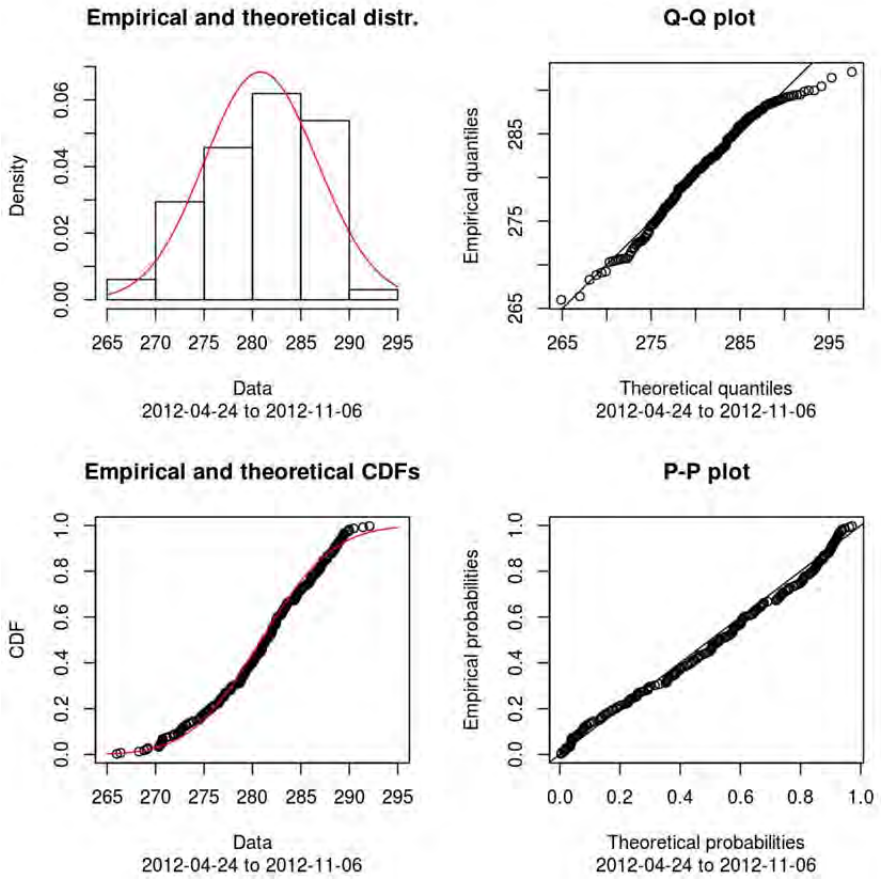

Figure 33. Distribution of 2012 daily Tmin at St. Paulin: (a) histogram and gamma probability density function with alpha=2320 and beta=8.26 fitted for P>0; (b) the quantile-quantile plot; (c) cumulative distribution functions; and (d) probability-probability plots. Note that temperature was converted to Kelvin in order to avoid negative values to which no gamma distribution can be fitted.

Table 16. Values of the alpha (shape) and beta (rate) parameters of the gamma distributions fitted to Ptot, Tmax and Tmin observed at St. Paulin in 2011-2012.

	Ptot		Tmax		Tmin	
	2011	*2012*	*2011*	*2012*	*2011*	*2012*
Alpha	0.547	0.611	1880.3	1592.9	2337.2	2320.3
Beta	0.0586	0.0864	6.39	5.41	8.30	8.26

5.2.2 Linear regression of Shawinigan and St. Paulin weather data

The linear regression of cumulative precipitation, Tmax and Tmin for Shawinigan and St. Paulin yielded a very strong correlation (R^2>0.95) for all three variables between 01/06/2011 and 10/11/2011, and 24/04/2012 and 06/11/2012. The figures below show the regression plots with the corresponding linear models for 2011, 2012 and for a concatenated dataset with 2011 and 2012 weather data. Cumulative precipitation at Shawinigan was slightly less (619 mm) than at St. Paulin (672 mm) in 2011, yielding a positive regression coefficient, whereas in 2012 the situation was reversed: 580 mm at St. Paulin versus 643 mm at Shawinigan, yielding a negative regression coefficient.

We observe that differences in Tmax and Tmin between both locations are mainly characterized by the intercept of the regression models, of which the value indicates that Tmax is generally lower (around 0.5°C) and Tmin generally higher (nearly 2°C) at Shawinigan. This may be explained by the fact that daily variations in temperature measured by the Shawinigan station were attentuated by the proximity of built-up area and the St. Maurice River. The effect is most pronounced during the night, when the air cools down less than at the St. Paulin experimental site, which is located in remote area.

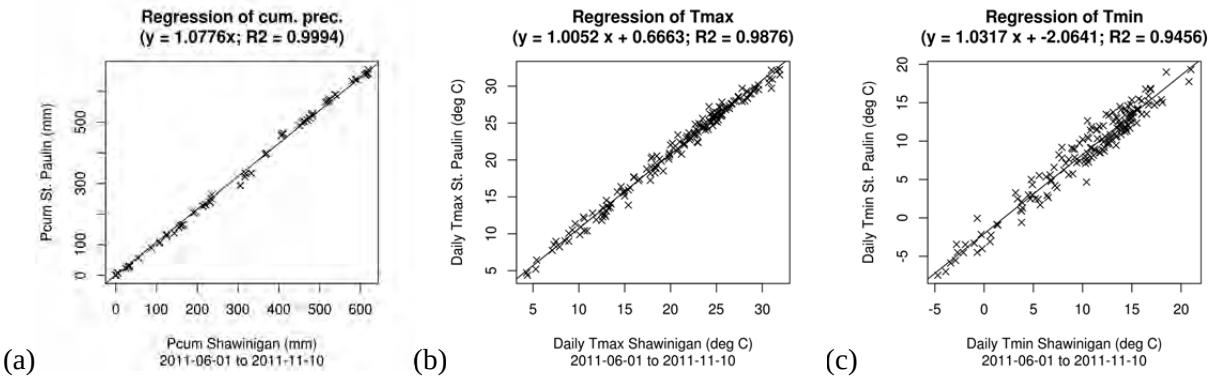

Figure 34. Linear regression of cumulative precipitation (a), Tmax (b) and Tmin (c) observed at Shawinigan (24 km NE of the experimental site) and St. Paulin in 2011.

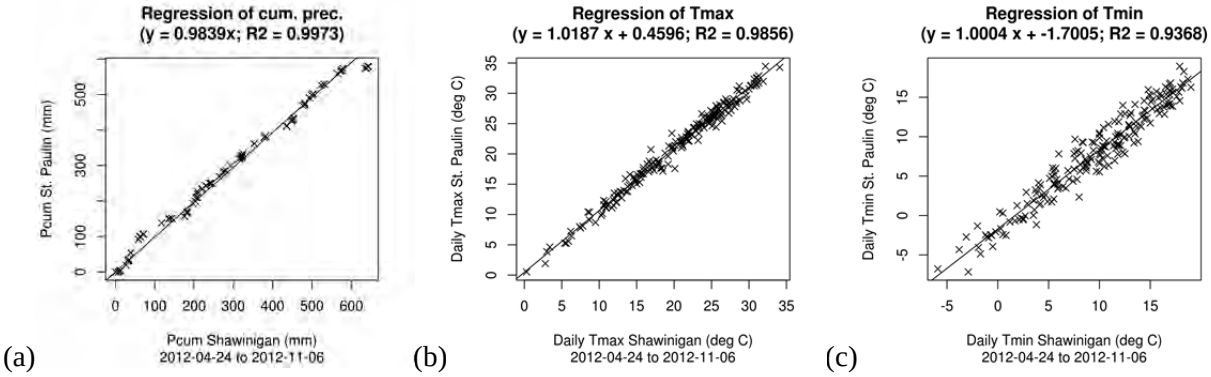

Figure 35. Linear regression of cumulative precipitation (a), Tmax (b) and Tmin (c) observed at Shawinigan (24 km NE of the experimental site) and St. Paulin in 2012.

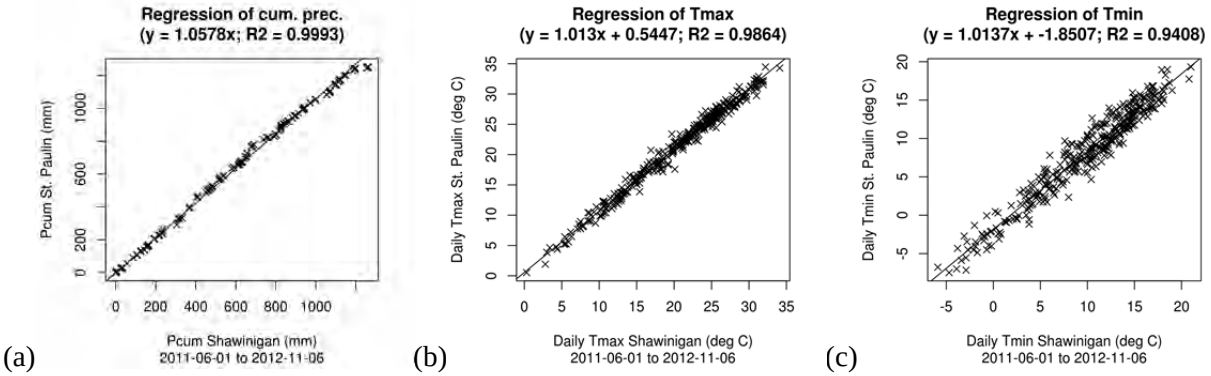

Figure 36. Linear regression of cumulative precipitation (a), Tmax (b) and Tmin (c) observed at Shawinigan (31 km WSW of the experimental site) and St. Paulin for the concatenated period 2011-06-01 to 2011-11-10 and 2012-04-24 to 2012-11-06.

5.2.3 Linear regression of St. Charles de Mandeville and St. Paulin weather data

The linear regression of St. Charles de Mandeville and St. Paulin weather data for 2011-2012 also yielded high coefficients of determination (R^2>0.94), indicating a linear relationship between cumulative precipitation, Tmax and Tmin for both locations between 01/06/2011 and 10/11/2011, and 24/04/2012 and 06/11/2012 (see figure on next page). Cumulative precipitation was in 2011 equal to 576 mm at St. Charles de Mandeville, which is less than the 672 mm measured at St. Paulin. The next year the situation was reversed: 645 mm at St. Charles de Mandeville versus 580 mm at St. Paulin.

Here too, we observe that differences in Tmax and Tmin between both locations are mainly characterized by the intercept of the regression models, of which the value indicates that Tmax is generally lower and Tmin generally higher at St. Charles de Mandeville. This time however, we suspect that this effect can be attributed to the lakes around the village of St. Charles de Mandeville.

5.2.4 Linear regression of Quebec City airport and St. Paulin weather data

Linear regression of Quebec City airport and St. Paulin weather data yielded resulted in high R^2, (>0.9) but still lower than for Shawiginan and St. Charles de Mandeville data (see figure on next page). Total precipitation in 2011 was 700 mm at Quebec City airport versus 672 mm at St. Paulin, and in 2012 total precipitation was 576 mm at Quebec City airport versus 580 mm at St. Paulin, which is highly similar despite the 135 km between both weather stations. This is also reflected in the coefficient of determination for cumulative precipitation: 0.9977 in 2011 and 0.9879 in 2012. Again, Tmax is generally lower and Tmin generally higher at Quebec City airport. This may be explained by its proximity to the St. Lawrence River.

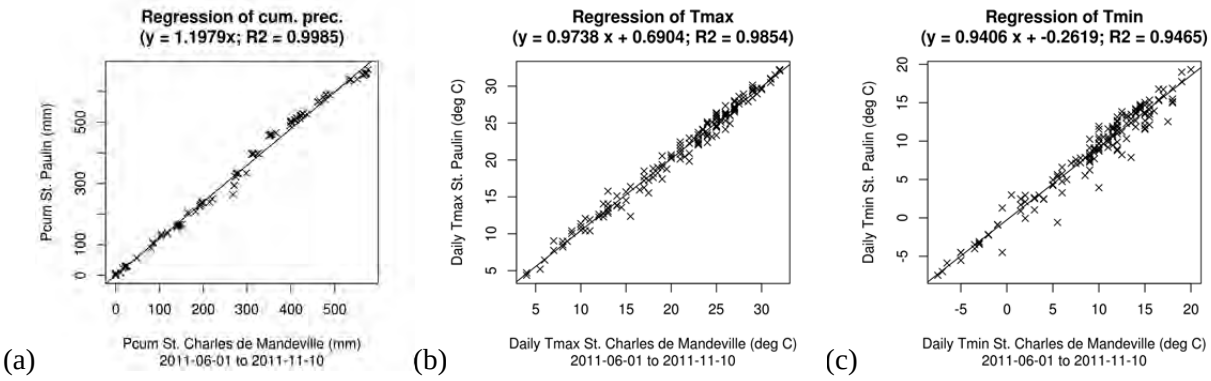

Figure 37. Linear regression of cumulative precipitation (a), Tmax (b) and Tmin (c) observed at St. Charles de Mandeville (31 km WSW of the experimental site) and St. Paulin in 2011.

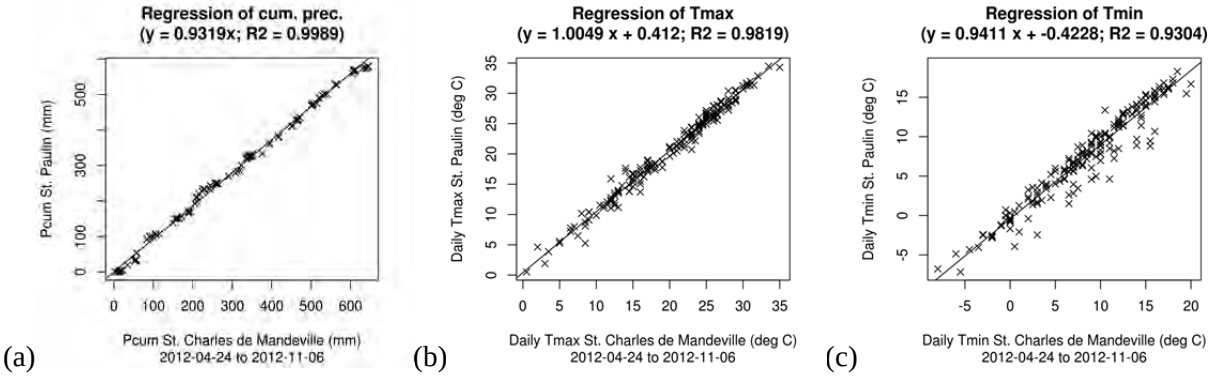

Figure 38. Linear regression of cumulative precipitation (a), Tmax (b) and Tmin (c) observed at St. Charles de Mandeville (31 km WSW of the experimental site) and St. Paulin in 2012.

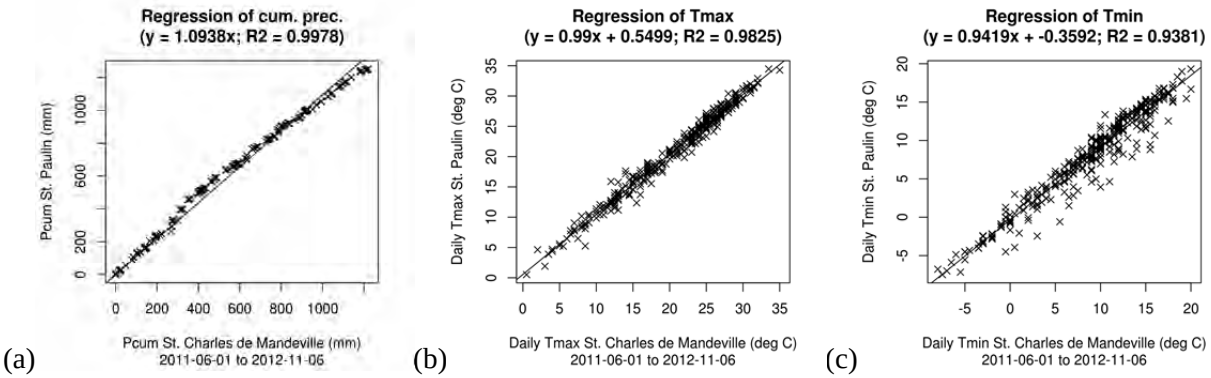

Figure 39. Linear regression of cumulative precipitation (a), Tmax (b) and Tmin (c) observed at St. Charles de Mandeville (31 km WSW of the experimental site) and St. Paulin for the concatenated period 2011-06-01 to 2011-11-10 and 2012-04-24 to 2012-11-06.

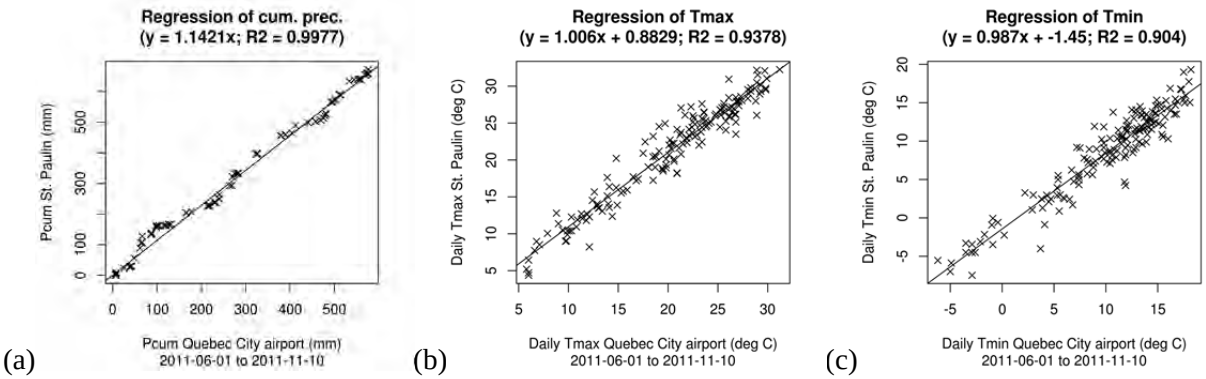

(a) (b) (c)

Figure 40. Linear regression cumulative precipitation (a), Tmax (b) and Tmin (c) observed at Quebec City airport (135 km ENE of the experimental site) and St. Paulin in 2011.

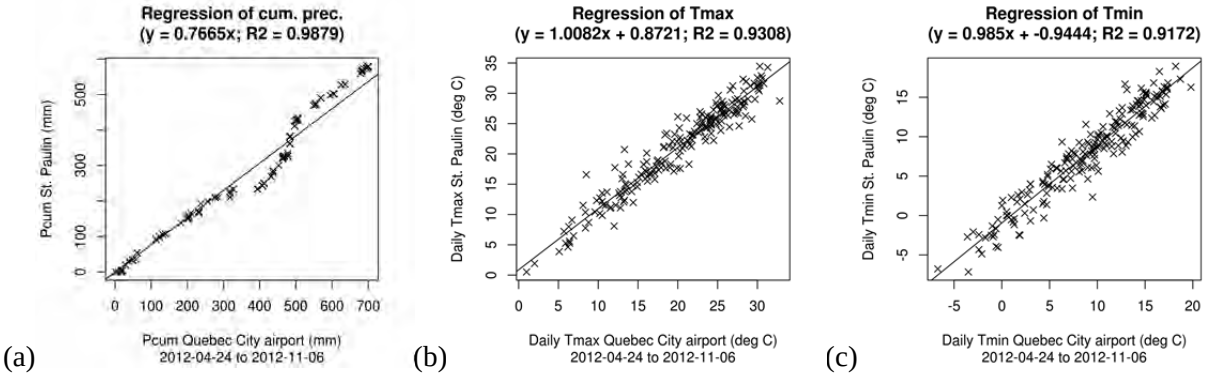

(a) (b) (c)

Figure 41. Linear regression of cumulative precipitation (a), Tmax (b) and Tmin (c) observed at Quebec City airport (135 km ENE of the experimental site) and St. Paulin in 2012.

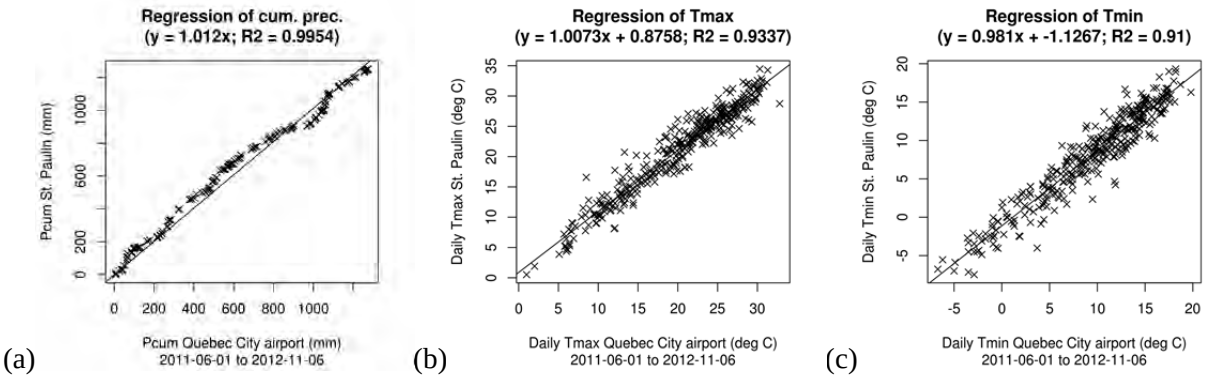

(a) (b) (c)

Figure 42. Linear regression of cumulative precipitation (a), Tmax (b) and Tmin (c) observed at Quebec City airport (135 km ENE of the experimental site) and St. Paulin for the concatenated period 2011-06-01 to 2011-11-10 and 2012-04-24 to 2012-11-06.

5.2.5 Reconstruction of a reference dataset for 1967-1996 (linear regression)

Given the high values for R^2 found for the 2011-2012 linear models of daily P, Tmax and Tmin obtained at Shawinigan, St. Charles de Mandeville and Quebec City airport, with respect to St. Paulin data, we concluded that data from these locations can be used to reconstruct a 30-year reference dataset for St. Paulin. The 30-year reference dataset for 1967-1996 was mostly based on Shawinigan data, because the corresponding linear regression model yielded the greatest coefficient of determination, and where data were missing we completed with data from St. Charles de Mandeville. If no data for either of these two stations, we used the Quebec City airport data (30-year statistics provided in table below).

Table 17. Simulated 30-year statistics of daily precipitation, Tmax and Tmin for St. Paulin in 1967-1996. Values were estimated based on observation at Shawinigan, St. Charles de Mandeville and Quebec City airport.

	Precipitation (P)	Maximum temperature (Tmax)	Minimum temperature (Tmin)
Minimum	0	-27.8 (17/01/1982)	-49.5 (18/01/1982)
1st Quartile	0	0.5	-10.9
Median	0	11.2	-0.7
Mean	3.0	10.4	-2.2
3rd Quartile	2.6	21.4	8.3
Maximum	100.5 (22/06/1981)	36.0 (01/08/1975)	21.3 (21/07/1977)

5.2.6 Simulation of the local climate in 2041-2070 (constant scaling)

We applied the constant scaling method (Mpelasoka and Chiew, 2009) to obtain simulations of daily precipitation, Tmax and Tmin for the period 2041-2070. The 30-year monthly deltas provided by Ouranos were applied to the 30-year reference dataset based on data from Shawinigan, St. Charles de Mandeville and Quebec City airport: the deltas for precipitation were provided as a factor, and therefore were multiplied with daily precipitation in 1967-1996, whereas the deltas for Tmax and Tmin were provided in centigrade, and therefore added or subtracted from the daily values in 1967-1996. Note that the Shawinigan dataset has a gap between 1997-1998, and therefore we did not use the same 1971-2000 reference period for which Ouranos carried out analyses.

5.3 Hydrological simulation of 2011-2012

5.3.1 Evaluation of model performance

In order to evaluate model performance we compared simulated and observed water content at a depth of 25 cm and directly below *Populus spp.* and at the same depth but 75 cm away from the tree (see figure below). These two locations were chosen because (1) soil water dynamics at this depth are most responsive to root uptake and evapotranspiration; and (2) the FDR sensors at these locations provide a continuous soil moisture dataset that covers the entire simulation period from 03/06 to 03/11.

The best agreement was obtained for 2011 (subfigure a), where the value of the initial condition was very close to the value measured by the FDR sensor. At the end of the 2011 simulation period the observations spread out and we see that outliers (water content >0.4) are not well reproduced by the model. In 2012 the initial water content is overestimated with respect to the observation. The reason for this is that because recorded values can vary from one sensor to another due to variations in the contact surface with the soil, the initial condition was not taken directly from observed values but interpolated linearly and averaged out. The seasonal evolution of soil moisture is nevertheless well reproduced for 2011, the soil being wetter at the end of the simulation period, and given that the offset at thebeginning of the 2012 simulation period is maintain until the end (0.09 vs. 0.11) we are very positive about the model performance. We were not able to evaluatie model performance for *Quercus rubra* and forage because of technical issues.

(a)

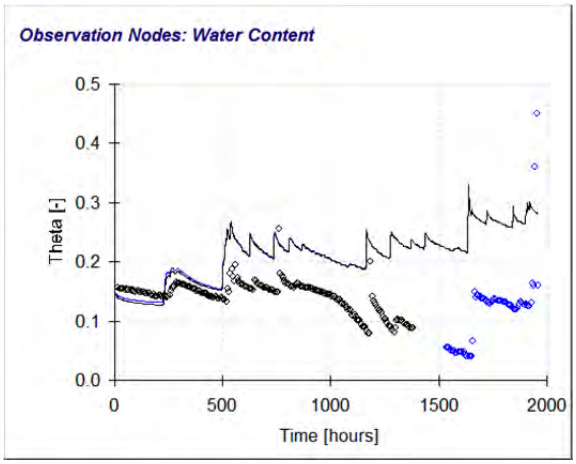

(b)

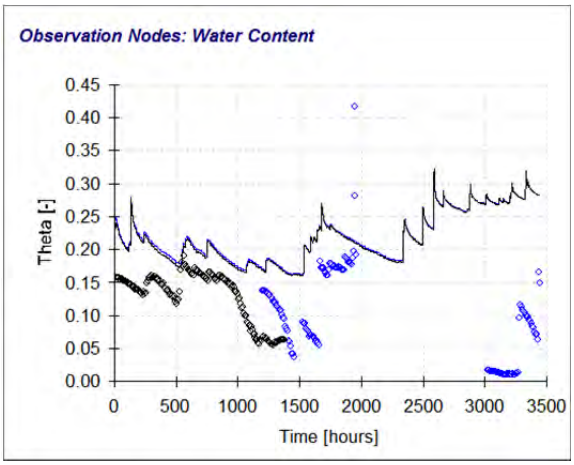

Figure 43. (a) Simulated (line graph) and observed water content (circles) between 03/06/2011 and 03/11/2011 at a depth of 25 cm, 75 cm away from *Populus spp.* (in black; x=5.25 m) and at a depth of 25 cm directly below *Populus spp.* (in blue; x=6.0 m); (b) likewise for the period between 03/06/2012 and 03/11/2012.

5.3.2 Water availability

Plants have a high adaptation capacity and are able to extract water available at pressure heads between the wilting point (pF=4 or a pressure head of -10,000 cm) and field capacity (pF=2 or a pressure head of -100 cm). The figure below shows the cumulative distributions of simulated pressure heads in 2011 and 2012 for the three vegetation types at a depth of 25 cm. We observe that the soil underneath the alley and *Quercus rubra* was too dry during nearly 10% of the period between 03/06/2011 and 03/11/2011 (b and c), whereas the water absorption capacity of *Populus spp*. allowed it to sustain an extractable pressure head around its root system at all times.

In 2012, the soil was wetter overall and available for plants during the entire summer and autumn, despite the fact that there was less rainfall: 580 mm in 2012 against 672 mm in 2011. The reason for this is that in the summer and autumn of 2011 the potential evapotranspiration was much higher than the amount of precipitation (PET of 634 mm vs 577 mm of precipitation), whereas the opposite was the case in 2012 (PET of 479 mm vs 525 mm of precipitation).

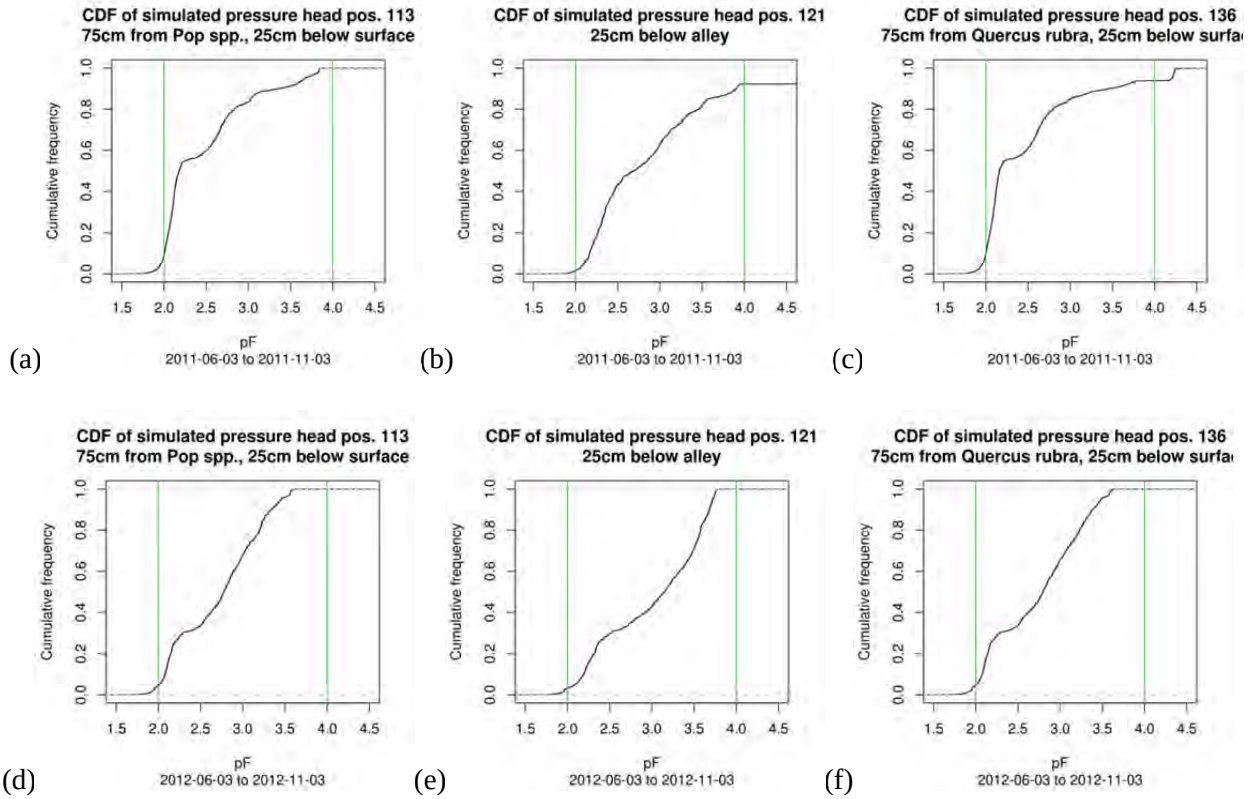

Figure 44. Cumulative distributions of simulated pressure head in the summer and autumn of 2011 (top) and 2012 (bottom) for *Populus spp*. (a), forage (b) and *Quercus rubra* (c). The green lines mark the field capacity (pF=2) and wilting point (pF=4) between which water is available for plant roots.

5.3.3 Duration and frequency of periods with critical water conditions

The figures below present the frequency of periods with waterlogging and the frequency of dry periods in 2011 and 2012 simulated for all three vegetation types. The model simulated two occurrences of waterlogging during three consecutive days below *Populus spp.* and *Quercus rubra*, and even one occurrence of four consecutive days of waterlogging between 17/07 and 21/07. For the alley vegetation we simulated a maximum of one consecutive day of waterlogging. As can also be deduced from the CDFs, no dry periods were simulated for *Populus spp.* in 2011, however the first ten days of the simulation period (between 03/06 and 13/06) were critically dry for the alley vegetation (pF=5.1) and *Quercus rubra* (pF=4.2).

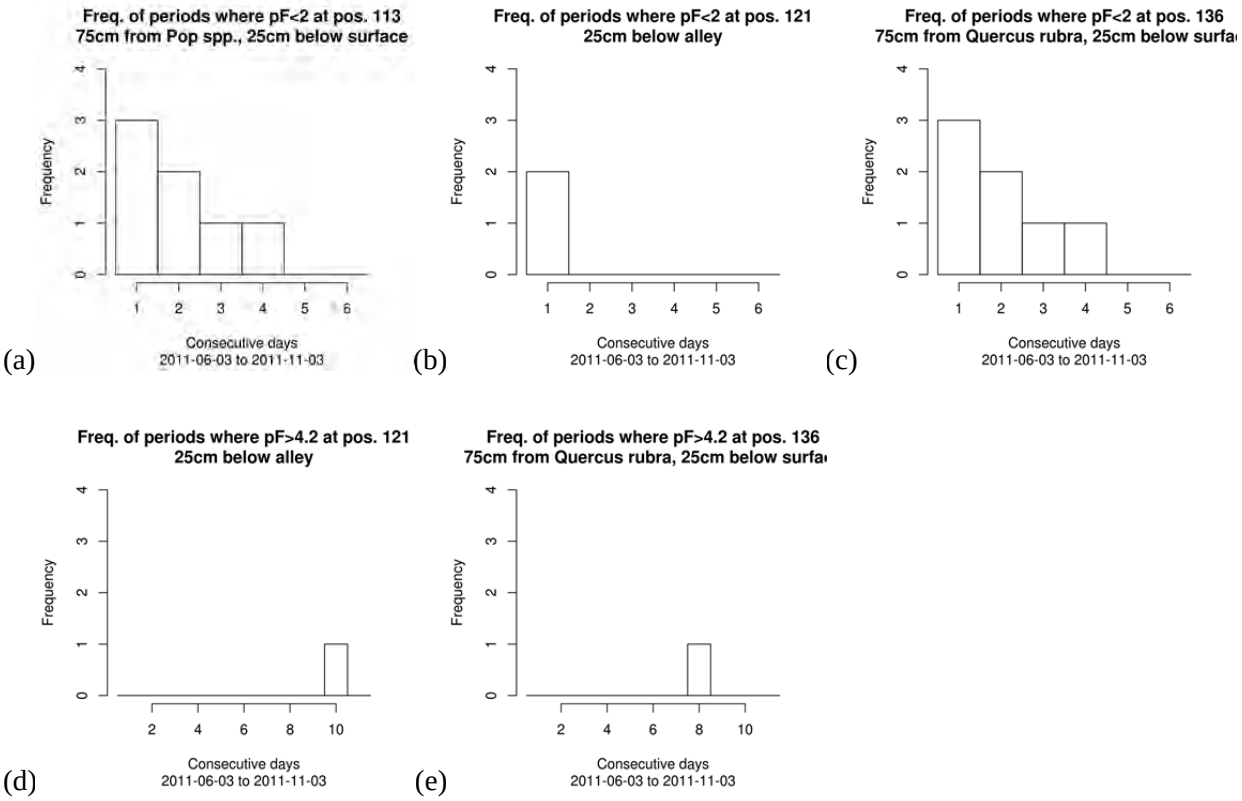

Figure 45. Frequency of periods with waterlogging simulated for the period between 03/06/2011 and 03/11/2011 for *Populus spp.* (a), forage (b) and *Quercus rubra* (c), and dry periods for forage and *Quercus spp.* (d and e, respectively). The frequencies were calculated based on daily average water content at the specified locations. No dry days (pF>4.2) were simulated for *Populus spp.*

As mentioned above the soil was in 2012 wetter than in 2011, which is also visible from subfigures d, e, and f in the figure below where only a single dry day is reported for *Populus spp.* The 24 days of waterlogging around the same vegetation were simulated after the first week of October 2012, following a very wet month of September (153.8 mm) and October (158.6 mm). Three weeks after waterlogging is first simulated for *Populus spp.*, the saturated area spreads to the alley and *Quercus rubra*.

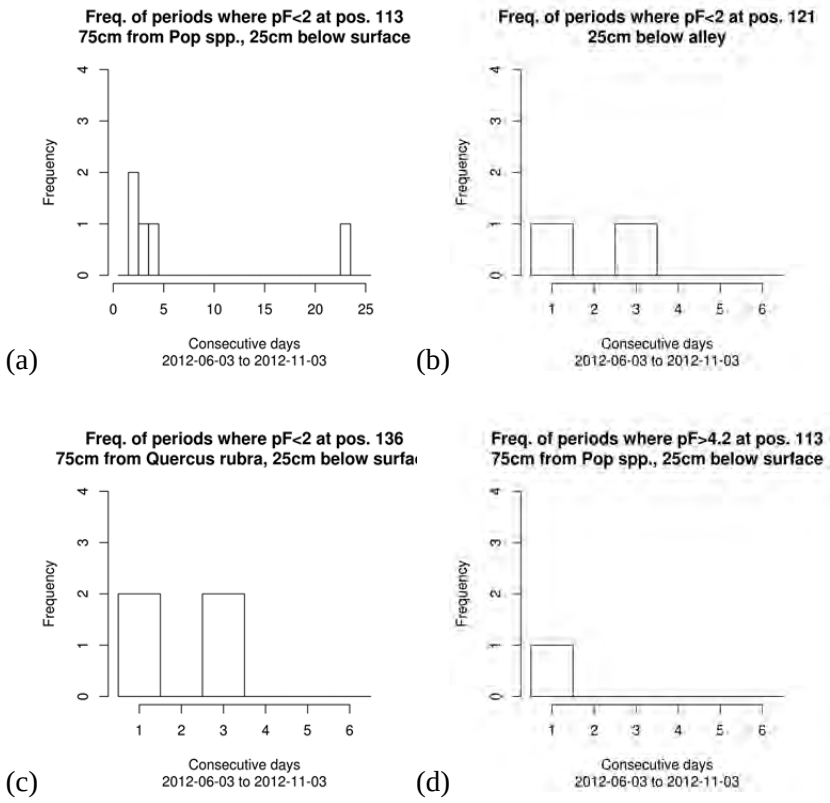

Figure 46. Frequency of periods with waterlogging simulated for the period between 03/06/2012 and 03/11/2012 for *Populus spp.* (a), forage (b) and *Quercus rubra* (c), and dry periods for *Populus spp.* (d). The frequencies were calculated based on daily average water content at the specified locations. No dry days (pF>4.2) were simulated for forage and *Quercus rubra*.

5.4 Hydrological simulation of 2041-2070

5.4.1 Water availability

The figures below show the cumulative distributions of simulated pressure head in the summer and autumn of 2041 and of 2071 at a depth of 25 cm for *Populus spp*. (a), forage (b) and *Quercus rubra* (c). The green lines mark the field capacity (pF=2) and wilting point (pF=4) between which water is available for plant roots. In the 2041 simulation, *Populus spp.* has access to water at all times as was the case in 2011 and 2012, whereas water availability increases considerably for forage (from 90% to 96% of the simulated period) and *Quercus rubra* (from 91% to 96%). This increased water availability cannot be ascribed to an increase in precipitation (635 mm during the summers and autumns of the simulated period 2041 against 637 mm in 2011), however it occurs simultaneously with an increase in transpiration: 610 mm during the summers and autumns of 2041 against 477 mm in 2011. The simulation suggests that in 2041, plant roots draw the water closer to the surface, which although not simulated explicitly could have a positive effect on water availability for alley crops.

For the summer and autumn of 2070 we see a different situation: water availability at a depth of 25 cm below the alley crops decreases to 86%, which is 4% lower than simulated for 2011 and 10% lower than simulated for 2041. However, *Populus spp.* has a nearly continuous water availability with a wetter profile compared to 2041, while *Quercus rubra* has access to water only 68% of the time with a drier profile than in 2041. We simulated 717 mm of precipitation, which is more than simulated for 2041, while transpiration is slighly lower at 595 mm. The great amount of precipitation adds more water to the soil, but this water percolates to deeper layers and cannot be retained in the topsoil due to the decrease in transpiration.

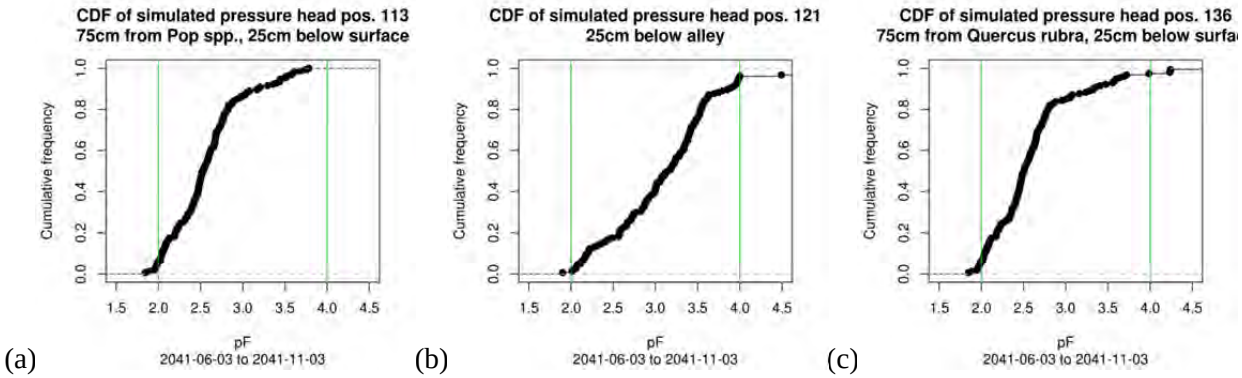

Figure 47. Cumulative distributions of simulated pressure head between 03/06 and 03/11 of the year 2041 for *Populus spp*. (a), forage (b) and *Quercus rubra* (c). The green lines mark the field capacity (pF=2) and wilting point (pF=4) between which water is available for plant roots. Statistics were computed for a depth of 25 cm.

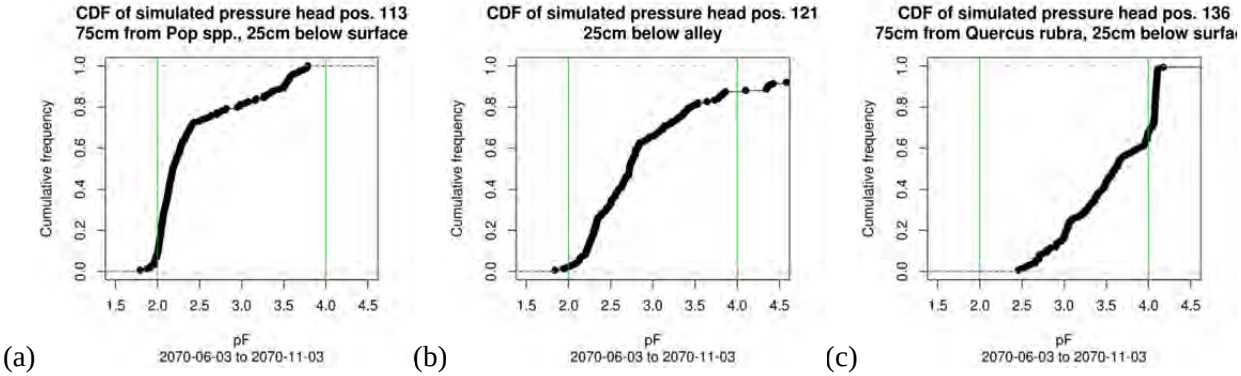

Figure 48. Cumulative distributions of simulated pressure head between 03/06 and 03/11 of the year 2071 for *Populus spp.* (a), forage (b) and *Quercus rubra* (c). The green lines mark the field capacity (pF=2) and wilting point (pF=4) between which water is available for plant roots. Statistics were computed for a depth of 25 cm.

A comparison of the cumulative distributions of simulated pressure head between 03/06 and 03/11 of the reference period 1967-1996 and of the future period 2041-2070 (represented in the figure below by black and blue line graphs, respectively) shows that changes in water availability over a 30-year period point toward a drier soil during most of the time. This effect is most pronounced within the normal pressure range of root uptake for *Populus spp.* and *Quercus rubra*, *i.e.* between pF=2 and pF=4, and is less apparent for forage. According to the simulations, water is available for 93%, 91% and 97% of the simulated 30 year period for *Populus spp.*, forage and *Quercus rubra*, respectively.

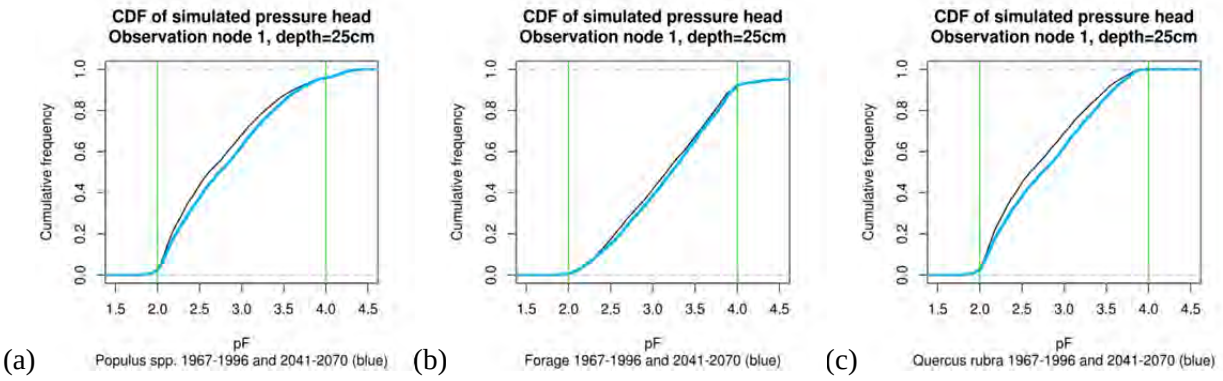

Figure 49. Cumulative distributions of simulated pressure head between 03/06 and 03/11 of the reference period 1967-1996 (in black) and of the future period 2041-2070 (in blue) for *Populus spp.* (a), forage (b) and *Quercus rubra* (c). The green lines mark the field capacity (pF=2) and wilting point (pF=4) between which water is available for plant roots. Statistics were computed for a depth of 25 cm.

5.4.2 Duration and frequency of periods with critical water conditions

In addition to the total duration of the period with optimum water availability, it is also of great importance to know the duration and frequency of periods with critical water conditions because this determines how likely a plant is able to survive under such conditions. The figure below shows how many periods with waterlogging between 03/06 and 03/11 were simulated for the reference period 1967-1996 (black bars) and for 2041-2070 (grey bars) in the HYDRUS subdomains corresponding to *Populus spp.* (a), forage (b) and *Quercus rubra* (c). Subfigures d and e show the dry periods for *Populus spp.* and forage, respectively. Note that no dry days (pF>4) were simulated for *Quercus rubra*.

In the reference period, waterlogged periods of one day were simulated 57 times for *Populus spp.*, 56 times for *Quercus rubra* and 16 times for forage (subfigures a, b and c). For 2041-2070 the one-day waterlogged periods occurred 10-11 times less below the trees (*Populus spp.* and *Quercus rubra*) with respect to the reference period. For forage on the other hand we observe that a two-day waterlogged period for the reference period becomes a one-day waterlogged period in the 2041-2070 simulation. The longest waterlogged period below *Quercus rubra* was 7 days, and occurred once in reference period (1993) and once in the future period (2067). 1993 was a wet year with 1198 mm of precipitation (*cf.* the local climate normal for 1967-1996 of 1104 mm). The 7-day waterlogged period was simulated for both the reference period and the future period in the same year of the respective climate sequences, *i.e.* the 27th year, which demonstrates that the correlation between the future climate scenario and the reference data is also reflected in the simulation of soil water dynamics.

While waterlogging during a maximum of one day is fairly common in the simulations, dry spells lasted much longer than periods of waterlogging (subfigures d and e). In addition, the dry spells simulated for 2041-2070 were longer than for 1967-1996. The longest dry spell of 29 days was simulated for forage within the period 2041-2070. Although the year of this dry spell was very wet (1684 mm, *cf.* the simulated climate normal for 2041-2070 of 1193 mm), the precipitation simulated for the month of August was very low with 30 mm (*cf.* the simulated monthly normal of 93 mm). Because of the shallow rooting depth of forage (up to 30 cm) and a maximum extraction rate equivalent to half that of *Populus*

spp. (0.1 mm/hr), soil water soon percolated to layers beyond the reach of forage roots resulting in prolonged water deficit in the soil and wilting of the forage vegetation. During the same period no critical dryness was simulated for *Populus spp.* and *Quercus rubra*, because these trees have a greater rooting depth (95 cm and 55 cm, respectively) and are able to continue extracting water during dry months, thus preventing the water from percolating out of the extraction zone.

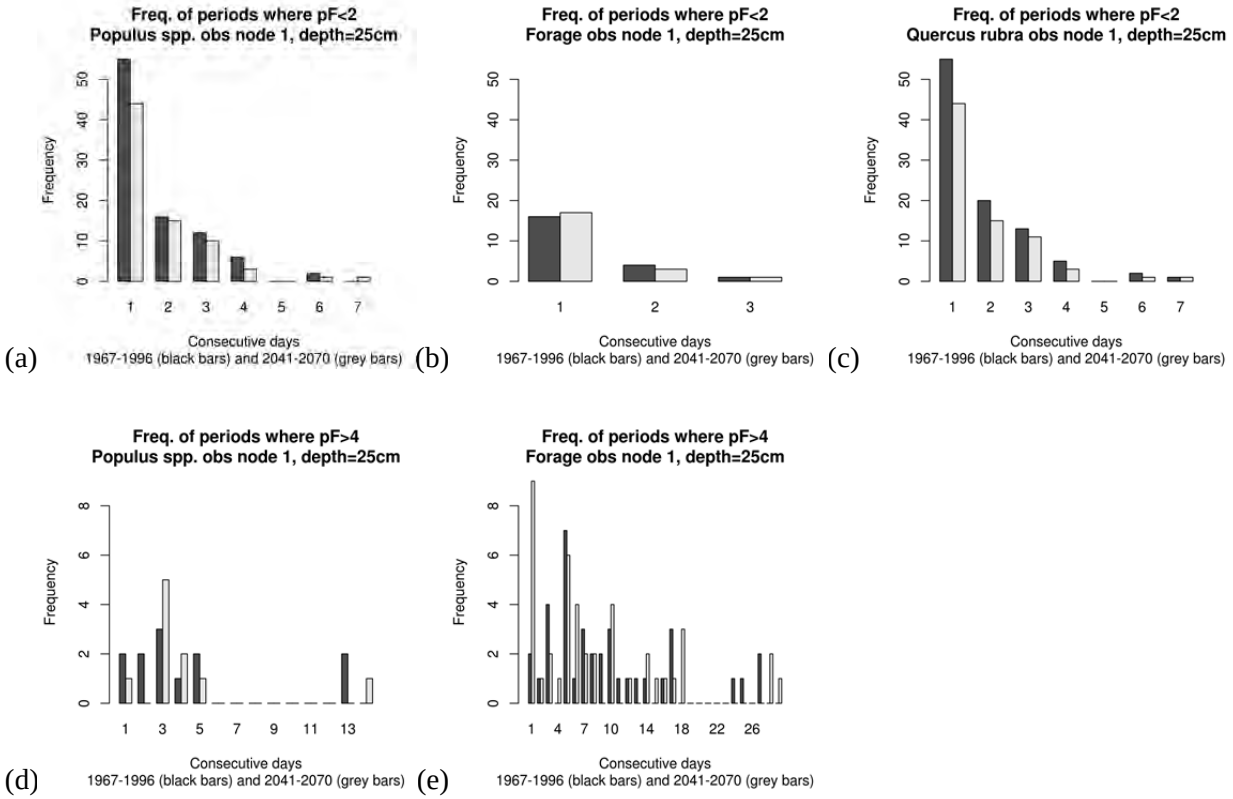

Figure 50. Frequency of periods with waterlogging simulated between 03/06 and 03/11 for the reference period 1967-1996 (black bars) and for 2041-2070 (grey bars) *Populus spp.* (a), forage (b) and *Quercus rubra* (c), and dry periods for *Populus spp.* (d) and forage (e). The frequencies were calculated based on daily average water content at the specified locations. No dry days (pF>4) were simulated for *Quercus rubra*. Statistics were computed for a depth of 25 cm.

5.5 Erosion simulations

5.5.1 Calibration of MHYDAS-Erosion

Table 18 shows the characteristics for each rainfall-runoff event recorded during the 2012 field campaign in the St-Narcisse-de-Beaurivage catchment. Summer events are more akin to convective events in their intensities, unlike autumn events. The 5th and 10th of August as well as the 19th of October events (in bold) are the most likely to produce erosion and transport, as they have the highest total precipitation and higher intensities. However, according to the NAPI, the 5th of August event occurred after a dry period, leaving the unsaturated soil more conducive and less prone to infiltration, minimizing runoff. In addition, both events in August occurred during the period of maximum crop cover, further reducing erosion in the field. For these reasons, the 19th of October event (underlined) is used for model calibration.

Table 18. Rainfall characteristics for the 2012 events used in the calibration of MHYDAS-Erosion.

Date	Duration (h)	Total precip. (mm)	Mean intensity (mm/h)	Max. intensity (mm/h)	NAPI 5	NAPI 2
2012 Jul. 04	8	14.4	1.81	11.9	0.69	-
2012 Aug. 05	**11**	**26.7**	**2.4**	**10.1**	**-**	**-**
2012 Aug. 10	**29**	**32.5**	**1.1**	**14.2**	**0.67**	**0.60**
2012 Sept. 08	10	12.2	1.2	7.8	0.78	-
2012 Sept. 18	14	16.0	1.1	6.9	-	-
2012 Oct. 06	15	24.1	1.6	4.6	0.75	0.61
2012 Oct. 14	22	13.2	0.6	2.3	0.79	0.61
2012 Oct. 19	**14**	**27.4**	**2.0**	**7.4**	**0.67**	**0.66**

The linear hydrograph separation (as described in **section 4.2.4.3**) is shown in Figure 51 **(a).** The model is only calibrated for hydrological processes, because no calibration events had precipitations intensities high enough to generate substantial erosion to be simulated by MHYDAS-erosion. Nevertheless, a comparison with the sediment fluxes on a comparable watershed located in Lennoxville for similar events confirms that the simulated results are of the right order of magnitude (Duchemin 2001). Further discussion on this validation is found in section **6.2.** Model calibration results for the 19th of October (hydrological processes only) are shown in Figure 51 **(b)**, and evaluation statistics are found in Table 19.

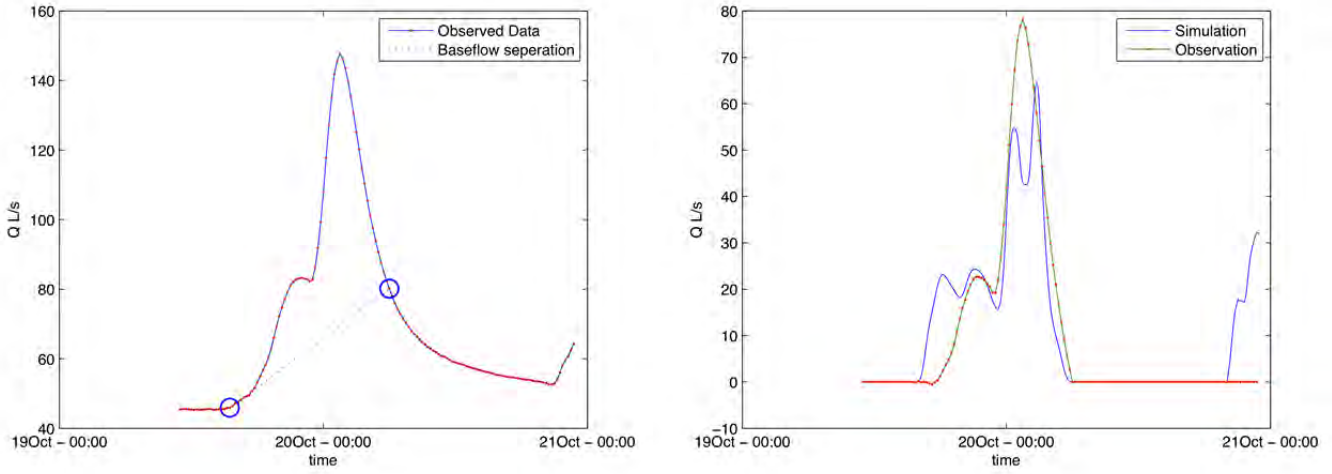

(a) (b)

Figure 51. a) Hydrograph separation and b) model hydrological calibration for the 19th of October 2012.

Table 19. Calibration metrics for the 19th of October 2012

Statistic	Value
RMSE	10.03
R^2	0.74
Nash_Sutcliffe efficiency (N_{CE})	0.74
Relative Volume Error (RVE)	9.75 $m^3 s^{-1}$
Percent error in the peak (PEP)	17.5%

5.5.2 Response to Chicago and triangular rainfall distributions

Table 20 gives the amount of soil loss simulated with MHYDAS-Erosion in response to Chicago and triangular rainfall distribution, and the abatement resulting from the use of vegetated filters to trap sediment. Simulation results show that for high intensity Chicago rainfall distributions, vegetated filters reduce total soil loss up to 20.8% for a return period of 10 years (6h), and 16.7 % for a return period of 100 years (24 hours). The low-intensity triangular rainfall distributions result in less erosion within the fields as the rainfall intensity develops more gradually over time, causing an apparent reduction in the trapping efficiency of vegetated filters with abatement values of 1.7% and 6.0% for return periods 10 and 100 years respectively. Figure 52 shows simulation results for the Chicago and triangular rainfall distributions where tree strips had the highest abatement efficiency. Note that the simulated sediment flux at the catchment outlet also includes sediment detached by means of bank erosion in the drainage network (see Discussion section).

Table 20. Soil loss simulated with MHYDAS-Erosion in response to Chicago and triangular rainfall distributions.

SIMULATION	Precipitation (mm)	Soil loss without strips (kg/ha)	soil loss with strips (kg/ha)	Δ m (kg/ha)	Δ m (%)
Chicago 6h					
10 years	55.6	34.6	27.4	7.2	20.8 %
50 years	71.4	61.8	49.8	12.0	19.4 %
100 years	78.1	75.3	61.8	13.5	17.9 %
Chicago 24h					
10 years	75.0	41.8	33.3	8.5	20.3 %
50 years	92.5	68.8	56.6	12.1	17.6 %
100 years	99.9	81.1	67.6	13.5	16.7 %
Triangulaire 24h					
10 years	75.0	14.5	14.3	0.2	1.68 %
50 years	92.5	41.6	40.8	0.8	2.01 %
100 years	99.9	58.8	55.3	3.5	6.03 %

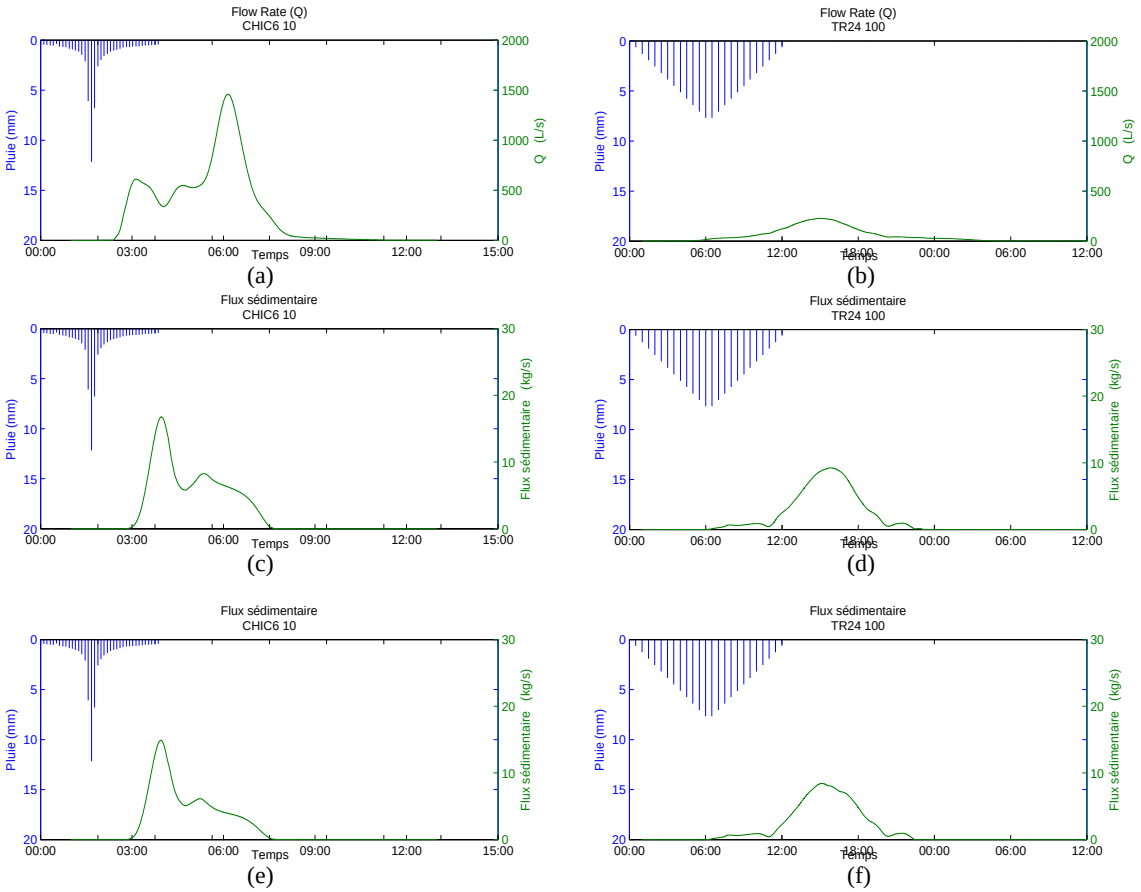

Figure 52. Simulated flow rate (a and b) and sediment flux at the catchment outlet in response to a 6h Chicago rainfall distribution with a 10 year return period (*right*) and 24 hour triangular distribution with a 100 year return period (*left*); without vegetated filter (c and d) and with vegetated filter (e and f).

6 Discussion

6.1 Influence of alley cropping on soil water dynamics in a changing climate

The comparison of soil water simulations for 2041-2070 with simulations for the reference period 1967-1996 suggests that given the local climate scenario for the experimental alley cropping site, the soil is drier and water availability to plants is reduced. Although the cumulative distribution of pressure head shows that the decrease in water content is greater for the trees (*Populus spp.* and *Quercus rubra*) than for forage growing within the alley, the analysis of periods with a pressure head below the wilting point suggests that dry conditions within the alley can last up to one day longer in 2041-2070. Dry spells were shorter and simulated less often for *Populus spp.,* and not even once for *Quercus rubra*. We attribute this difference in frequency of dry critical conditions between the forage in the alley and the trees that are planted in rows to the rooting depth, which is greater for trees so that they can continue to extract water and retain water below the surface during dry summer months.

A simulated increase in the duration of dry periods for 2041-2070 is accompanied by a reduction of waterlogging conditions, which is most apparent for the frequency of one-day periods of waterlogging (20% fewer occurrences in 30 years for *Populus spp.* and *Quercus rubra*). In all cases however we simulated more and longer waterlogged periods for both trees than for forage. The reason that waterlogging occurs more often and lasts longer for *Populus spp.* and *Quercus rubra* is because their root systems retain water in the upper layers of the soil. Therefore, the elevated saturation level of the soil around the root system is more likely to increase to the point of waterlogging in the event of high intensity precipitation. Climate simulations for St. Paulin for the period 2041-2070 indicate a potential increase of temperature by 2.2-3.7°C depending on the season, resulting in an increase in transpiration and further increase in the risk of waterlogging.

6.2 Influence of alley cropping on soil erosion

Simulated results show that tree strips have a clear impact on total sediment exports. However, these results should be discussed further.

As noted in section 5.5.1, the model is only calibrated for hydrological processes, because no calibration events had precipitations intensities high enough to generate substantial erosion to be simulated by MHYDAS-erosion. Erosion predicted by the model for simulations with synthetic events had to be compared with similar events on a watershed with similar characteristics. Only triangular synthetic events are compared with the real events because they represent typical distributions for the Quebec region (Pelletier *et al.*, 2009). Duchemin (2001) study shows that for a comparable watershed located in Lennoxville (0.78-km^2) events similar to those simulated had the same order of magnitude magnitude for the total soil loss.

Distinct peak in flow rates observed for the Chicago rain in Figure 52 can be explained by the fact that the sampling site is located at the convergence of branches 14 and 15. The "pulse" produced by the

precipitation is observed at the outlet, depending on the different concentration times for the areas drained by the branches.

Abatement in Figure 52 and Table 20 should be interpreted taking into account that the simulated sediment flux at the outlet also includes sediments generated from bank erosion in the drainage network. With these considerations, the following observations can be made:

- For high intensity events as shown to the right of Figure 52 (Chicago), the majority of erosion occurs in the fields. The apparent significant tree strip abatement efficiency, because a larger proportion of the total erosion of the watershed is captured.

- For of low intensity events as shown to the left of Figure 12 (triangular), most of the erosion occurs in streams, showing lower tree strip abatement efficiency at the outlet.

- The results obtained with the triangular rains are more representative of the of the actual micro-catchment behaviour.

MHYDAS-Erosion is a distributed model, outputs for the flow rate and sediment flux at each hydrological unit (RS & SU) can be generated for each simulation. Further analysis on simulation results to identify the micro-catchment sediment sources and sinks is the subject of ongoing work.

7 Conclusion and recommendations

7.1 Findings

7.1.1 Hydrology

The hydrological study started out with the hypothesis that the root systems of trees in an alley cropping system improve the resilience of intercrops to drought and increased rainfall. In order to characterize and evaluate local hydrology and erosion in an alley cropping system in southern Quebec for present and future climate we developed a comprehensive approach with a field component and a hydrological modeling component. We performed weather observations and soil moisture measurements over a period of 2 years, and following a data analysis we identified the governing hydrological processes in the alley cropping system that we subsequently simulated with a two-dimensional model for water movement within the soil. Including simplified equations for variably-saturated flow in the soil, root uptake and transpiration, we parameterized the model and simulated the effects of alley cropping for a climate change scenario for 2041-2070.

The results of this simulation provides “what if” answers to the effect of alley cropping in the event that the climate simulation for 2041-2070 becomes reality. A comparison with respect to simulations for the reference period 1967-1996 suggests that:

- The soil becomes drier overall, leading to a reduction of the period of water availability;
- Dry conditions could last up to one day longer for intercrops. The intercrop suffers longer from dry spells than the trees because of its shallow rooting depth (up to 30 cm for the intercrop vs 95 cm and 55 cm for *Populus spp.* and *Quercus rubra*, respectively);
- *Quercus rubra* always has access to water during dry periods;
- Both *Populus spp.* and *Quercus rubra* are more vulnerable to waterlogging than the intercrop because they retain more water under normal conditions.

7.1.2 Erosion

In this report the primary objective concerning soil erosion was to test the following hypothesis:

- Tree strip systems significantly reduce erosion caused by rainfall.

The first sub-objective of this study was to develop a discretisation methodology for MYDAS-Erosion for an intensively farmed watershed, specifically for the Bras d’Henri watershed. The second sub-objective is to evaluate how the hypothetical use of tree strip systems at key locations within the watershed alters the sedimentological connectivity, and thus the field erosion and total sediment exports.

Simulated results showed that tree strips have a clear impact on total sediment exports. However, abatement values should be interpreted taking into account that the simulated sediment flux at the outlet also includes sediments generated from bank erosion in the drainage network. The simulation results were as follows:

- For a high intensity Chicago rainfalls, tree strips reduce total soil loss up to 20.8% for a return period of 10 years (6h), and 16.7 % for a return period of 100 years (24 hours).

- The low-intensity triangular rainfalls produce less erosion within the fields as they develop more gradually, causing an apparent reduction in the tree strips abatement efficiency with abatement values of 1.7% and 6.0% for return periods 10 and 100 years respectively.

- Simulated sediment fluxes are in the same order of magnitude as similar events on a comparable watershed located in Lennoxville (0.78-km^2). Further more, typical rainfall events for the Quebec region have distributions best represented by triangular design distributions (Pelletier *et al*., 2009), confirming validity of the simulated results.

- For of high intensity events, the majority of erosion occurs in the field, contrarily to low intensity events where most of the erosion occurs in the drainage network, explaining lower abatement efficiencies simulated at the outlet.

7.2 Implications

A wide range of crops can be grown in alley cropping systems, including corn, chesnuts, hazelnuts and walnuts. The use of alley cropping however is not limited to crops, but can also be linked to the production of greenery such as ornamental foliage plants. In this study we investigated the hydrology of an alley cropping system with tree rows composed of *Populus spp.* and *Quercus rubra*, and as intercrop forage, which has a shallow rooting depth. The implications of the study can be framed within the agricultural and economic context as follows:

- With respect to the tree species for which we studied the soil water dynamics, we observed longer and more frequent periods of dry conditions below *Populus spp.* than below *Quercus rubra*, given the reported water extraction rates for these trees (0.02 and 0.01 cm/hr, respectively). This means that *Populus spp.* requires so much water that it uses up all the available water when precipitation is absent, effectively entering in competition with the intercrop. Based on the hydrological simulations alone we are inclined to favor *Quercus rubra* over *Populus spp.* because of its lower water consumption and reduced risk of entering in competition with the intercrop.

- Although our simulations indicated that dry periods may have a greater impact in the future for forage in the intercrop area, they also show that drought issues occur less frequently for vegetation with a greater rooting depth, in which case water supply is more continuous. In order to achieve a healthy water balance for the intercrop, it is important to select an intercrop with a sufficient rooting depth. This ensures an optimal crop growth rate while simultaneously enjoying the benefits of alley cropping documented by the USDA, such as diversification of income,

improved soil health and improved crop health. The improvement of crop health is possible not only as a result of the reduction of moisture loss from the soil, but also because tree canopies protect the crop against wind damage, insect pests and extreme temperatures.

7.3 Limitations

The results of hydrological modeling present important indicators as to how alley cropping influences soil water dynamics in a changing climate, but these indicators must be interpreted with proper regard for the complexity of the spatial domain and the temporal variability of climate. The following methodological restrictions and practical realities need to be considered:

- In order to evaluate model performance, we compared simulated and observed water content at a depth of 25 cm and directly below *Populus spp.,* and at the same depth but 75 cm away from the tree. This visual comparison is a qualitative form of calibration and allows for verifying that the model simulates the right order of magnitude, but and automated calibration on multiple locations in the transect by means of inverse solution of the hydraulic parameters of the soil would result in a more accurate parameterization of the hydrological model.

- The accuracy and precision of the climate simulation used as input for the hydrological model have an important effect on the accuracy of the outcome. Our local climate simulation for the experimental site is based on only five regional climate simulations for 2041-2070, but more simulations would allow for a better identification of their respective uncertainties and thus yield more robust conclusions (Murphy *et al.*, 2009).

- Soil moisture data were not available for the reference period (1967-1996) and future period (2041-2070), and therefore we based the initial conditions for the corresponding simulations on FDR data recorded on 03/06/2011. This is the starting date of each simulated year for the reference and future periods, and the best possible predictor of how water is distributed along the transect of the alley cropping system. Although the FDR data show that the soil underneath the trees is often wetter that underneath the alley, we did not reconstruct initial conditions specific to each year or simulate them for the years in the future simulation period.

- No hydraulic measurements (pressure head) were performed below a depth of 100 cm, and therefore it is difficult to establish with certainty the time-dependent flux at the lower boundary of the computational domain. We assumed a free drainage boundary to emulate a situation with a low ground water table, although we are aware that this is only the case during a part of the season.

- Although the FDR measurements provide ample evidence of preferential infiltration under the trees, the hydrological model does not explicitly account for preferential flow. The preferential flow paths by which macropore flow, the common type of preferential flow in soils, can be measured in the field with the help of dye tracer, but macropores are not stable over longer periods of time. These factors make the explicit simulation of macropore flow and evaluation of model performance a daunting task.

- Lateral flow between the root systems of *Populus spp.*, *Quercus rubra* and forage was not accounted for in the hydrological model, although the effects of lateral flow to the trees on water availability for the intercrops is potentially great.

- MHYDAS-Erosion distributes the input rainfall for every time step, during a simulation. However, if the rain temporal resolution of is too large, intensity peaks causing the majority of the erosion and transport are spread out and not simulated appropriately. This therefore causes sediment flux to be underestimated at the outlet. Precipitation with a higher temporal resolution could better represent the peak intensity during storm events. Also, MHYDAS-Erosion is an event-based model which makes it difficult to simulate long-term climatic change effects; future work should involve the development of a continuous version of MHYDAS-Erosion.

- Substantial errors in the rating curve propagate in the calibration of the erosion model. Sediment flux values can thus only be interpreted with the same order of certainty as that for the flow rate values, and therefore the sediment flux at the outlet. Future flow rate measurements should be done at a stable section of the stream or with the use of a weir.

7.4 Recommendations

Our study has stirred up many new questions that need to be addressed, as well as points of improvement of the hydrological model. Our recommendations are the following:

- Regional downscaling of climate simulations could also be applied to a greater set of available climate simulations, including global climate models (GCMs), regional climate models (RCMs) and simulations calculated for the North American Regional Climate Change Assessment Program (NARCCAP). This approach would allow for a better estimation of uncertainty in the model input.

- For the sake of parsimony we used a linear water stress response function (Feddes *et al.*, 1978) in combination with a constant root distribution that does not evolve over time (Vrugt *et al.*, 2001). In order to incorporate the effects of a gradual increase in water uptake by the root system as a result of plant growth it is possible to use a nonlinear water and osmotic stress response function (Van Genuchten, 1987) in combination with a time-variable root depth function (Verhulst-Pearl, 1838; Pearl and Reed, 1920).

- Elaborating upon the preceding recommendation, the stress response function and time-variable root depth function can be integrated for multiple root systems in one computational domain in order to allow for simulating the interaction between different root systems (lateral flow);

- Alley cropping systems are know to reduce the amplitude of variations in temperature near the surface, by reducing wind speed. However, it is not known how this affects the growth rate of intercrops and the water balance. A comparison of data from fields with alley cropping and fields with traditional row cropping can point out the relationship between the attenuation of variations in temperature and the difference in water uptake between both fields.

- Soil aggregates are rich in clay and potentially retain large quantities of water. A combination of a model for matrix flow and a model that accounts for water retention in soil aggregates could simulate the short term effects of water storage and release on hydrology.

- MHYDAS-Erosion is a distributed model, outputs for the flow rate and sediment flux at each hydrological unit (RS and SU) can be generated for each simulation. Present work and avenues for further studies are:

    - Quantification of tree strip abatement efficiencies by analysing only the field outputs

    - Further analysis on simulation results to identify the micro-catchment sediment sources and sinks using VFDM (Gumiere and Rousseau, 2011)

    - Developing realistic abatement plans strategically placing tree rows where abatement is most needed, and testing then using the same synthetic rainfalls

    - Comparing the aforementioned simulation results with simulations using predicted rainfall events under changing climate conditions.

References

AAFC : Centre de recherche et de développement sur les sols et les grandes cultures, Agriculture et Agroalimentaire Canada (AAC), 2560, boul. Hochelaga, Québec, G1V 2J3

Allen, R. A., Pereira, L. S., Raes, D. and Smith, M., 1998. FAO Irrigation and Drainage Paper No. 56. Crop Evapotranspiration (guidelines for computing crop water requirements. Food and Agriculture Organization of the United Nations, Rome.

American National Standard Institute, 1972. Standard method of particle-size analysis of soils. Designation D 422–63, pp. 69–79. American National Standard A37.145.

Bambrick, A. D., Whalen, J. K., Bradley, R. L., Cogliastro, A., Gordon, A. M., Olivier, A., and Thevathasan, N. V., 2010. Spatial heterogeneity of soil organic carbon in tree-based intercropping systems in Quebec and Ontario, Canada. Agroforestry Systems 79: 343–353.

Boutier, L., 2013. Distribution spatiale des racines fines, disponibilité de la lumière et rendement dans un système de culture intercalaire avec arbres feuillus en zone tempérée. Final project report, Ouranos Consortium.

Brooks, R. H., and Corey, A. T., 1964. Hydraulic properties of porous media, Hydrology Paper No. 3, Colorado State University, Fort Collins, CO.

Cho, H.-K., Bowman, K. P. and North, G. R.. 2004. A comparison of gamma and lognormal distributions for characterizing satellite rain rates from the tropical rainfall measuring mission. Journal of Applied Meteorology 43: 1586-1597.

Chow et al. Handbook of applied hydrology: a compendium of water-resources technology. 260, \a new york: mc graw hill book company, 1964.

Deletic A, Fletcher TD. 2006. Performance of grass filters used for stormwater treatment - a field and modelling study. Journal of Hydrology 317(3–4): 261–275.

Duchemin, M. and Lachance, M. and Morin, G. and Lagace, R., 2001. Approche geomatique pour simuler l'erosion hydrique et le transport des sediments a l’echelle des petits bassins versants. Water Quality Research Journal of Canada 36: 435-473.

Feddes, R. A., Hoff, H., Bruen, M., Dawson, T., De Rosnay, P., Dirmeyer, P., Jackson, R. B., Kabat, P., Kleidon, A., Lilly, A., and Pitman, A. J., 2001. Modeling root water uptake in hydrological and climate models. Bulletin of the American Meteorological Society 82 (12): 2797–2809.

Feddes, R. A., Kowalik, P. J., Zaradny, H., 1978. Simulation of field water use and crop yield. John Wiley & Sons, New York, NY.

Foster GR, Flanagan DC, Nearing MA, Lane LJ, Risse LM, Finkner SC. 1995. Water Erosion Prediction Project (WEPP): technical documen- tation. Tech. rep. NSERL Report 10. National Soil Erosion Research Laboratory. USDA-ARS-MWA.1196 Soil Building: West Lafayette, IN 47907 – 1196.

Gumiere, S. J., Raclot, D., Cheviron, B., Davy, G., Louchart, X., Fabre, J. C., Moussa, R., and Le Bissonnais, Y., 2010. MHYDAS-Erosion: A distributed single-storm water erosion model for agricultural catchments. Hydrological Processes 25: 1717-1728.

Gumiere, S. J., and Rousseau, A. N., 2011. Development of VFDM: A riparian vegetated filter dimensioning model. International Symposium on Erosion and Landscape Evolution, American Society of Agricultural and Biological Engineers, Anchorage, AK, 18 September, 2011.

Hadley, J.L., Kuzeja, P.S., Daley, M.J., Phillips, N.G., Mulcahy, T., Singh, S., 2008. Water use and carbon exchange of red oak- and eastern hemlock-dominated forests in the northeastern USA: implications for ecosystem-level effects of hemlock woolly adelgid. Tree Physiology 28: 615-627.

Hargreaves, G. H., 1974. Estimation of potential and crop evapotranspiration. Transactions of the American Society of Agricultural Engineers 17 (4): 701-704.

Hayami S. 1951. On the Propagation of Flood Waves. Bulletin of the Disaster Prevention Research Institute, Kyoto University 1: Kyoto, Japan; 1–16.

Heggen, R. (2001). Normalized Antecedent Precipitation Index. J. Hydrol. Eng., 6(5), 377–381.

Hinckley, T. M., Brook, J. R., Cermak, J., Ceulemans, R., Kucera, J., Meinzer, F. C., Roberts, D. A., 1994. Water flux in a hybrid poplar stand. Tree Physiology 14: 1005-1018.

IRDA: Research Center and Head Office Aubert R. Michaud, 2700, rue Einstein Québec (Québec) G1P 3W8 CANADA Téléphone : 418 643-2380 # 690, aubert.michaud@irda.qc.ca

Kedem, B., 1990. Estimation of mean rain rate: application to satellite observations. Journal of Geophysical Research, 1990, Vol. 95 D2: 1965-1972.

Kremer, R. J., and Kussman, R. B., 2011. Soil quality in a pecan-kura clover alley cropping system in the Midwestern USA. Agroforestry Systems 83: 213-223.

Lagacherie P, Rabotin M, Colin F, Moussa R, Voltz M. 2010. Geo- MHYDAS: a landscape discretization tool for distributed hydrological modeling of cultivated areas. Computers & Geosciences 36(8): 1021–1032. DOI: 10.1016/j.cageo.2009.12.005.

Mailhot, A., Duchesne, S., Caya, D., and Talbot, G., 2007. Assessment of future change in intensity-duration-frequency (IDF) curves for Southern Quebec using the Canadian Regional Climate Model CRCM. Journal of Hydrology 347: 197-210.

McKeague, J.A. (ed), 1978. Manual on soil sampling and methods of analysis. Second edition. Subcommittee on Methods of Analysis. Canadian Soil Survey Committee. Canadian Society of Soil Science. Ottawa, Ont. 212 pp.

Monteith, J.L., 1981. Evaporation and surface temperature. Quarterly Journal of the Royal Meteorological Society 107: 1-27.

Morel-Seytoux HJ. 1984. From excess infiltration to aquifer recharge: A derivation based on the theory of flow of water in unsaturated soils. Water Resources Research 20: 1230–1240.

Mpelasoka, F. S. and Chiew, F. H. S., 2009. Influence of rainfall scenario contruction methods on runoff projections. Journal of Hydrometeorology 10: 1168-1183.

Murphy, J., Sexton, D., Jenkins, G., Boorman, P., Booth, B., Brown, C., Clark, R., Collins, M., Harris, G., Kendon, E., Betts, R., Brown, S., Howard, T. P., Humphrey, K. A., McCarthy, M. P., McDonald, R. E., Stephens, A., Wallace, C., Warren, R., Wilby, R., and Wood, R. A., 2009. UK Climate Projections Science Report: Climate change projections. Met Office Hadley Centre, Exeter.

Pearl, R., Reed, L., 1920. On the rate of growth of the population of united states since 1790 and its mathematical representation. Proceedings of the National Academy of Sciences USA G 6 (6), 275.

Pelletier, G., Anctil, F., and Filion, M., 2009. Characterization of 1-h rainfall temporal patterns using a Kohonen neural network: a Quebec City case study. Canadian Journal of Civil Engineering 36: 980-990.

Penman, H. L., 1948. Natural evaporation from open water, bare soil and grass. Proceedings of the Royal Society A 193: 120-145.

Plamboeck, A. H., Grip, H., and Nygren, U., 1999. A hydrological tracer study of water uptake depth in a Scots pine forest under two different water regimes. Oecologia 119: 452-460.

Rawls, W. J., D. L. Brakensiek, and K. E. Saxton, 1982. Estimating soil water properties. Transactions of the American Society of Agricultural Engineers 25(5): 1316-1320.

Rousseau AN, Fortin JP, Turcotte R, Royer A, Savary S, Quévy F, Noël P, Paniconi. 2011. Water News – CWRJ, 31: 18-20. 4.

Richards, L. A., 1931. Capillary conduction of liquids through porous mediums. Physics 1: 318-333.

Šejna, M., Šimůnek, J. and Van Genuchten, M. T., 2011. The HYDRUS software package for simulating two- and three-dimensional movement of water, heat and multiple solutes in variably-saturated media. User manual, version 2.0. PC Progress, Prague, Czech Republic, pp. 280.

Šimůnek, J., Vogel, T., and Van Genuchten, M. T., 1992. The SWMS_2D code for simulating water flow and solute transport in two-dimensional variably saturated media, version 1.1. U.S. Salinity Laboratory, USDA, ARS, Riverside, CA.

Šimůnek, J., Šejna, H., Saito, H., Sakai, M., Van Genuchten, M. T., 2009. The HYDRUS-1D software package for simulating the one-dimensional movement of water, heat, and multiple solutes in variably-saturated media. Version 4.08. University of California Riverside, Department of Environmental Sciences, Riverside, California.

Šimůnek, J., Van Genuchten, M. T. and Šejna, M., 2011. The HYDRUS software package for simulating two- and three-dimensional movement of water, heat and multiple solutes in variably-saturated media. Technical manual, version 2.0. PC Progress, Prague, Czech Republic, pp. 258.

Soil Classification Working Group, 1998. The Canadian system of soil classification, 3rd Edition. Agriculture and Agri-Food Canada Publication 1646 p.

USGS : National Field Manual for the Collection of Water-Quality Data, US Geological Survey : Techniques of Water-Resources Investigations Book 9, Handbooks for Water-Resources Investigations

Van Genuchten, M. T., 1987. A numerical model for water and solute movement in and below the root zone. Research Report No 121. U.S. Salinity Laboratory, USDA, ARS, Riverside, California.

Verhulst, P. F., 1838. Notice sur la loi que la population suit dans son accroissement. Curr. Math. Phys. 10: 138.

Vogel, T., 1987. SWMII – Numerical model of two-dimensional flow in variably saturated porous medium. Research report 87, Department of Hydraulics and Catchment Hydrology, Wageningen University, The Netherlands.

Vrugt, J. A., Hopmans, J. W., Šimůnek, J., 2001a. Calibration of a two-dimensional root water uptake model. Soil Science Society of America Journal 65 (4): 1027-1037.

Vrugt, J. A., Van Wijk, M. T., Hopmans, J. W., Šimůnek, J., 2001b. One-, two-, and three-dimensional root water uptake functions for transient modeling. Water Resources Research 37 (10): 2457-2470.

Wesseling, J. G., 1991. Meerjarige simulaties van grondwateronttrekking voor verschillende bodemprofielen, grondwatertrappen en gewassen met het model SWATRE. Report 152, Winand Staring Centre, Wageningen, the Netherlands.

Wilks, D. S., 2006. Statistical methods in the atmospheric sciences. Elsevier Academic Press, USA, Vol. 91.

Yan F-L, Shi Z-H, Li Z-X, Cai C-F. 2008. Estimating interrill soil erosion from aggregate stability of ultisols in subtropical china. Soil & Tillage Research 100: 34–41.

Acknowledgment

We would like to thank all colleagues and partners for their respective contributions to this project: A. Olivier (Université Laval), A. Paquette and S. Domenicano (both UQAM Centre for Forest Research), G. Thériault, G. Montminy and Nadia Goussard (AAFC), A. Cogliastro, D. Rivest and L. Bouttier (Institut de Recherche en Biologie Végétale), Y. Périard (Université Laval), M. F. Sottile (Ouranos), S. Tremblay, G. Levrel, M. Fossey, G. Carrer, and E. Maroy (all INRS-ETE).

Appendix A Parameterization of HYDRUS

- Name in HYDRUS: stpaulin_scenario_a_hpoplar, stpaulin_scenario_a_redoak, stpaulin_scenario_a_pasture, stpaulin_scenario_b_hpoplar, stpaulin_scenario_b_redoak, stpaulin_scenario_b_pasture

- Main processes: Water flow; root water uptake (evapotranspiration), inverse solution

- Inverse solution: Estimate soil hydraulic parameters, weighting by standard deviation. Maximum of 0 iterations, between 7000-10,000 data points in the objective function, one value per 15 minutes. The inverse solution model is used to compare simulated with observed water content only; parameters are not actually estimated.

- Time information: 153 days simulation period, corresponding with the period between 2011-06-03 and 2011-11-03 (scenario a), and the period between 2012-06-03 and 2012-11-03 (scenario b), respectively. Time step equals 1 hour, final time is 3672 hours; 14688 time-variable boundary conditions.

- Output information: Print times: 153 (every 24 hours)

- Soil hydraulic model: Brooks-Corey, with no hysteresis in retention curve;

- Water flow parameters: Model parameters corresponding with the Brook-Corey model (1964) for loamy sand layer between 0-15 cm depth (Ks=14.59 mm/hr), sand layer between 15-75 cm depth (Ks=29.7 mm/hr), loam layer between 75-110 cm depth (Ks=1.04 mm/hr) and clay loam layer between 110-140 cm depth (Ks=0.26 mm/hr); for the unsampled part of the domain between 140-300 cm we assumed water flow parameter values for clay;

- Root water and solute uptake model: Feddes; critical stress 1, no solute stress;

    - Feddes parameters for hybrid poplar: P0=-10cm; P0pt=-25 cm; P2H=-500 cm; P2L=-800 cm; P3=-8000 cm (values of P0-P3 based on HYDRUS values for deciduous fruit); r2H=0.02 cm/hr (Hinckley *et al.*, 1994); r2L=0.004 cm/hr (equals 20% of r2H).

    - Feddes parameters for red oak: P0=-10cm; P0pt=-25 cm; P2H=-500 cm; P2L=-800 cm; P3=-8000 cm (values of P0-P3 based on HYDRUS values for deciduous fruit); r2H=0.016667 cm/hr (Hadley *et al.*, 2008); r2L=0.003333 cm/hr (equals 20% of r2H).

    - Feddes parameters for pasture: P0=-10cm; P0pt=-25 cm; P2H=-200 cm; P2L=-800 cm; P3=-8000 cm (values of P0-P3 based on HYDRUS values for deciduous fruit); r2H=0.01 cm/hr (half of hybrid poplar value); r2L=0.0005 cm/hr (equals 20% of r2H).

- Time variable boundary conditions of the upper boundary: atmospheric boundary with time-variable input from rainfall data and output calculated by the root uptake model.

- Precipitation and other weather variables were provided for every 15 minutes, and in order to synchronize these data with FDR data we reinterpolated them for the whole hour, 15 minutes past the hour, 30 minutes past the hour and 45 past the hour. The total of interpolated precipitation intensities calculated for HYDRUS was compared to the total of the original data record to verify that the water balance was maintained.

- Potential evaporation 0 cm/hr, potential transpiration is time-variable, calculated with the Penman-Monteith equation (Allen *et al.*, 1998). Minimum allowed pressure at top: -10,000 cm. Surface associated with transpiration 300 cm (hybrid poplar and red oak) and 640 cm (pasture)

- Lower boundary set to no flux, side boundaries no flux

- Finite element mesh parameters: triangular domain with a target finite element size of 20 cm and 10 cm at the upper boundary.

- Root distribution:

  - Hybrid poplar (left): Maximum rooting depth 95 cm and depth of maximum root density 7.5 cm (Bouttier, observed in 2011).

  - Red oak (right): Maximum rooting depth 55 cm and depth of maximum root density 7.5 cm (Bouttier, observed in 2011).

  - Pasture: Maximum rooting depth 30 cm and depth of maximum root density 0 cm.

- Dimensions of rectangular domain: 1250*300 cm depth, corresponding with the area between the two axes of tree rows;

- Initial water content: We performed a linear interpolation of the observed water content on the starting date and used this as initial conditions in HYDRUS.

Appendix B List of publications and reports

Hallema, D. W., Rousseau, A. N., and Gumiere, S. J. Modeling the evolution of soil moisture patterns in an alley cropping system in Quebec, Canada. Paper in preparation.

Hallema, D. W., Rousseau, A. N., and Gumiere, S. J., 2013. Modeling the evolution of soil moisture patterns in an alley cropping system in southern Quebec. La Recherche Hydrologique au Québec dans un contexte de changement climatique, Institut National de la Recherche Scientifique Centre Eau, Terre, Environnement, Quebec City, Canada, 25-26 April, 2013.

Hallema, D. W., Rousseau, A. N., and Gumiere, S. J., 2012. A graphical weather report for St. Paulin, Quebec (2011-2012). Institut National de la Recherche Scientifique, Centre Eau Terre Environnement, Quebec City, Canada.

Hallema, D. W., Rousseau, A. N., Paquette, A., and Gumiere, S. J., 2012. The effects of Hurricane Sandy measured in the Laurentian foothills of Quebec (Canada) with a mobile weather station. Institut National de la Recherche Scientifique, Centre Eau Terre Environnement, Quebec City, Canada.

Hallema, D. W., Rousseau, A. N., and Gumiere, S. J., 2012. Soil moisture mapping in an alley cropping system in Quebec, Canada. Fall Meeting, American Geophysical Union, San Francisco, California, 3-7 December, 2012.

Hould-Gosselin, G., Rousseau, A. N., Gumiere, S. J., and Hallema, D. W., 2013. Évaluation de l'impact de bandes sylvicoles sur la connectivité sédimentologique d'un petit bassin versant agricole sous un climat tempéré. La Recherche Hydrologique au Québec dans un contexte de changement climatique, Institut National de la Recherche Scientifique Centre Eau, Terre, Environnement, Quebec City, Canada, 25-26 April, 2013.

Paquette, A., Olivier, A., Cogliastro, A., Bouttier, L., Rivest, D., Messier, C., Rousseau, A., Hallema, D. W., Gumiere, S. J., Work, T., Doblas, E., Revéret, J. P., Alam, M. and Domenicano, S., 2012. Contribution de systèmes agroforestiers multifonctionnels à la capacité d'adaptation aux changements climatiques des agroécosystèmes. 5th Ouranos Symposium. Université du Québec à Montréal, Montreal, Canada, 19-21 November, 2012.

Rousseau, A. N., Hallema, D. W., Gumiere, S. J., Carrer, G., and Fossey, M., 2012. The influence of alley cropping systems on soil water dynamics and soil erosion in a changing climate. Ouranos-ICAR Climate Change Action Plan 26 "Biodiversity", progress report 1334. Institut National de la Recherche Scientifique, Centre Eau Terre Environnement, Quebec City, Canada.

Rousseau, A. N., Hallema, D. W., Gumiere, S. J., Périard, Y., Hould-Gosselin, G., Paquette, A., and Olivier, A., 2013. Étude de l'impact des systèmes intercalaires sylvicoles-agricoles sur la dynamique de l'eau et la connectivité sédimentaire : suivi de terrain et modélisation numérique. Journée Scientifique - Agroforesterie, Centre de Référence en Agriculture et Agroalimentaire du Québec, Drummondville, Canada, 7 February, 2013.

Rousseau, A. N., Nadeau, D., Carrer, G., Oreiller, M., Hallema, D. W., Gumiere, S. J., Jutras, S., and St-Hilaire, A., 2012. Suivi instrumental pour l'étude des processus hydrologiques en milieux nordique et agricole. GaGiLau (Garonne, Gironde, St-Laurent) Conference, Session 1: Hydrologie et écohydrologie. Institut National de la Recherche Scientifique, Centre Eau Terre Environnement, Quebec City, Canada, 25-26 September, 2012.

Appendix C WEBs watershed soil types

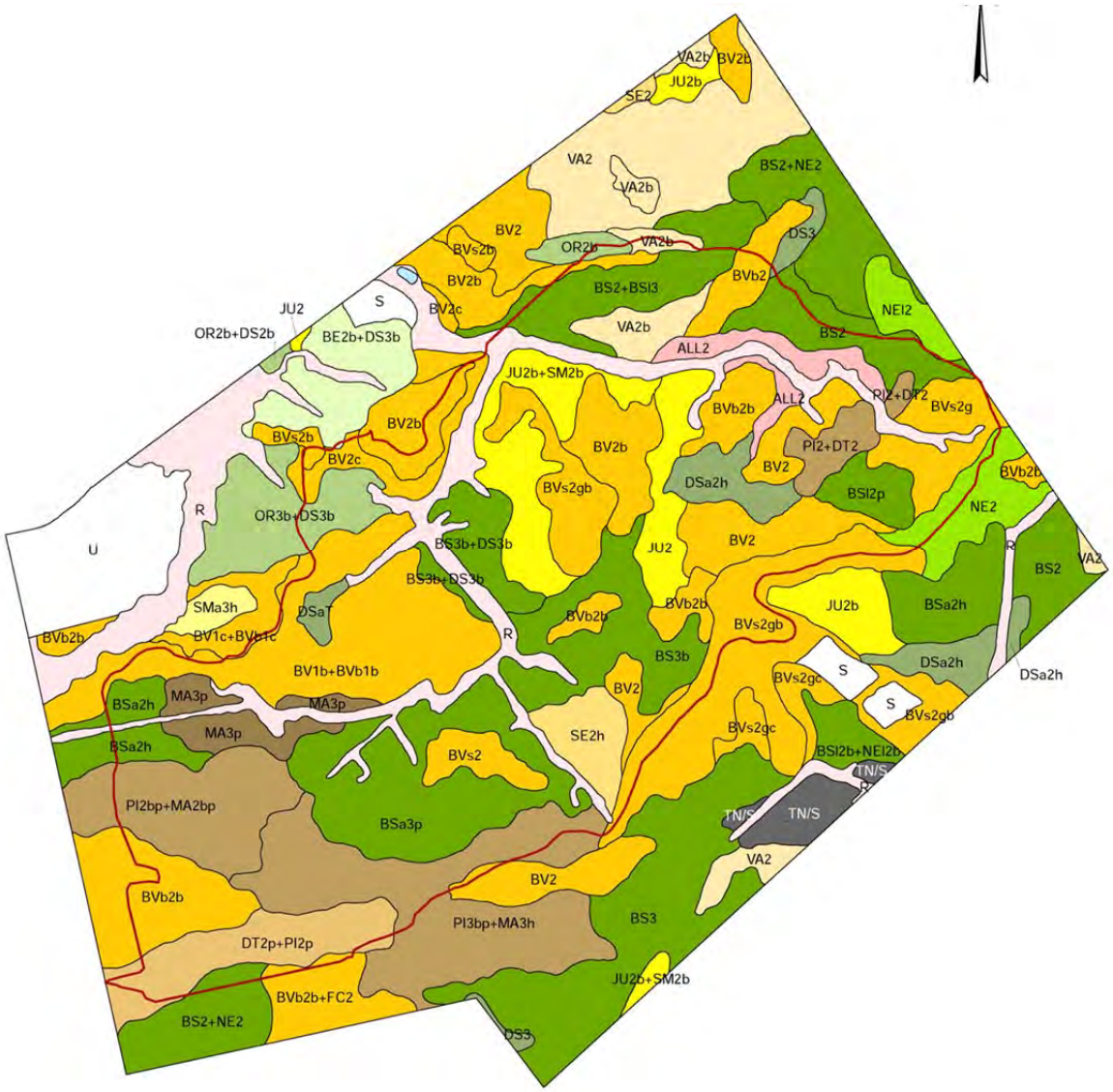

Figure 53: Soil types surveyed by AAFC

Table 21 : Soil types surveyed by AAC

Symbole	Description
All2	Alluvions, loam sableux
BE2b + DS3b	Complexe de sols : Breault, loam sableux très fin, 3 - 8% de pente; Des Saults, loam limoneux, 3 - 8% de pente
BS2	Le Bras, loam sableux fin
BS2 + BSl3	Complexe de sols : Le Bras, loam sableux fin; Le Bras, substratum loameux, loam limoneux
BS2 + NE2	Complexe de sols : Le Bras, loam sableux fin; Neubois, loam sableux fin
BS3	Le Bras, loam limoneux
BS3b	Le Bras, loam limoneux, 3 - 8% de pente
BS3b + DS3b	Complexe de sols : Le Bras, loam limoneux; Des Saults, loam limoneux, 3 - 8% de pente
BSa2h	Le Bras, variante calcaire, loam sableux fin humifère
BSa3p	Le Bras, variante calcaire, loam limoneux, légèrement à modérément pierreux
BSl2b + NEl2b	Complexe de sols : Le Bras, substratum loameux, loam sableux fin, 3 - 8% de pente; Neubois, substratum loameux, loam sableux fin, 3 - 8% de pente
BSl2p	Le Bras, substratum loameux, loam sableux, légèrement à modérément pierreux
BV1b + BVb1b	Complexe de sols : Beaurivage, sable loameux, 3 - 8% de pente; Beaurivage, variante brunisolique, sable loameux, 3 - 8% de pente
BV1c + BVb1c	Complexe de sols : Beaurivage, sable loameux, 8 - 15% de pente; Beaurivage, variante brunisolique, sable loameux, 8 - 15% de pente
BV2	Beaurivage, loam sableux
BV2b	Beaurivage, loam sableux, 3 - 8% de pente
BV2c	Beaurivage, loam sableux, 8 - 15% de pente
BVb2	Beaurivage, variante brunisolique, loam sableux
BVb2b	Beaurivage, variante brunisolique, loam sableux, 3 - 8% de pente
BVb2b + FC2	Complexe de sols : Beaurivage, variante brunisolique, loam sableux, 3 - 8% de pente; Fourchette, loam sableux
BVs2	Beaurivage, squelettique-sableux, loam sableux
BVs2b	Beaurivage, squelettique-sableux, loam sableux, 3 - 8% de pente
BVs2g	Beaurivage, squelettique-sableux, loam sableux graveleux
BVs2gb	Beaurivage, squelettique-sableux, loam sableux graveleux, 3 - 8% de pente
BVs2gc	Beaurivage, squelettique-sableux, loam sableux graveleux, 8 - 15% de pente
DS3	Des Saults, loam limoneux
DSa2h	Des Saults, variante calcaire, loam sableux fin humifère
DSaT	Des Saults, variante calcaire, tourbeux
DT2p + Pl2p	Complexe de sols : Dosquet, loam sableux, légèrement à modérément pierreux; Des Pins, loam sableux fin, légèrement à modérément pierreux
JU2	Saint-Jude, loam sableux
JU2b	Saint-Jude, loam sableux, 3 - 8% de pente
JU2b + SM2b	Complexe de sols : Saint-Jude, loam sableux, 3 - 8% de pente; Saint-Samuel, loam sableux, 3 - 8% de pente
MA3p	Mawcook, loam, légèrement à modérément pierreux
NE2	Neubois, loam sableux fin
NEl2	Neubois, substratum loameux, loam sableux fin
OR2b	Des Orignaux, loam sableux fin, 3 - 8% de pente
OR2b + DS2b	Complexe de sols : Des Orignaux, loam sableux fin, 3 - 8% de pente; Des Saults, loam sableux fin, 3 - 8% de pente
OR3b + DS3b	Complexe de sols : Des Orignaux, loam limoneux, 3 - 8% de pente; Des Saults, loam, 3 - 8% de pente
Pl2 + DT2	Complexe de sols : Des Pins, loam sableux fin; Dosquet, loam sableux
Pl2bp + MA2bp	Complexe de sols : Des Pins, loam sableux fin, 3 - 8% de pente, légèrement à modérément pierreux; Mawcook, loam sableux, 3 - 8% de pente, légèrement à modérément pierreux
Pl3bp + MA3h	Complexe de sols : Des Pins, loam limoneux, 3 - 8% de pente, légèrement à modérément pierreux; Mawcook, loam humifère
SE2	Séraphine, loam sableux fin
SE2h	Séraphine, loam sableux fin humifère
SMa3h	Saint-Samuel, variante calcaire, loam limoneux humifère
VA2	Valère, loam sableux fin
VA2b	Valère, loam sableux fin, 3 - 8% de pente
TN/S	Humisol terrique sur matériau sableux
R	Ravin
S	Sablière
U	Urbain

Appendix D Method for establishing rating curves

Fonction de régression

La fonction de régression utilisée afin d'établir la relation entre la hauteur d'eau et les débits est le logarithme de la fonction puissance :

$$\ln(Q) = \beta_0 + \beta_1 \ln(h) \quad (2)$$

Où h est la hauteur d'eau moyenne journalière (m), Q est le débit moyen journalier (L/s) et β_0, β_1 des constantes. Une régression linéaire simple a été établie entre la hauteur d'eau et le débit et les paramètres de la régression ont été estimés par la méthode des moindres carrés. Par ailleurs, en visualisant les paires de points de 2005 à 2012, nous avons pu constater une grande variabilité interannuelle. En effet, les paires de points pour chaque année semblent suivre la même tendance, mais ces courbes sont décalées d'une année à l'autre. Puisque le cours d'eau est très petit, cela peut être dû à sa bathymétrie qui varie d'une année à l'autre, suite au gel-dégel, aux fontes printanières, à la variabilité du climat, à des travaux agricoles, etc. De plus, il n'y a pas de barrage en aval de la section étudiée qui pourrait faire varier les hauteurs d'eau d'une année à l'autre. Normalement, les mesures de hauteur-débit sont calculées en vue d'obtenir une seule courbe de tarage pour la section du cours d'eau. Cependant, étant donné la disparité des paires de points d'une année à l'autre et parce que le but du projet étant d'estimer le mieux possible les charges de contaminants agricoles, huit courbes de régression ont été calculées, une pour chaque année (2005 à 2012).

Mesures de hauteurs d'eau

Une étape cruciale lors du calcul des courbes de tarage a été de choisir les hauteurs d'eau à utiliser pour la régression, car plusieurs hauteurs d'eau associées aux débits sont disponibles. Il y a d'abord des sondes au-dessus du cours d'eau qui mesure les hauteurs d'eau toutes les 15 minutes. La sonde SR50 et la multisonde sont en fonction depuis 2005, mais une nouvelle sonde a été installée en 2009, une sonde ultrasonique (module 710). Les données provenant de la sonde SR50 ont été utilisées entre 2005 et 2008, et celles de la sonde ultrasonique entre 2009 et aujourd'hui, car cette dernière est plus fiable et plus précise (AAC). La hauteur d'eau reliée au débit mesuré peut être celle qui est enregistrée par la sonde dans le temps le plus rapproché. Il y a ensuite des hauteurs d'eau calculées manuellement à l'aide d'une règle graduée qui ont été prises lors du calcul du débit juste au-dessus de la sonde. Cependant, ces hauteurs ont été prises de 2005 à 2008. Il y a néanmoins d'autres hauteurs d'eau prises manuellement, celles prises pour calculer les superficies de chaque section du cours d'eau lors du calcul du débit. En visualisant la bathymétrie du cours d'eau, nous avons fixé une section comme étant celles en dessous de la sonde et nous avons utilisé les hauteurs d'eau calculées à cette section.

Les hauteurs d'eau des sondes ont d'abord été utilisées comme élément entrant dans la courbe de tarage, car elles paraissaient plus régulières et précises. Les régressions établies selon ces hauteurs sont très satisfaisantes pour certaines années. Cependant, en validant les courbes obtenues par un bilan hydrologique simple, les écoulements annuels totaux sont trop élevés pour certaines années.

Les régressions hauteur-débit ont ensuite été testées avec les hauteurs prises manuellement. Puisque les hauteurs entrant dans la courbe de tarage sont celle prises manuellement et que celles calculées journalièrement proviennent des sondes, les bilans hydrologiques sont peu concluants, car les hauteurs manuelles versus celles des sondes diffèrent beaucoup. Les différences entre les hauteurs prises manuellement et celles prises par les sondes s'expliquent par la variation de la précision et de l'exactitude des résultats.

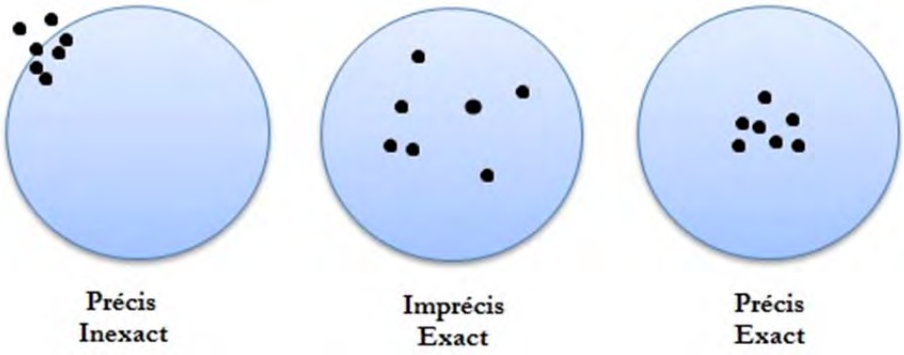

Figure 54: Précision et exactitude des erreurs

Les hauteurs prises avec les sondes sont précises et inexactes alors que les hauteurs manuelles sont moins précises, mais plus exactes (voir Figure 54). Les hauteurs d'eau manuelles ont tout de même été utilisées lors de la régression hauteur-débit même si elles sont moins précises que les hauteurs des sondes pour certaines années. Elles ont été choisies entre autres parce qu'elles semblent en général mieux représenter les débits élevés comparativement aux hauteurs prises avec les sondes et par conséquent, il en découle de bons bilans hydrologiques. Une régression linéaire simple a ensuite été établie entre les hauteurs manuelles et celles des sondes afin d'ajuster les hauteurs moyennes journalières prises par les sondes.

$$\mathrm{H}_{man} = \beta_0 + \beta_1 \mathrm{H}_{sonde} \quad (3)$$

Où H_{man} est la hauteur d'eau mesurée manuellement à l'aide d'une règle graduée et où H_{sonde} est la hauteur d'eau mesurée par la sonde le plus rapprochée dans le temps (hauteurs aux 15 minutes). En résumé, les courbes de tarage ont été obtenues à l'aide des hauteurs prises manuellement, et les données de hauteurs journalières résultent d'une régression linéaire entre les hauteurs des sondes et les hauteurs manuelles.

Incertitudes des débits

L'expression de l'incertitude associée au calcul des débits est un facteur très important à considérer lors des calculs relatifs à l'écoulement, à la ressource en eau ou aux charges en effluents. Cependant, très peu d'études dans la littérature ont analysé l'incertitude sur des mesures de débits individuels. Une valeur fixe d'incertitude est souvent utilisée pour toutes les données de débits. Les incertitudes associées aux mesures des débits peuvent provenir d'erreurs environnementales (écoulement non stationnaire durant la période de mesure, variation de la géométrie du cours d'eau qui peut être due à de l'érosion ou de la sédimentation, hystérèse lors d'événements de pluie, etc) ou d'erreurs humaines (manipulations de l'équipement, calibrage des instruments, erreurs d'intégration spatiale, etc). Il s'ajoute ensuite des

incertitudes lors du calcul des courbe de tarage (erreurs d'extrapolation, fonction de régression utilisée, etc). La combinaison des incertitudes lors du calcul du débit Q_t au temps t peut être exprimée comme suit (Le Coz, 2012) :

$$\varepsilon^2\,(Q_t) = \varepsilon_R^2(Q) + \,\varepsilon_{CH}^2(Q_t) + \left(\frac{\partial Q}{\partial h}\right)^2 \varepsilon^2\,(h_t)$$

Où :

$\varepsilon_R^2(Q)$ est l'incertitude dans la relation hauteur-débit. Ces erreurs peuvent provenir de la fonction utilisée ou de la calibration des paramètres. Elle est particulièrement importante lorsque des données sont dispersées ou manquantes et qu'il faut extrapoler afin d'obtenir les données de hauts débits.

$\varepsilon_{CH}^2(Q_t)$ est l'incertitude reliée aux conditions hydrologiques au temps t. Cela peut être causé par des effets de remous, de l'érosion ou de la sédimentation qui font varier la géométrie du cours d'eau (hystérèse) ou par des changements saisonniers dans la végétation.

$\left(\frac{\partial Q}{\partial h}\right)^2 \varepsilon^2\,(h_t)$ est l'incertitude reliée à la mesure de hauteur d'eau au temps t. Le Coz (2012) précise cependant que plusieurs auteurs reconnaissent que l'incertitude reliée à la mesure de la hauteur d'eau est très négligeable en comparaison à l'incertitude lors des mesures de débit.

L'incertitude des débits a été estimée par une méthode de simulation de style Monte-Carlo. L'idée est de définir les paramètres de régression *p* comme étant des variables aléatoires qui peuvent être représentées par une distribution statistique $f\left(p \mid \vec{\beta}\right)$ où $\vec{\beta}$ sont les paramètres de la distribution. Cette méthode permet ainsi d'évaluer les paramètres et les erreurs par processus stochastique. De plus, puisque cette technique est directement liée à des fonctions de densité de probabilité, l'analyse d'incertitude peut être réalisée facilement en utilisant les percentiles de la distribution. Cependant, quelques suppositions doivent être faites sur la distribution des paramètres. Rappelons que l'équation de régression linéaire utilisée est

$$\widehat{\ln(Q)} = b_0 + b_1 \ln(h)$$

Pour établir la distribution des paramètres, trois cas possibles sont considérés : la première étant un b_0 connu et b_1 suivant une distribution $N(\beta_1, \sigma_{\beta_1}^2)$; le deuxième étant un modèle avec b_0 et b_1 suivant une distribution $N(\beta_0, \sigma_{\beta_0}^2)$ et $N(\beta_1, \sigma_{\beta_1}^2)$ respectivement; et enfin le troisième cas étant une distribution bivariée de b_0 et b_1 $N((\beta_0, \beta_1), \mathrm{V})$, où V est la matrice de variance-covariance. Les paramètres des distributions sont obtenus de données mesurées sur le site ou d'études antérieures. Les paramètres estimés sont donc ceux obtenus des courbes de tarage.

Appendix E WEBs watershed field photographs

Figure 55: TSS sampling apparatus

Figure 56: Branch 15 near the outlet in October